Engineering Organoids for Stem Cell Maturation

Neeti N. Gandhi

Dissertation submitted to the faculty of the Virginia Polytechnic Institute and State University in partial fulfillment of the requirements for the degree of

Doctor of Philosophy
In
Chemical Engineering

Padmavathy Rajagopalan, PhD, Chair
Richey Davis, PhD
Yong Woo Lee, PhD
Rong Tong, PhD
Steven Parker Wrenn, PhD

Nov. 18, 2024
Blacksburg, VA

Keywords: Organoids, Induced Pluripotent Stem Cells, Liver, Maturation, Virology

Engineering Organoids for Stem Cell Maturation

Neeti N. Gandhi

ABSTRACT (ACADEMIC)

The liver is the largest visceral organ in the body. It is responsible for performing an array of vital functions, including the filtration of blood, synthesis of different macromolecules, and the biotransformation of drugs and toxicants. Hepatocytes, or the main liver cell type, perform most of these functions. Primary human hepatocytes (PHHs) are ideal for *in vitro* liver studies since they are obtained directly from tissues and exhibit mature markers and express all enzymes. However, sourcing these cells is extremely difficult since they usually require invasive retrieval and are limited in quantity. Induced pluripotent stem cell (iPSC)-hepatocyte-like cells (iHLCs) hold tremendous potential to be used as a substitute for PHHs since they are obtained non-invasively. However, iHLCs require further maturation before they can replace PHHs due to their lower liver-specific functions and fetal characteristics. Existing maturation approaches commonly require administration of exogenous chemicals at concentrations up to 10^6-fold higher than present *in vivo*. The lack of a systematic approach to mature iHLCs currently limits their widespread use.

During liver embryogenesis, neighboring cells secrete different proteins that regulate and induce multiple pathways that mature hepatic progenitor cells to functional hepatocytes. We report the assembly of a multicellular 3D human liver organoid with iHLCs that recapitulates the *in vivo* hepatic microenvironment. Intra- and intercellular signaling between human hepatic cells in the organoid result in mature iHLCs that exhibit several markers and functions of PHHs within one to two weeks in culture. When two other cell types, Kupffer cells and liver sinusoidal endothelial cells, are present in the organoids, they secrete signaling molecules that synergistically mature

iHLCs. Relying solely on endogenous secretion provides a systematic and reproducible approach to generate mature iHLCs for drug, disease, and patient-specific *in vitro* studies.

Engineering Organoids for Stem Cell Maturation

Neeti N. Gandhi

ABSTRACT (GENERAL)

The liver is the largest internal organ in the body. It is responsible for performing an array of vital functions, including the filtration of blood, synthesis of different molecules, and metabolism of drugs and toxicants. Hepatocytes, or the main liver cell type, perform most of these functions. Typically, primary human hepatocytes (PHHs) are ideal for *in vitro* liver studies since they are obtained directly from tissues and exhibit adult characteristics and functions. However, sourcing these adult liver cells is extremely difficult since they are usually obtained through biopsies and are limited in quantity. Induced pluripotent stem cell (iPSC)-hepatocyte-like cells (iHLCs) hold tremendous potential to be used as a substitute since they can be obtained non-invasively. However, iHLCs require further maturation before they can be substituted for PHHs due to their lower liver-related functions and immature characteristics. Existing maturation approaches require the administration of chemical mixtures that can be up to a million times higher than the concentrations of these same molecules inside the body. The lack of a systematic approach to mature iHLCs currently limits their widespread use.

During liver development, neighboring cells secrete different proteins that regulate and induce multiple pathways that aid in the maturation of cells into adult liver cells. We report the assembly of a multicellular 3D human liver organoid with iHLCs that recapitulates the *in vivo* hepatic microenvironment. Intra- and intercellular signaling between human hepatic cells in the organoid result in mature iHLCs that exhibit several markers and functions of PHHs within one to two weeks in culture. When two other hepatic cell types, Kupffer cells and liver sinusoidal endothelial cells, are present in the organoids, they secrete signaling molecules that synergistically mature iHLCs.

Relying solely on intercellular secretion from the cells provides a systematic and reproducible approach to generate mature iHLCs for drug, disease, and patient-specific *in vitro* studies.

ACKNOWLEDGEMENTS

First and foremost, I would like to thank my advisor, Dr. Padma Rajagopalan. I owe my growth over the last four years as a scientist to everything she has taught me. She has spent countless hours guiding me in my research as well as mentoring, encouraging, and supporting me. She has been an incredibly influential mentor in my career and has pushed me to achieve goals that surpassed my expectations. I am forever grateful for the opportunities and experiences that I have gained working under her guidance. I would also like to thank the rest of my committee, Dr. Rong Tong, Dr. Richey Davis, Dr. Yong Woo Lee, and Dr. Steven Wrenn, for their time and feedback. I would like to acknowledge the support and friendship from previous and current lab group members throughout the years as well.

To my closest family and friends, Shobhit and Holly, Mom, Dad, Ba, Dada, Harika, Angie Masi, and my mother and father in-law, thank you for all the love and support you have given me throughout my PhD. Thank you for always listening and encouraging me to never give up. I owe everything to you all and could not have done this without you.

I gratefully acknowledge the financial support provided by the National Science Foundation, the United States Department of Agriculture, the Institute for Critical Technology and Applied Sciences at Virginia Tech, the Computational Tissue Engineering Interdisciplinary Graduate Education Program at Virginia Tech and the Kirk and Noel Schulz Transformative Graduate Education Fellowship from Virginia Tech.

TABLE OF CONTENTS

LIST OF FIGURES

LIST OF TABLES

LIST OF ABBREIVIATIONS

7-hydroxy-4 trifluoromethylcoumarin - **HFC**

7-methoxy-4 trifluoromethylcourmarin - **MFC**

Aceaminophen - **APAP**

Air-liquid Interface - **ALI**

Alphafetoprotein - **AFP**

Alpha-1 antitrypsin - **A1AT**

Antimicrobial peptides - **AMP**

Aquaporin - **AQP**

Asialoglycoprotein receptor - **ASGPR**

ATP binding cassette coding genes - **ABCB**

Bactenecin - **Bac**

Bacterial media - **BM**

Bile salt export protein - **BSEP**

Bovine airway endothelial - **BAE**

Bovine epithelial - **BE**

Bovine epithelial type 2 - **BAT2**

Bone morphogenetic Factor - **BMP**

Bovine herpes virus - **BHV**

Bovine myeloid antimicrobial peptide - **BMAMP**

Bovine parainfluenza-3 virus - **BPIV-3**

Bovine respiratory disease - **BRD**

Bovine respiratory syncytial virus - **BRSV**

Bovine serum albumin - **BSA**

Bovine viral diarrhea virus - **BVDV**

Cell media - **CM**

Cytochrome P450 - **CYP**

Dimethyl sulfoxide - **DMSO**

Ile-(6) aminohexanoic amide - **dihexa**

Embryonic stem cells - **ESCs**

Endoplasmic reticulum - **ER**

Ethylenediaminetetraacetic acid - **EDTA**

Ethanol - **EtOH**

Extracellular matrix - **ECM**

False discovery rate - **FDR**

Fibroblast growth factor - **FGF**

Gene Ontology - **GO**

Glutathione - **GSH**

Half maximal effective concentration - **EC_{50}**

Hepatic stellate cells - **HSCs**

Hepatitis E - **HEV**

Hepatocyte-like cells - **iHLCs**

Hepatocyte growth factor - **HGF**

Hours post infection - **hpi**

Human umbilical vein endothelial cells - **HUVECs**

Human adipose microvascular endothelial cells - **HAMECs**

Induced pluripotent stem cells - **iPSCs**

iPSC derived-endothelial cells - **iECs**

Immunoglobulin binding protein - **IgBP**

Immunoglobulin binding protein A - **IbpA**

Kupffer cells - **KCs**

Lethal concentration 50 - **LC_{50}**

Lipopolysaccharide - **LPS**

Liver-enriched transcription factor - **LETF**

Liver sinusoidal endothelial cells - **LSECs**

Liver X receptor - **LXR**

Mammalian target of rapamycin - **mTOR**

Mesenchymal stem cells - **MSCs**

MicroRNA - **miRNA**

Minimum inhibitory concentration - **MIC**

Mitogen-activated protein - **MAP**

Multidrug resistance associate protein - **MRP**

Non-parenchymal cells - **NPCs**

Nuclear factor kappa light chain enhancer of activated B cells - **NF-κB**

Oncostatin M - **OSM**

Precision-cut lung slices - **PCLS**

Penicillin streptomycin - **Pen-Strep**

Phosphate buffered saline - **PBS**

Phosphoenolpyruvate carboxykinase - **PCK1**

Phosphoinositide 3-kinase - **PI3K**

Pluripotent stem cells - **PSCs**

Polycaprolactone - **PCL**

Poly-L-Lactic acid - **PLLA**

Primary human hepatocytes - **PHHs**

Protein Kinase B - **AKT**

Principal component - **PC**

Principal component analyses - **PCA**

Prostaglandin E2 - **PGE2**

Reactive oxygen species - **ROS**

RNA-sequencing - **RNA-seq**

Single cell RNA-sequencing - **scRNA-seq**

Single nucleotide polymorphisms - **SNP**

Sodium dodecyl sulfate - **SDS**

Submerged tissue cultures - **STCs**

t-distributed stochastic neighbor embedding - **t-SNE**

Tissue culture polystyrene - **TCPS**

Toll-like receptor - **TLR**

Tracheal antimicrobial peptide - **TAP**

Trans-epithelial electrical resistance - **TEER**

Transforming growth factor - **TGF**

Triiodothyronine - **T3**

UDP glucuronosyltransferase - **UGT**

Vascular endothelial growth factor - **VEGF**

Zonula occuldens-1 - **ZO-1**

Chapter 1: Background

1.1 Liver Structure and Cellular Composition

The liver is the largest visceral organ in the body, weighing around 3-4 pounds (1-3). It is located immediately under the diaphragm, and ranges in length from 9 to 10 inches (1-3). Hepatic portal circulation is a vital function that allows the liver to remove any harmful metabolites and secrete proteins into the bloodstream (1-3). At any given time, 80% of blood passes through the liver via the hepatic portal vein (3). Blood flow through the liver is critical, and when disrupted, can lead to severe symptoms that impact the rest of the body. For example, hepatomegaly or enlargement of the liver, jaundice, or the buildup of bilirubin, and ascites, or excess fluid in between the abdominal lining and the organs, may occur when the liver is not functioning properly (1-6). In total, the liver is responsible for an array of vital functions, such as metabolism of various macromolecules (proteins, carbohydrates, and lipids), β-oxidation of fatty acids, bile acid production, cholesterol production and secretion, hormone degradation, vitamin storage, plasma protein production (e.g. albumin), secretion of pro- and anti-clotting factors, and biotransformation, or the metabolism of toxicants and xenobiotics (1, 7).

The liver is divided into two lobes, the left and right with the latter being larger (2, 3). The lobes are then divided even further into lobules by small blood vessels and fibrous strands (1-3). The hepatic lobules are the anatomical units of the liver that include blood vessels and bile ducts in hexagonal-type cylinders (2 mm high by 1 mm in diameter) (**Figure 1.1A**) (3). The lobule contains lines of hepatocytes with a 10-15 μm distance in between, which is known as the liver sinusoid (**Figure 1.1B**) (3). Blood enters from the hepatic portal vein into the sinusoids and is then drained to the central vein, which is in the center of the lobule, before moving back into the hepatic vein and the body's circulation (3). The liver sinusoid is a microvascular unit with characteristics such as low oxygen tension (approximately 40 mmHg), low blood perfusion pressure (approximately

2-3 mmHg), low flow rates (approximately 407-451 um/s), and low Reynolds number (approximately 10^{-4}), indicating laminar flow (1, 8-10). This region houses the non-parenchymal cells (NPCs), exposes the hepatocytes to blood supply, and is responsible for biotransformation (1, 11, 12).

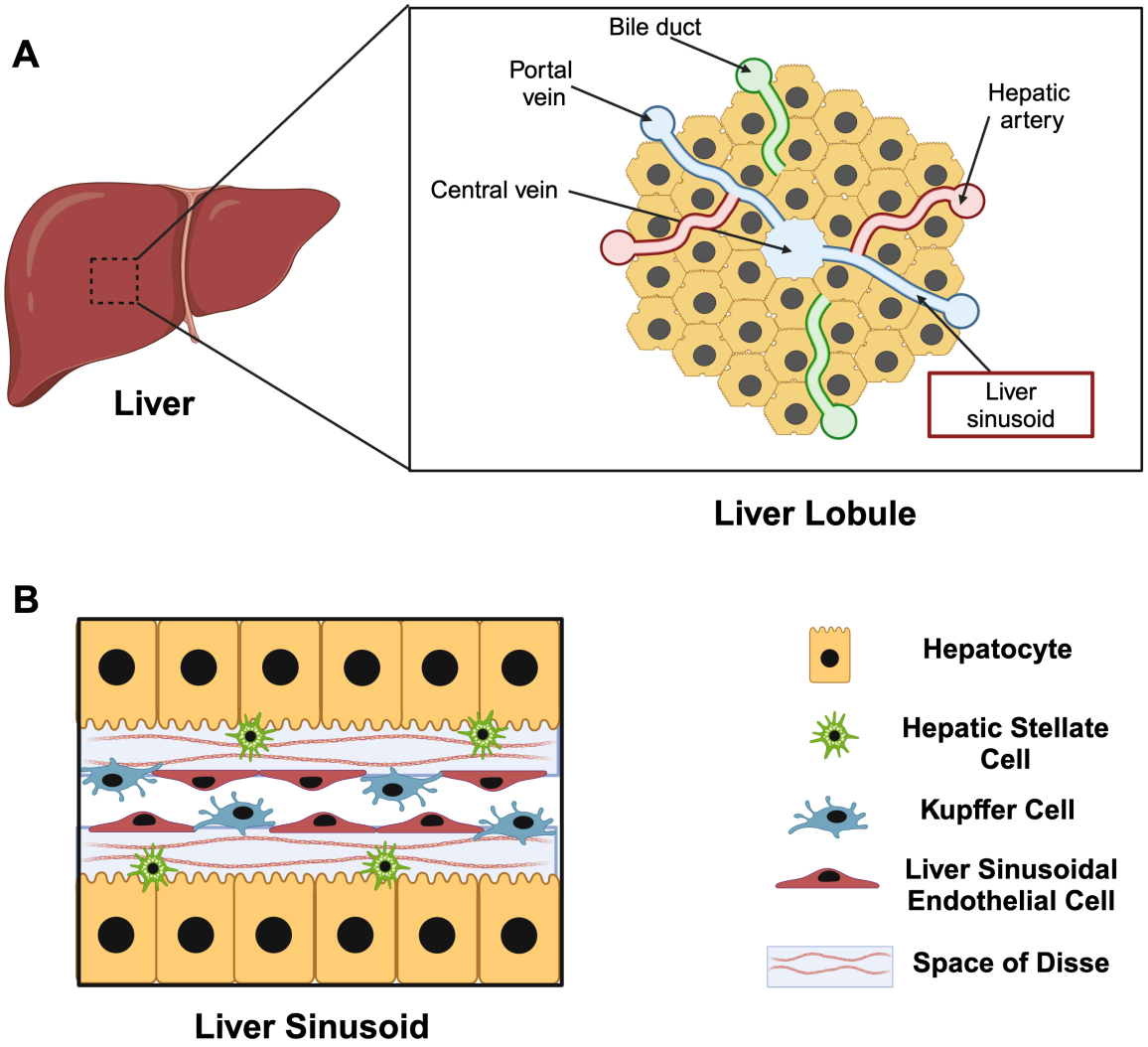

Figure 1.1 Schematic of (**A**) a lobule and (**B**) the sinusoid region in the liver.

There are four major cell types in the liver. The first cell type is the hepatocytes, which are the parenchymal (main) cell type in the liver. The perisinusoidal space, also known as Space of Disse, is an extracellular matrix (ECM)-rich region that separates the hepatocytes and the sinusoid (1,

12, 13). Hepatocytes perform several liver functions, including filtration, synthesis, and biotransformation, and comprise of 80% of hepatic cells (1, 7, 12, 14, 15). Hepatocytes are also polar which allows for spatial differences and various functions to be performed on certain sides within the cell (1, 16). On the basolateral membrane of hepatocytes, microvilli extend into the Space of Disse and allow for the absorption of molecules entering from the sinusoid (1, 16). Secretion of produced molecules occurs through the apical membrane (1, 16).

There are also three non-parenchymal cell types, which include liver sinusoidal endothelial cells (LSECs), Kupffer cells (KCs), and hepatic stellate cells (HSCs) (1, 7, 12, 14, 15). LSECs line the sinusoids and act as molecular sieves, thereby filtering molecules before they can enter hepatocytes (1, 17). These cells contain fenestrae, small openings, with a diameter of 100-300 nm, which control the entrance of molecules to hepatocytes, and express different scavenger receptors to clear the blood of waste metabolites (1, 17). The ratio of hepatocytes:LSECs *in vivo* is approximately 5:1 (1). KCs are the resident macrophages of the liver (1, 7, 12). They can also perform scavenger and phagocytic functions to remove any molecules that can be damaging to hepatocytes (1, 7, 12). Additionally, these cells can trigger an immunogenic response in response to a harmful product (12). The ratio of hepatocytes:KCs *in vivo* is approximately 10:1 (12, 15). HSCs are present in the Space of Disse and can revert between quiescent and activated (1, 13, 18). They are responsible for storing majority of the body's vitamin A reserve when quiescent (1, 13, 18). However, these cells can transform into myofibroblasts where they secrete ECM components to aid in liver repair and regeneration when activated during liver injury or stress (13, 18). This activation leads to progression of fibrosis, which could be caused by alcohol, steatohepatitis, or viral infection (18, 19). The ratio of hepatocytes:HSCs *in vivo* is approximately 15:1 (1).

Because of the intricacy of the environment and the array of vital functions the liver performs, developing an accurate and efficient model to study this organ remains a great area of interest (20-23). *In vitro* hepatic cultures are used to study liver function, disease, and toxicity to better solve healthcare issues (1, 7, 11, 12, 24, 25). However, there is a need to find a sustainable source of cells to further liver research (20-23).

1.2 Induced Pluripotent Stem Cells

Stem cells hold tremendous potential for advancing knowledge of embryogenesis and disease (26-30). They have been used in transplant protocols and tissue regeneration (28-32). Pluripotent stem cells (PSCs) are obtained from the inner cell mass of the blastocyst, which is after the zygote forms a ball of cells that is hollow in the middle (11, 27-31). These cells can then differentiate into cell types that originate from the three germ layers (endoderm, mesoderm, and ectoderm) that lead to all organs and tissues (11, 31). The most commonly known PSCs are embryonic stem cells (ESCs) (31, 32). However, ethical issues surrounding ESCs, such as obtaining them from a viable embryo, cause concern for their use (11, 27-31).

In 2006, Takahashi and Yamanaka were able to reprogram mouse dermal fibroblasts (somatic cells) to induced PSCs (iPSCs) through the addition of four transcription factors, Oct4, c-Myc, Sox2, and Klf4, by retroviral transduction (33, 34). Oct4 and Sox2 maintain pluripotency and self-renewal characteristics (35, 36). Klf4 and c-Myc enhance proliferation of the cells (37, 38). The same method was successful with human dermal fibroblasts in 2007 (**Figure 1.2A**) (33). Alterations to the reprogramming factors, including Nanog and Lin-28, have also been investigated (39, 40).There have been several established protocols that differentiate iPSCs to various cell types including cardiomyocytes, neurons, microglia, endothelial cells, osteoclasts, and hepatocytes (11, 41-45).

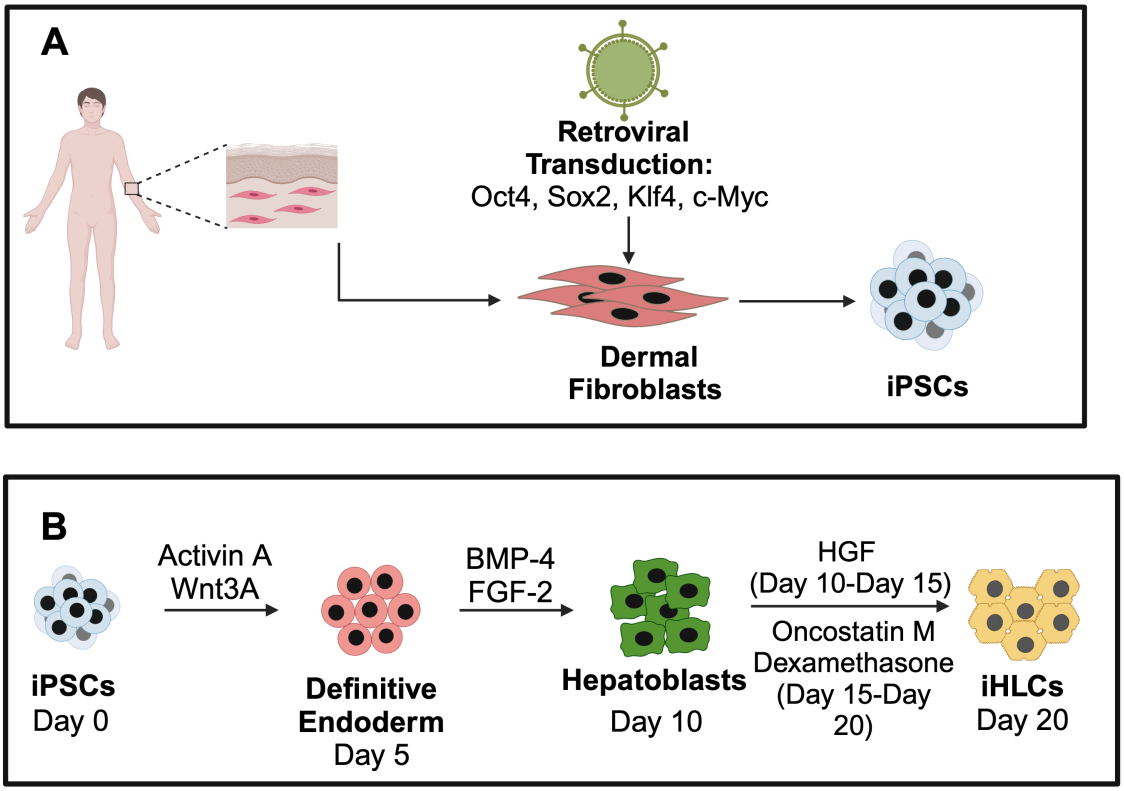

Figure 1.2 Schematic of the differentiation of (**A**) dermal fibroblasts to iPSCs and (**B**) iPSCs to iHLCs.

iHLCs are generated from iPSCs following a stepwise protocol that mimics liver embryogenesis (**Figure 1.2B**) (46). Similar protocols were used and developed with ESCs (45). The liver is generated from the endoderm germ layer (46). Activin A, involved in development of organs and tissues, and Wnt3a, which signals proliferation of cells, are added to iPSCs to differentiate them to the definitive endoderm (47, 48). This step takes five days (45). From there, the cells are transformed into hepatoblasts, or immature hepatocytes over the next five days (45). The addition of bone morphogenetic protein (BMP)-4 and fibroblast growth factor (FGF)-2 are responsible for development and regeneration of organs and tissues (49, 50). To achieve hepatocyte-like cells, Oncostatin M (OSM), hepatocyte growth factor (HGF), and dexamethasone are used (45). These three molecules are responsible for the maturation of hepatocytes, production of metabolic

enzymes, and maintenance of the cuboidal morphology of hepatocytes (51, 52). This protocol enhances the differentiation to hepatocytes (45, 53, 54). In the literature, iHLCs have been reported to exhibit characteristics of adult hepatocytes, such as glycogen storage, lipid metabolism, albumin and urea secretion, hepatocyte morphology, and expression of metabolic enzymes (11, 45, 46).

Primary human hepatocytes (PHHs) are mature cells that are derived from the liver and perform all hepatic functions (21). They are the preferred cell type for *in vitro* studies (11, 21, 55). However, these cells are typically obtained from donors, primarily through biopsies or cadavers, which can result in limited quantities (11, 21). Additionally, the donor's history and background can impact the function of hepatocytes, potentially affecting data obtained during experimentation (21). Other *in vitro* models have used hepatocarcinoma cells or hepatocyte cell lines, which are genetically modified and do not exhibit the same functions as primary hepatocytes (11, 21, 56).

In efforts to mitigate some of the issues that revolve around PHHs, iHLCs have been utilized for *in vitro* studies (11, 22, 45, 50, 57). They are highly proliferative, obtained from adult skin cells, and maintain the genotype of the host, making them ideal of patient-specific studies (28, 29). However, they express lower hepato-specific functions and fetal characteristics, which limits their current use (11, 20, 22, 28, 29, 57). For instance, these cells have been reported to express cytochrome P450 (CYP) 3A7 and alphafetoprotein (AFP), two proteins present in fetal livers, that are not present in adult hepatocytes (22, 57). Gene expression of hepatic enzymes such as CYP2E1, CYP2C9, and CYP2A6 can be downregulated up to 40,000-fold in iHLCs compared to PHHs (55). To improve these lower functions, several methods have worked towards maturing iHLCs so that their use can become more widespread in the liver research community.

1.3 Maturation of iHLCs

1.3.1 Exogenous Chemicals and Small Molecules

In the literature, various studies have reported different protocols to mature iHLCs. Most common is the addition of exogenous chemicals and small molecules (54, 58-60). Several methods alter the chemical cocktails used to differentiate iPSCs to iHLCs on different temporal scales, which has led to discrepancies in the results (50, 54). Chemical cocktails have included insulin, epidermal growth factor (EGF), vascular endothelial growth factor (VEGF), retinoic acid, vitamin K, and ascorbic acid at different steps and concentrations in the differentiation protocol (54, 58-60). Various isoforms of fibroblast growth factor (FGF) have been used, including FGF2, FGF4, and b-FGF (basic FGF) (54, 58-60). The concentration (μg – ng) of each of these supplements varies and is much higher than what is typically found *in vivo* (pg) (21, 54). For example, HGF is administered from 20-100 ng/ mL in several iPSC differentiation protocols, however, even *in vivo,* concentrations ranged from 0.2-12.5 ng/ mL in fetal tissues (54, 61).

Kaserman et. al. added VEGF, EGF, and transforming growth factor-alpha (TGF-α) to their culture medium to further differentiate iPSCs from the definitive endoderm to the hepatoblast stage (60). Vitamin K was also used as a supplement to promote the hepatic lineage (60). However, flow cytometry analysis of the cells after 25 days showed that these additional supplements resulted in iHLCs expressing FOXA1, a transcription factor that downregulates differentiation into the hepatic lineage (60). Si-Tayeb et. al. used defined culture conditions to differentiate iPSCs to iHLCs in a stepwise protocol with no overlap in supplements at every stage (45). Their protocol resulted in more than 80% of albumin-expressing cells, a sign of maturation (45). Additionally, the iHLCs produced key hepatic functions, such as glycogen storage, uptake of lipids, and secretion of lipids. The iHLCs also exhibited hepatocyte morphology (45). However, more than half of the measured mRNA of phase I and II drug metabolizing enzymes including CYP1A2, CYP2C9,

CYP3A4, UGT1A1, and UGT1A6, were significantly lower expressed in iHLCs compared to a human liver, indicating these cells were immature (45).

Exogenous molecules have also been administered at different steps in the differentiation protocol to enhance certain pathways leading to liver maturation (46, 54, 62). These molecules are typically not present *in vivo* (46, 54, 62). A study by Du et. al. showed that using a small molecule inhibitor, CHIR99021, to inhibit the GSK-3β pathway can indirectly activate the Wnt3a pathway to differentiate iPSCs into the definitive endoderm (50). Cells treated with 3 μM CHIR99021 showed expression of hepatic nuclear factor (HNF) 4α, AFP, and albumin (50). Despite the addition of the small molecule, CYP1A2 activity and albumin secretion were up to 4-fold lower compared to PHHs.

Siller et. al. used a combination of small molecules including dimethyl sulfoxide (DMSO) and Ile-(6) aminohexanoic amide (dihexa), an HGF agonist, along with dexamethasone to further mature the cells after they exhibited markers of the definitive endoderm stage (63). These small molecules were used instead of growth factors to provide an alternative method of differentiation without the need for recombinant proteins (63). After treatment with this cocktail, cells expressed mature markers such as albumin, CYP3A4, and alpha-1 antitrypsin (A1AT) (63). Although these molecules can induce differentiation, DMSO and dihexa do not mimic signaling molecules that are present during liver embryogenesis (63).

DMSO has been used for stem cell differentiation, specifically towards the hepatoblast lineage. However, studies have reported varying results whether DMSO can be beneficial or toxic towards cells (54, 64-66). Du et. al. reported an optimal concentration range for DMSO was 0.25-0.5% v/v, whereas 1% v/v caused toxicity (50). However, Siller et. al. reported that 1% v/v encouraged cells to differentiate towards the hepatoblast stage, where >87% of cells expressed AFP and

HNF4α (63). A recent study by Krumm et. al. also reported the use of 1% v/v DMSO in differentiating iPSCs to hepatoblasts (67). Proteomic and transcriptomic analyses revealed that cells exhibited high expression of HNF4α and FOXA2, indicating further differentiation to hepatoblasts (67). Transcriptomic analysis concluded that the iHLCs generated from this protocol expressed mRNA for proteins involved in gluconeogenesis, β-oxidation, and the TCA cycle (67). However, protein expression levels, such as cytochrome P450 (CYP450) and drug metabolism enzymes (genes not specified) were downregulated up to approximately 9-fold compared to PHHs (67).

iPSCs have also been differentiated into HLCs with the use of valproic acid and sodium butyrate, both epigenetic modifiers (68, 69). They serve as histone deacetylation inhibitors which guide the differentiation of iPSCs to hepatic states (68, 69). A previous study also used valproic acid in the reprogramming protocol without the use of c-Myc, which has been used to transform somatic cells to iPSCs, however, it can also be a proto-oncogene (69). To investigate if valproic acid would exhibit the same effects on iPSC differentiation to hepatic cells, Kondo et. al. administered this small molecule for various time lengths and at different days after the cells reached the hepatoblast stage (68). Highest mRNA expression levels of albumin were achieved when valproic acid was administered to cells for seven days after immediately reaching the hepatoblast stage, indicating maturation (68). Cells treated with valproic acid also had a statistically significant increase in mRNA expression levels of various drug metabolizing enzymes, such as CYP2C9, CYP2C19, CYP3A4 and UDP glucuronosyltransferase (UGT) 1A1 (68).

1.3.2 Spheroids and Culture Systems

Spheroid cell culture systems, or aggregates of cells in suspension, have been widely used in the literature to improve hepatic function of primary hepatocytes, cell lines, and iHLCs (21, 54, 70, 71). Such hepatic functions that have been improved in iHLC spheroid cultures include protein

secretion, enzyme expression, as well as hepatic features, such as bile canaliculi (21, 70, 71). These spheroids can be formed in monocultures of just hepatocytes, or in co- or multi-cultures including LSECs, human umbilical vein endothelial cells (HUVECs), HSCs, endothelial cells, cholangiocytes, human adipose microvascular endothelial cells (HAMECs), and mesenchymal stem cells (MSCs) (72-76). However, spheroids can form a necrotic center indicating cell death (22). Larger spheroids may even result in variations across the culture system, where the inner and outer cells may behave differently due to differences in signaling (22).

Ramli et. al. differentiated iPSCs by forming spheroids at the definitive endoderm stage (70). The spheroids were maintained until they achieved the hepatoblast stage and then disassociated (70). The cells were reseeded in a high-throughput manner to form spheroids in suspension (70). Bile canaliculi was visualized in the spheroids (70). Additionally, secretion of albumin and apolipoprotein B was detected in the cultures. However, both properties were approximately 3-fold lower in comparison to PHHs (70). The authors stated that the spheroids still had fetal-like characteristics, as exhibited by AFP and CYP3A7, a CYP450 enzyme that is predominantly present in fetal livers, expression. (70). This study was primarily conducted to investigate the efficacy of drug-induced cholestasis in iHLC-spheroids (70). The authors noted that the lack of other NPCs, such as KCs and HSCs, limits their model due to the importance of additional cell types in recapitulating the liver environment (70).

The encapsulation of spheroids with extracellular matrix (ECM) material, e.g. Matrigel®, has been used to maintain PHHs *in vitro* (77, 78). A similar approach was adapted to six iPSC cell lines to investigate if the culture system promoted maturation and an ability to differentiate to the hepatocyte-like stage (73). A specific iPSC-line, Dotcom, showed the highest secretion and mRNA expression of albumin (73). Compared to monolayers, there was a statistically significant increase in CYP2C9 and CYP3A4 activity in spheroids (73). However, the baseline CYP activity

was up to approximately 5-fold lower in iHLC spheroids compared to cultures assembled with PHHs (73). Another comparison was conducted on spheroids assembled with either iHLCs or HepG2 (a hepatocarcinoma-derived cell line) cells (79). After treatment with several hepatotoxic drugs, including clozapine, flutamide, isoniazid, and tacrine, it was concluded that iHLC spheroids had statistically significant lower cell viability than when the compounds were administered to HepG2 cultures (79). These results indicate that iHLCs were more sensitive to toxicants than HepG2 and, therefore, could be a better source for drug screening studies (79). However, the cell viability of iHLC spheroids after toxicant administration was up to approximately 70% higher than PHH cultures (79). Although, this study showed that iHLC spheroids were still a better source for *in vitro* studies than hepatic cell lines, they exhibited significantly lower liver-related functions compared to PHHs (79).

The addition of other cells induces intercellular signaling to increase hepatic function in cell cultures (72-76). Ardalani et. al. reported the assembly of iHLC spheroids that included iPSC derived-endothelial cells (iECs), LSECs, HSCs, and cholangiocytes (72). The highest increase in albumin and urea synthesis was observed in spheroids with iHLCs and LSECs, compared to iHLC mono-spheroids and 2D cultures of iHLCs (72). iHLC spheroids that included iECs, HSCs, and LSECs and HSCs together still exhibited higher albumin and urea secretion compared to monocultures (72). Induced CYP3A4, CYP2C9, and CYP1A2 enzyme activity was significantly higher up to 4-fold in iHLC spheroids that included LSECs, LSECs and HSCs, or iECs (72). This study emphasized how the inclusion of NPCs in a 3D model with iHLCs induced maturation and higher metabolic activity (72).

1.3.3 Scaffolds and Environment

The environment in which iHLCs are cultured can influence maturation and improve hepatic function (1, 80). The liver ECM includes proteins such as collagen, fibronectin, and laminin that

induce cell-environment signaling *in vivo* and *in vitro* (1, 13, 80). The ECM provides an environment that is conducive for migration, differentiation, and cell signaling, (80). Similar concepts have been adapted to investigate stem cell differentiation and maturation *in vitro* (81-83). Wang et. al. used a rat liver-derived decellularized ECM scaffold, a 3D bio-plotted poly-L-lactic acid (PLLA), and a type 1 collagen and Matrigel®, a commercially available mouse-derived matrix material, construct to compare maturation of iHLCs (82). In both 3D scaffolds, iHLCs proliferated 1.67-1.75-fold throughout a 14-day culture, compared to no change in cell numbers in a type 1 collagen with a Matrigel overlay sandwich control (82). rt-PCR determined significant increases in CYP1A2, CYP2C9, and CYP3A4 in iHLCs cultured in the ECM scaffold compared to the sandwich control, although the expression of these enzymes was still up to approximately 6-fold lower than PHHs (82). Albumin synthesis was significantly higher throughout the culture period in iHLCs cultured in the ECM scaffold compared to the sandwich control (82). However, AFP synthesis in all iHLC cultures was significantly higher by approximately 4-fold compared to PHHs (82). Although the decellularized-ECM scaffold enhanced hepatic functions and enzyme expression compared to sandwich controls with just type 1 collagen and Matrigel®, the iHLCs were still significantly immature compared to PHHs (82).

Foregut progenitors were encapsulated in Matrigel® before growth factors and supplements were added to continue differentiation into iHLCs (84). The presence of bile canaliculi and secretion of bile acids (approximately 125 μmol/ day/ 10^6 cells) on Day 27 indicated that the organoids were polarized and capable of performing hepatic functions (84). Additionally, the spheroids expressed hepatic markers such as albumin, CYP2C9, and CYP7A1 as well as other bile and drug metabolism markers including multidrug resistance associated protein (MRP) 1 and 2 and bile salt export pump (BSEP) (84). However, gene expression was up to 1.5 orders of magnitude lower than PHHs (84). Additionally, AFP expression was 4 orders of magnitude higher in iHLC spheroids indicating that these cells still exhibited immature markers (84).

Other biomaterials that have attempted to mature iHLCs include PLLA-polycaprolactone (PCL) hybrid constructs, poly(ethylene glycol), and cellulose nanofibril substrates (83, 85, 86). A PLLA-polycaprolactone hybrid construct showed that iHLCs expressed hepatic functions including glycogen accumulation and lipoprotein uptake as well as typical morphology and characteristics, including the presence of lipid droplets (85). An inverted colloid crystal fabricated from polyethylene glycol with collagen I, fibronectin, and laminin was used to form spheroids of iHLCs which had greater mRNA expression levels of mature hepatic markers, such as albumin, CYP3A4, and CYP2C9 (86). Cellulose nanofibrils, a biocompatible material, were used to mature iHLCs in comparison to Matrigel® substrates (83). Flow cytometry analysis revealed that the iHLCs expressed mature marker asialoglycoprotein receptor (ASGPR) 1, which is present on the basolateral membranes of hepatocytes, indicating polarity was achieved (83). However, RT-PCR resulted in similar expression profiles between cellulose nanofibril and Matrigel® differentiated iHLCs, indicating the material did not further mature the cells (83).

1.3.4 Genetic Reprogramming

Reprogramming somatic cells directly to a hepatic lineage is yet another method to improve the immaturity and fetal-like characteristics of iHLCs (87-93). This method tries to bypass differentiation to iPSCs by overexpressing genes that lead to a hepatic fate (87-93). This method utilizes a combination of transcription factors that are typically expressed during the hepatoblast stage (87-93). Although variation exists between the targeted liver-enriched transcription factors (LETF), all studies have included the use of HNF4α (87-93). This transcription factor is responsible for initiating liver development and regulating hepatic genes expressed (91). Without HNF4α, there was a decrease in the expression of hepatic genes such as albumin and alpha-1 trypsin, compared to when it was used with FOXA3 and HNF1α (93).

Several combinations of transcription factors have been studied to induce the hepatic lineage from fibroblasts (87-93). Infection with lentiviruses carrying plasmids of HNF4α, HNF1α, and FOXA3 resulted in hepatocyte morphology, uptake of low-density lipoproteins, lipid droplet accumulation, and glycogen storage (93). Although, CYP450 expression levels were still lower compared to PHHs up to 200-fold (93). Induction of CYPs resulted in similar patterns (93). Additional transcription factors that have been included in combinations of reprogramming methods include HNF1β, HNF6, PROX1, ATF5, CEBPA, FOXA1, FOXA2, GATA4, GATA6, and HHEX (87-90, 92).

However, reports have varying results about each of these genes are their capability to mature cells into hepatocytes. For example, HNF1β was investigated to replace HNF1α, but resulted in significantly lower expression of albumin (62). Similarly, reprogramming with genes in the Forkhead Box set (FOXA3 and FOXA2), which is essential for hepatic conversion, have even been used combinatorially or interchangeably (88). One study reported the use of both FOXA3 and FOXA2 in their reprogramming methods (89). Another study reported the use of a FOXA2 alone with HNF4α, which resulted in iHLCs with unstable phenotypes, leading to concerns of applicability and safety (87). All of these variations have still led to a similar conclusion that iHLCs continue to exhibit lower hepato-specific functions compared to PHHs (87-90, 92). The reprogramming method does genetically alter the cells rather than allowing for a dynamic maturation process from signals in the culture media or system.

MicroRNAs (miRNAs) have also been utilized in reprogramming. miRNAs regulate the cell post-transcriptionally and control protein levels (54, 94, 95). Various hepatic-specific miRNAs reported in the literature include mi-RNA-424, -542-5p, 148a, 542-5-, -106a, -574-3p, -451, and -122 (54, 94, 95) although, miRNA-122 is the most widely reported and has been extensively studied (96). This miRNA is the most abundant in a developed liver and has been implicated in several hepatic

pathways (95, 96). miRNA-122 can stimulate LETFs and induce hepatic differentiation (95, 96). So far, miRNAs have not been used to reprogram somatic cells. Instead, studies have used combinations to induce a hepatic lineage in MSCs (54, 94, 95).

1.4 Research Objectives

Despite the variations in protocols, complete maturation of iHLCs still has not been achieved. If iHLCs are to be used as a sustainable replacement for PHHs, they should exhibit functions and markers characteristic of an adult phenotype. There is a critical need for a systematic approach to generate mature iHLCs that can be widely adapted for future *in vitro* drug, disease, and patient-specific studies.

Hypothesis: We hypothesize that incorporating NPCs, including LSECs and KCs, that can secrete different signaling factors at concentrations found *in vivo* will mature iHLCs. These cells have been reported to be involved in liver embryogenesis and can increase hepatocyte functionality. Such a process can be used more consistently across the liver and iPSC research community instead of relying on complex cocktails of reagents that need to be administered in a specific temporal sequence, using genetic modifications that alter the transcription of mRNA and translation of proteins, or using culture systems that vary in size, cell numbers, and ratios. In this work, we aim to understand how iHLCs compare to PHHs and demonstrate how these cells may be matured in a 3D multicellular human liver organoid solely through cell-cell signaling. Our research objectives are the following:

1. Investigate differentially expressed genes between iHLCs and PHHs that explain the observed phenotypic differences.
2. Assemble 3D multicellular human liver organoids with iHLCs, LSECs, and KCs to investigate if maturation occurs.

3. Compare hepatocyte markers and functions between organoids assembled with iHLCs and PHHs to examine differences in characteristics between the two cell types.
4. Measure the secretion of molecules to understand the mechanism and regulation of maturation in iHLC organoids.

Chapter 2: Comparative Transcriptomic and Phenotypic Analysis of Induced Pluripotent Stem Cell Hepatocyte-Like Cells and Primary Human Hepatocytes

Chapter 2 reprinted with permission from Gandhi, N., Wills, L., Akers, K., Su, Y., Niccum, P., Murali, T.M., and Rajagopalan, P., Comparative Transcriptomic and Phenotypic Analysis of Induced Pluripotent Stem Cell Hepatocyte-Like Cells and Primary Human Hepatocytes. Cell and Tissue Research, 2024. ***396****: p. 119-139.*

AUTHORS' CONTRIBUTIONS

N.G performed statistical analysis, interpreted the data, and wrote the manuscript. L.W. performed the cellular work and assessments. K.A. performed the RNA-seq analysis and interpreted the results. Y.S. assisted with revisions and analyzing the RNA-seq data. P.N. assisted with revisions to the manuscript. T.M.M. and P.R. designed the scope of the paper, supervised, and wrote the paper.

2.1 Introduction

Since their discovery, induced pluripotent stem cells (iPSCs) have gained attention for their potential in various applications for *in vitro* and *in vivo* applications, such as organoids, toxicity and drug studies, disease modeling, and regenerative medicine (26, 27, 97). iPSCs were discovered in 2006 by Takahashi and Yamanaka (34). Since then, iPSCs have been differentiated into neural, intestinal, liver, retinal, cardiac, and muscle cells (11). Various protocols have been reported to differentiate iPSCs into hepatocyte-like cells (iHLCs) (45, 53, 60, 67, 76, 98-100). The differentiation protocols for iHLCs are based on procedures used to obtain hepatocytes from embryonic stem cells (ESCs) (11, 45, 53, 60, 67, 76, 98). The first step is to obtain the definitive endoderm through the addition of Activin A and Wnt3a (45, 53, 67, 76, 98). Thereafter, cells are targeted towards hepatoblasts, or immature hepatocytes, through the addition of bone

morphogenetic factor-4 (BMP-4) and fibroblast growth factor-2 (FGF-2) (45, 53, 67, 76, 98, 100). The hepatoblasts are further matured to hepatocytes by adding hepatocyte growth factor (HGF) followed by a mixture of oncostatin M and dexamethasone (45, 53, 60, 67, 76, 98, 99). Each of these steps leads to the development, maturation and functionality of hepatocytes (45, 53, 60, 67, 76, 98-100). Other molecules used for differentiation of iPSCs to iHLCs include VEGF, EGF, TGF-α and vitamin K (54, 60). Adding chemical cocktails is the most common method for the maturation and differentiation of iHLCs (45, 53, 60, 67, 76, 98, 99). However, other methods include the addition of small molecules (DMSO, valproic acid), different culture systems (spheroids, scaffolds, organoids), and genetic reprogramming (transcription factors and miRNAs) (50, 54, 71, 95, 101). The generation of iHLCs is typically confirmed by albumin expression, accumulation of glycogen, urea synthesis, lipid metabolism and expression of cytochrome P450 (CYP450) enzymes (45, 53, 60, 67, 76, 98-100). However, studies have reported that iHLCs exhibit lower expression of enzymes involved in metabolism and biotransformation (45, 99, 100).

Traditionally, primary human hepatocytes (PHHs) are considered to be the most relevant for *in vitro* liver investigations (11, 21). However, disadvantages of these cells include invasive retrieval, significant donor variability and limited availability (11, 21, 102).

Genome-wide transcriptomic analyses have been conducted to investigate the similarities and differences between iHLCs and either the liver *in vivo*, PHHs or hepatic cell lines (56, 79, 103, 104). We first focus on reports that have shown similar characteristics between iHLCs and mature hepatic cells (56, 79, 103, 104). Sjogren et. al. reported that iHLCs were more similar to PHHs than Huh7 and HepRG cells. Their results indicated a lower number of differentially expressed genes involved in nine apoptotic pathways (genes not reported) (56). Another comprehensive gene expression analysis study compared iHLCs to PHHs from six donors, as well as several cell lines including HepRG, Huh7, HepG2, and HepG2/C3A (79). The results indicated that iHLCs

were more closely related to PHHs compared to the hepatoma cell lines, except HepRG, in drug metabolizing pathways, as determined by principal component analyses (PCA) (79). While iHLCs have been shown to exhibit phenotypic characteristics that emulate mature hepatic cells, significant differences have also been revealed. The same study also showed that CYP3A7, an enzyme expressed in fetal livers, had a higher relative gene expression in iHLCs (11.9-13.4) compared to PHHs (8.5) (79). A qPCR analysis of drug metabolizing pathways also showed that the expression levels of CYP2E1 and CYP3A4, two members of the CYP450 enzyme family, in iHLCs were 0.2% and 0.7%, respectively, of the PHH values (56). A transcriptomic analysis using RNA-sequencing (RNA-seq) also compared iHLCs from two commonly used differentiation protocols and PHHs (104). This study focused on long non-coding RNAs and transcription factors involved in the differentiation pathways of iPSCs to iHLCs (104). Results showed that transcriptional regulators such as RARG, E2F1, and FOXH1, which are involved in hepatocyte maturation, were downregulated in iHLCs compared to PHHs, which could contribute to their immaturity (104).

To further understand the variations between PHHs and iHLCs, we measured gene expression levels in each cell type using RNA-seq data. We computed genes that were differentially-expressed between the two types of cells (105). Then, we investigated pathways that were upregulated in PHHs compared to iHLCs as revealed by analysis of RNA-seq data. We focused on specific genes involved in pathways that contribute to differences between iHLCs and PHHs, such as drug metabolism, hepatocyte phenotype, bile secretion and the citric acid cycle. To support the ‘omic data, we have validated the differences in gene expression with cellular analysis. By understanding the transcriptomic differences between iHLCs and PHHs, we provide a basis for reports of experimentally observed differences in their functional capabilities.

2.2 Materials and Methods

RPMI 1640, B-27 supplement, phosphate buffered saline (PBS), Tris-HCl, ethylenediaminetetraacetic acid (EDTA), ethanol (EtOH), bovine serum albumin (BSA), and TrypLE™ were obtained from Thermo Fisher Scientific (Waltham, MA). Gentamicin, collagenase, β-mercaptoethanol, Tris, sodium dodecyl sulfate (SDS), 7-methoxy-4-trifluoromethylcoumarin (MFC), 7-hydroxy-4-trifluoromethylcoumarin (HFC), β-glucuronidase/arylsulfatase, and acetaminophen (APAP) were purchased from Millipore Sigma (St. Louis, MO). Oncostatin M was obtained from R&D systems (Minneapolis, MN). Dexamethasone was purchased from MP Biomedicals (Solon, OH).

2.2.1 Extraction of Type 1 Collagen

Collagen was extracted from rat tails as described in previous reports (7, 15). Briefly, tendons obtained from rat tails were dissolved in acetic acid and were purified through centrifugation at 13,000 x g. Collagen was precipitated with 30% (w/v) sodium chloride and then dialyzed in 1 mM hydrochloric acid. The solution was sterilized with chloroform and maintained at a concentration of 2.0–3.0 mg/mL at a pH of 3.1. Each well of a 6-well tissue culture polystyrene (TCPS) plate was coated with 0.5 mL of 1.1 mg/ mL collagen and allowed to gel for approximately 45 minutes at 37℃.

2.2.2 Culturing iHLCs and PHHs

iHLCs (iCell Hepatocytes 2.0) were purchased from Fujifilm (Santa Ana, CA). Cells were seeded at a density of 300,000 cells/ cm^2 on collagen gels (1.1 mg/mL) and cultured according to the manufacturer's protocol. Culture medium was changed every 24 h. Plating media consisted of RPMI supplemented with Oncostatin M (10 μg/mL), dexamethasone (5 mM), gentamicin (50 mg/mL), B-27 supplement (2% v/v), and iCell Hepatocytes 2.0 medium supplement. Cells were

maintained in maintenance media, containing RPMI, dexamethasone (5 mM), gentamicin (50 mg/ mL), B-27 supplement (2% v/v), and iCell Hepatocytes 2.0 medium supplement, five days after seeding. iHLC monocultures were maintained for up to seven days prior to conducting liver-specific testing. To assemble the collagen sandwich (CS), a second layer of collagen (1.1 mg/mL) was added seven days after iHLC seeding (**Figure 2.1A**). Spent culture medium was collected every 24 h and stored at -80ºC until analyzed. Cells were maintained at 37ºC in a humidified environment at 5% carbon dioxide.

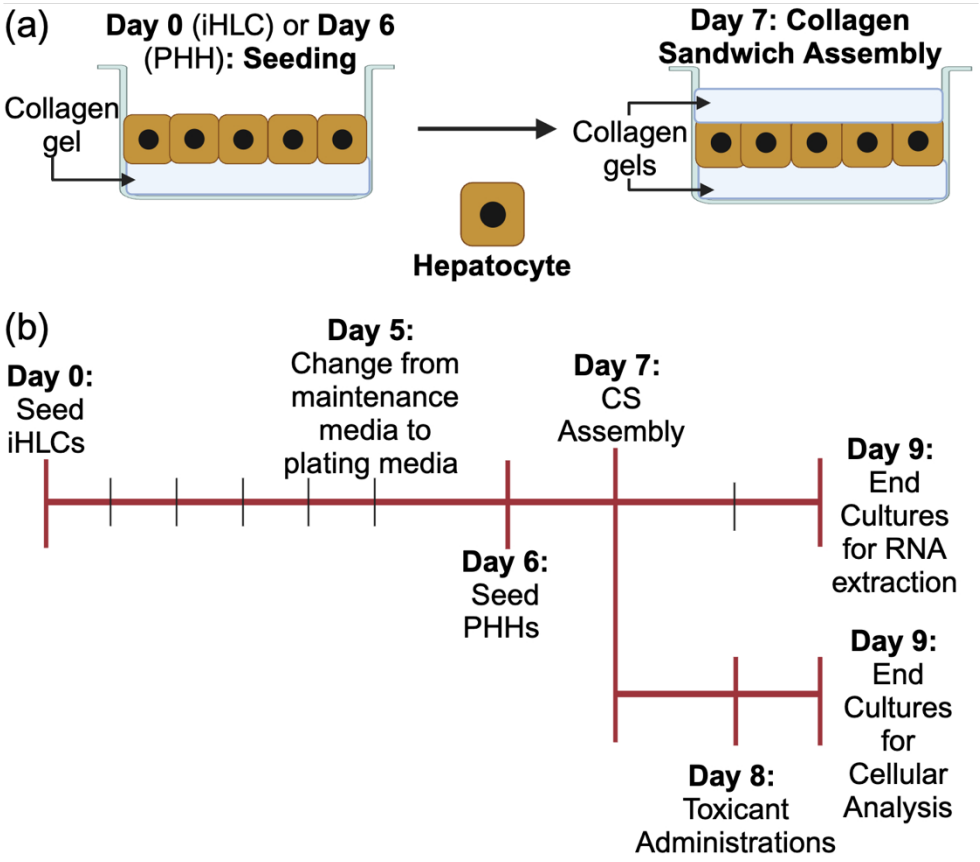

Figure 2.1 (**A**) Assembly of collagen sandwich hepatocyte cultures. (**B**) Timeline for iHLC and PHH cultures for the RNA-seq experiment.

PHHs were obtained from Sekisui XenoTech (Kansas City, KS). PHHs were cultured and maintained according to the manufacturer's protocol. PHHs were initially seeded on collagen gels (1.1 mg/mL) at a density of 560,000 cells/ well for 6-well TCPS plates and 35,000 cells/ well for

96-well plates (12). Briefly, cells were thawed in manufacturer supplied OptiThaw media and plated in OptiPlate. From there, cells were maintained in OptiCulture. CS cultures were assembled 24 h post-seeding as previously described (**Figure 2.1A**). Spent culture medium was collected at every 24 h and stored at -80ºC until analyzed. Cells were maintained at 37ºC in a humidified environment at 5% carbon dioxide.

2.2.3 Extraction of RNA from PHHs and iHLCs

RNA extraction was conducted on cells when thawed immediately after cryopreservation as well as from cultured iHLCs and PHHs. The extraction was conducted on cells of the same lot number and donor. The cells were mixed with RNAprotect Cell Reagent (Qiagen, Hilden, Germany) and stored until extraction. iHLC and PHH cultures were detached from collagen-coated TCPS plates upon the addition of TrypLE™ and collagenase, respectively (12, 14, 15, 106). After centrifugation and aspiration of the supernatant, the remaining pellet was re-suspended in RNAprotect Cell Reagent.

RNA extraction was conducted using the RNeasy Plus Micro Kit (Qiagen) following the manufacturer's protocol. Briefly, cells were suspended in the RNAprotect Cell Reagent, centrifuged, and re-suspended in RLT buffer supplemented with β-mercaptoethanol (14.3 M). The lysate was homogenized using QIAshredder spin columns. The homogenized lysates were transferred to gDNA Eliminator spin columns and the resulting solution was mixed with 70% v/v ethanol. The solution was centrifuged through the RNeasy MinElute spin column. Buffer RW1, Buffer RPE, and 80% v/v ethanol were added sequentially to the spin columns. The final RNA collection step was completed by centrifuging RNase-free water through the spin columns. Samples were stored at -80ºC until further analysis.

2.2.4 RNA-sequencing

The RIN value ranges for samples used in the present study are shown in **Table 2.1**. Briefly, the total RNA was converted for sequencing into a strand-specific library using Illumina TruSeq Stranded mRNA HT Sample Prep Kit (Illumina, San Diego, CA) and Illumina's Next Seq/ NovaSeq. The cleaved RNA fragments were converted to cDNA using reverse transcriptase and random primers and prepared for library enrichment. After 13 cycles of PCR, 15 individually indexed cDNA libraries were pooled and sequenced on Illumina NextSeq high Output 150 cycle kit to generate approximately 25 million paired end reads.

Table 2.1 RIN ranges for samples used in RNA-seq measurements.

Sample	**RIN Range ($n \geq 3$)**
iHLCs, Day 0	9.6 – 9.8
iHLCs, Day 9	9.7
PHHs, Day 6	7.7 – 8.1
PHHs, Day 9	7.5 – 7.9

2.2.5 Differential Gene Expression Analysis

The RASflow workflow was used for the alignment, gene counting, and differential gene expression analysis of the RNA-seq samples. HISAT2 was used to align RNA-seq reads against the GRCh38 cDNA transcriptome obtained from ENSEMBL (107-109). Gene counting was performed using the featureCounts program before applying PCA and t-distributed stochastic neighbor embedding (t-SNE) for linear and non-linear dimensionality reduction, and ggplot2 for hierarchical clustering to visualize the resulting gene expression matrix (110-113).

Samples for RNA-seq analysis were collected from iHLCs and PHHs on Days 0 and 6, respectively, and on Day 9 for both cell types. DESeq2 was used to perform differential gene expression analysis (114). The procedure of Benjamini-Hochberg was applied to adjust for multiple hypothesis testing. Genes with false discovery rate (FDR) adjusted *p*-values < 0.05 were

selected as differentially expressed. ClusterProfiler was used to identify KEGG Pathways and Gene Ontology (GO) Biological Processes enriched in each gene set (115, 116). Enriched terms with *p*-values < 0.05 were selected as over-represented or under-represented in each comparison.

2.2.6 Administration of Toxicants to iHLC and PHH Cultures

APAP and EtOH were dissolved in hepatocyte media and administered to cultures 24 h after CS models were assembled (Day 8). APAP was administered at 2.5 mM (LC_{50} for humans, lethal concentration 50) and 5 mM (2 X LC_{50} for humans), respectively (12, 117). EtOH was also added at 80 mM (½ LC_{50} for humans) and 160 mM (LC_{50} for humans) (12, 117).

2.2.7 Immunofluorescence Measurements of iHLCs and PHHs

iHLC and PHH cultures were fixed in a 2% (v/v) glutaraldehyde solution in PBS (1 X). The cells were then sequentially exposed to a 0.1% (v/v) Triton-X 100 solution in PBS (1 X) and a 1% (w/v) BSA/ PBS (1 X) blocking solution with 1.5% (v/v) goat serum. Intracellular albumin was identified using a primary polyclonal sheep anti-human serum albumin antibody (Abcam, Cambridge, MA) followed by incubating with a DAPI-conjugated secondary antibody (Thermo Fisher Scientific). Bile canaliculi were identified using a primary monoclonal mouse anti-human CD26 antibody (Thermo Fisher Scientific) followed by a TRITC-conjugated secondary antibody (Abcam). Actin was stained with rhodamine phalloidin (Thermo Fisher Scientific). Imaging was conducted on a Zeiss LSM 880 confocal microscope.

2.2.8 Measurement of Urea Secretion

Spent culture medium was assayed for the secretion of urea using a colorimetric BUN kit (StanBio Laboratory, Boerne, TX) (7, 14, 15). The urea concentration was determined through absorbance

measurements at 520 nm. A standard curve was developed by diluting urea in hepatocyte medium.

2.2.9 Measurement of DNA

DNA measurements were performed using the Quant-iT PicoGreen kit (Thermo Fisher Scientific). iHLCs and PHHs were released from gels by treating cultures with TrypLE™ or collagenase, respectively. Cell suspensions were collected, pelleted, and re-suspended in a 0.1% (w/v) SDS solution containing EDTA and Tris-HCl. Fluorescence was measured at an excitation/emission wavelength of 480 and 520 nm, respectively (118). A standard curve was generated by diluting the provided Lambda DNA. The original sample were diluted 10X in TE buffer prior to being assayed.

2.2.10 Measurement of the Activity of Cytochrome P450 2E1 (CYP2E1)

CYP2E1 activity was measured 24 h after toxicant administration (Day 9) (12, 119). CYP2E1 enzymatic activity was measured through the metabolic conversion of MFC to HFC. 10 μM of MFC was added to the cultures and allowed to incubate at 37ºC for 1 hour. The culture medium was collected and combined with β-glucuronidase/arylsulfatase and 0.5 M acetic acid. The mixture was incubated at 37ºC for 2 h. An equivalent volume of a 0.25 N Tris in 60% acetonitrile (v/v) was added to quench the reaction. The concentration of HFC was measured at an excitation/emission wavelength of 410 and 510 nm, respectively and compared to a standard curve to calculate enzymatic activity.

2.2.11 Measurement of Glutathione (GSH)

Glutathione (GSH) was measured 24 h after toxicant treatment (Day 9) using the GSH-Glo™ Glutathione Assay (Promega, Madison, WI). Cultures were incubated with Luciferin-NT and

Glutathione S-Transferase. Luciferin Detection Reagent was added to generate a luminescent signal which was compared to controls to determine changes in GSH (12).

2.2.12 Analysis of Mitochondrial Membrane Integrity

Mitochondrial membrane integrity was measured using the JC-1 Mitochondrial Membrane Potential Detection Kit (Biotium, Fremont, CA). The cationic JC-1 dye (5,5',6,6'-tetrachloro-1,1',3,3'-tetraethylbenzimidazolylcarbocyanine iodide) was added to the cell cultures 24 h after toxicant administration (Day 9) and incubated for 15 minutes at 37ºC. Fluorescence was measured to determine the numbers of both healthy (red; measured at an excitation/ emission wavelength of 550 and 600 nm, respectively) and damaged (green; measured at an excitation/ emission wavelength of 485 and 535 nm, respectively) cells. The ratio of red to green determined changes in the mitochondrial membrane integrity, with decreased ratios indicating mitochondrial damage (12).

2.2.13 Statistical Analysis

All results are reported as mean ± standard deviation; n represents the sample size. For the experimental analysis, statistical significance was determined using a two-tailed Student's t-test with $\alpha = 0.05$. Unequal variance was assumed. The Bonferroni correction was applied to adjust for testing multiple hypotheses.

2.3 Results

2.3.1 Dimensionality Reduction and Clustering

The timeline for conducting RNA-seq analysis on different cell types is shown in **Figure 2.1B**. We performed hierarchical clustering (**Figure 2.2A**) and dimensionality reduction (**Figure 2.2B** and **Figure 2.2C**) on the RNA-seq data (**Section 2.2**). We found that the samples first clustered by

cell type and subsequently, within each cell type, by timepoint (**Figure 2.2A**). These results indicate that there is a measurable difference in gene expression between both cell types at these time points. PCA and t-SNE analysis visually corroborated this clustering (**Figure 2.2B** and **Figure 2.2C**). The first principal component (PC1) accounts for 89% variance and the second component (PC2) accounts for 8% in the data. PHH samples were substantially separated from iHLC samples along PC1, suggesting that this component correlated with cell type. On the other hand, PHH samples on Day 6 were separated from Day 9 samples along PC2, as were iHLC samples on Days 0 and 9, indicating that this component may correspond to the timepoint. Similarly, in the t-SNE plot, biological replicates at each time point were clustered together within these groups and were distinctly separate from samples for other days and cell types.

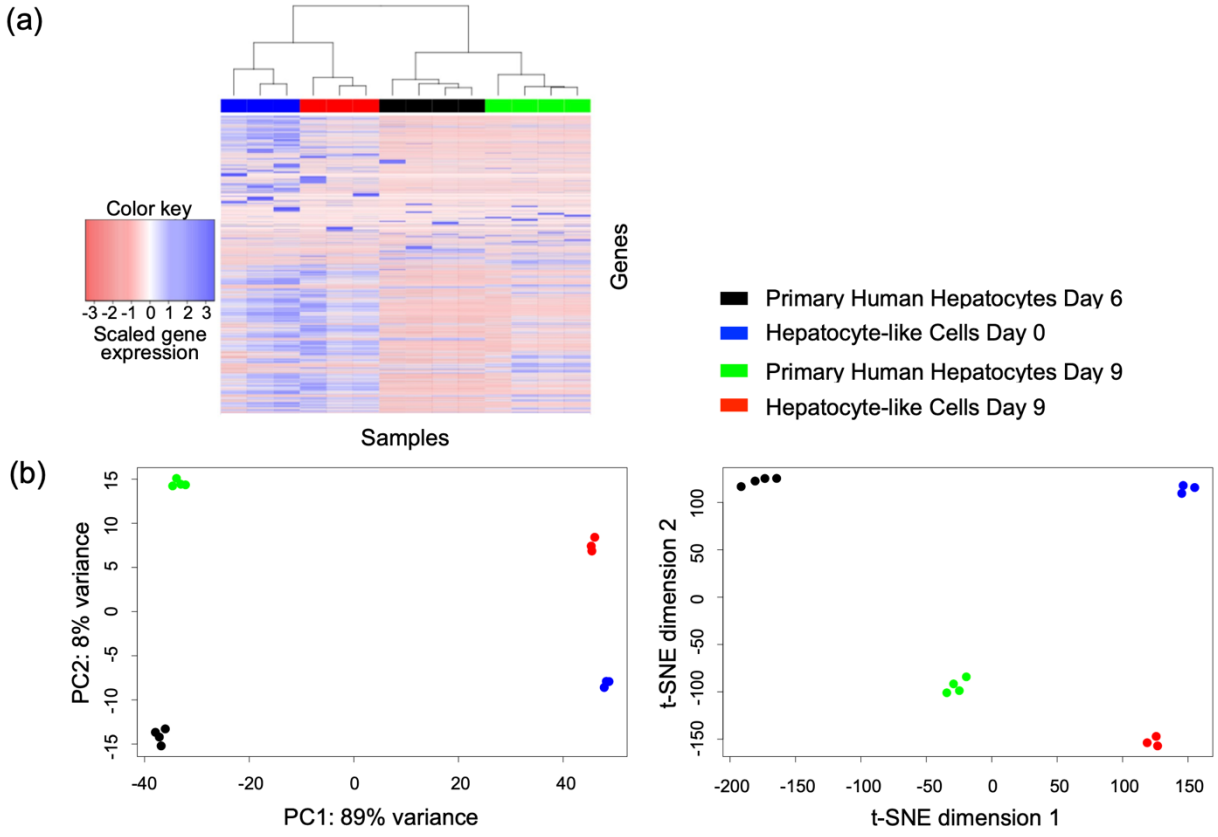

Figure 2.2 (**A**) Hierarchical clustering of PHH and iHLC gene expression data. (**B**) PCA and (**C**) t-SNE dimensionality reduction.

2.3.2 Differential Gene Expression Analysis and Functional Enrichment

Encouraged by this result, we computed the genes that were overexpressed in PHHs compared to iHLCs on Day 9 (**Section 2.2**). For this comparison, there were a total of 9504 differentially expressed genes. Functional enrichment analysis in this set of genes (**Section 2.2**) identified 51 pathways (only 30 are shown) (**Figure 2.3**) overrepresented in PHH samples with a *p*-value below 0.05 ($p < 0.05$). We further investigated several of these enriched pathways and processes related to hepatic functions.

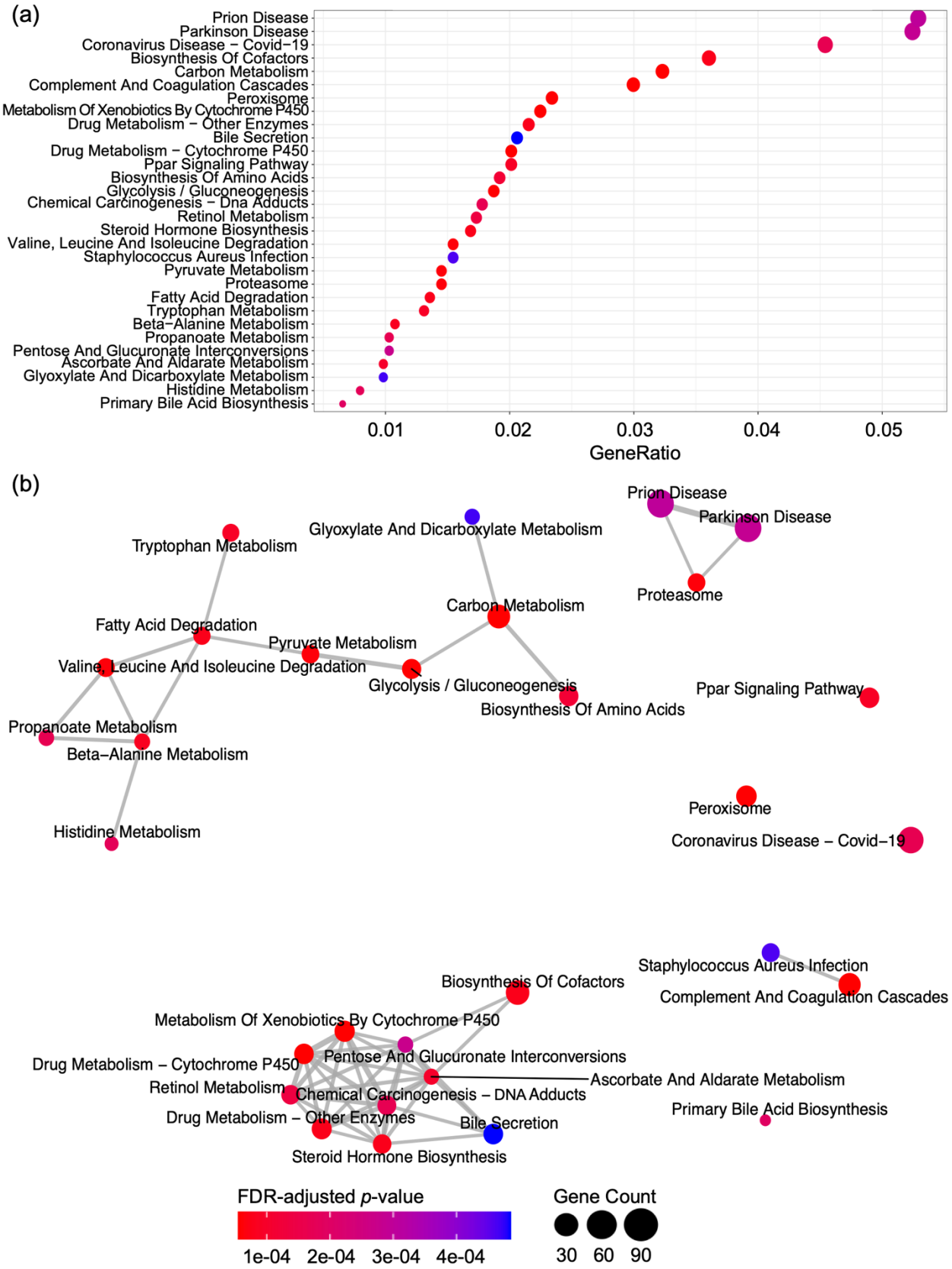
(a)
Prion Disease
Parkinson Disease
Coronavirus Disease − Covid−19
Biosynthesis Of Cofactors
Carbon Metabolism
Complement And Coagulation Cascades
Peroxisome
Metabolism Of Xenobiotics By Cytochrome P450
Drug Metabolism − Other Enzymes
Bile Secretion
Drug Metabolism − Cytochrome P450
Ppar Signaling Pathway
Biosynthesis Of Amino Acids
Glycolysis / Gluconeogenesis
Chemical Carcinogenesis − Dna Adducts
Retinol Metabolism
Steroid Hormone Biosynthesis
Valine, Leucine And Isoleucine Degradation
Staphylococcus Aureus Infection
Pyruvate Metabolism
Proteasome
Fatty Acid Degradation
Tryptophan Metabolism
Beta−Alanine Metabolism
Propanoate Metabolism
Pentose And Glucuronate Interconversions
Ascorbate And Aldarate Metabolism
Glyoxylate And Dicarboxylate Metabolism
Histidine Metabolism
Primary Bile Acid Biosynthesis
0.01
0.02
0.03
0.04
0.05
GeneRatio
(b)
Prion Disease
Parkinson Disease
Glyoxylate And Dicarboxylate Metabolism
Tryptophan Metabolism
Proteasome
Carbon Metabolism
Fatty Acid Degradation
Pyruvate Metabolism
Valine, Leucine And Isoleucine Degradation
Glycolysis / Gluconeogenesis
Ppar Signaling Pathway
Biosynthesis Of Amino Acids
Propanoate Metabolism
Beta−Alanine Metabolism
Peroxisome
Histidine Metabolism
Coronavirus Disease − Covid−19
Staphylococcus Aureus Infection
Biosynthesis Of Cofactors
Complement And Coagulation Cascades
Metabolism Of Xenobiotics By Cytochrome P450
Drug Metabolism − Cytochrome P450
Pentose And Glucuronate Interconversions
Ascorbate And Aldarate Metabolism
Retinol Metabolism
Chemical Carcinogenesis − DNA Adducts
Primary Bile Acid Biosynthesis
Drug Metabolism − Other Enzymes
Bile Secretion
Steroid Hormone Biosynthesis
FDR-adjusted p-value
1e-04
2e-04
3e-04
4e-04
Gene Count
30
60
90

Figure 2.3 (**A**), (**B**) KEGG pathways upregulated in PHHs compared to iHLCs on Day 9. (**A**) Each row represents a KEGG pathway. The x-axis corresponds to the fraction of genes in the pathway that are also differentially expressed. The legend for the color and size of the circles appears in the right of the panel. (**B**) Network of overlaps between enriched pathways. Each node is a pathway, and each edge connects pairs of pathways that overlap in differentially expressed genes. Node color indicates the FDR-corrected p-value of enrichment for the corresponding pathways while node size reflects the number of genes in the pathway.

2.3.3 Bile Secretion

Genes involved in bile secretion were upregulated in PHHs compared to iHLCs on Day 9. Of the 80 genes in the bile secretion pathway, 44 were found to be upregulated in PHHs ($p < 0.05$). A major function of the liver is the production of bile acids and their transport through bile canaliculi (1). Cholesterol causes the synthesis of bile acids, which aid in the absorption and clearance of lipids and lipid-soluble vitamins and molecules (1, 120). Bile acids are transported and recycled through the liver. Inhibition of this pathway can lead to severe complications, such as gallstones and cholestasis (120).

UDP-glucuronosyltransferase (UGT) genes were upregulated in PHHs. Bile glucuronidation, conducted by UGT enzymes, is an important step in the conjugation of bilirubin to allow for the formation of water-soluble molecules (121). Of note, UGT1A1, the primary enzyme that glucuronates bilirubin to conjugated bilirubin, was elevated by 15-fold in PHHs (122). Aquaporin 9 (AQP9) was upregulated in PHHs by 455-fold. This gene corresponds to a channel on the basolateral membrane of hepatocytes, and facilitates transport of urea, water, glycerol, and bile (123, 124). ATP binding cassette coding genes (ABCB1, ABCG5, ABCC2, ABCB4, ABCG2, ABCC3) were significantly upregulated as well ($p < 0.05$). These ATP-dependent proteins transport molecules across the hepatocyte membrane and are involved in the metabolism of drugs and xenobiotics (125).

We focus on two major enzymes involved in the cholesterol metabolism cascade. CYP7A1, an enzyme found in the endoplasmic reticulum membrane, catalyzes the initial reaction in cholesterol metabolism to bile acids in hepatocytes (125). This is the rate-limiting step in the catabolic pathway (125). PHHs expressed 3.44-fold higher CYP7A1 compared to iHLCs. BAAT, bile acid-CoA amino acid N-acyltransferase, catalyzes the second step in bile-acid production from cholesterol (126). This gene was upregulated in PHHs by 3.3-fold. The upregulation of these enzymes suggests that the ability to metabolize cholesterol in iHLCs may be lower than in PHHs. The gene expression analysis was validated by immunofluorescence measurements which show that bile canaliculi were present only in PHHs (**Figure 2.4A** and **2.4B**). Bile canaliculi are responsible for transporting bile on the apical side of hepatocytes (1). ABCB4, ABCG5/8 and bile salt export protein (BSEP or ABCB11) are three key genes that regulate and are involved in the formation of bile and transport through the canaliculi of hepatocytes (127). BSEP is expressed in both cell types. However, there is no statistically significant difference in expression ($p > 0.05$). ABCB4 and ABCG5/8 are expressed 5.4-fold, 8.2-fold, and 5.4-fold higher in PHHs compared to iHLCs. Additionally, SLC51A, SLC10A1, and SLCO1B3, members of the solute carrier transporter family, import bile acids in hepatocytes (127). These three genes were upregulated in PHHs by 4.1-, 3.9-, and 41.4-fold higher in PHHs, respectively. The lower expression of these proteins could explain the lack of bile formation and, therefore, the absence of canaliculi in iHLCs (**Figure 2.4C)** (127).

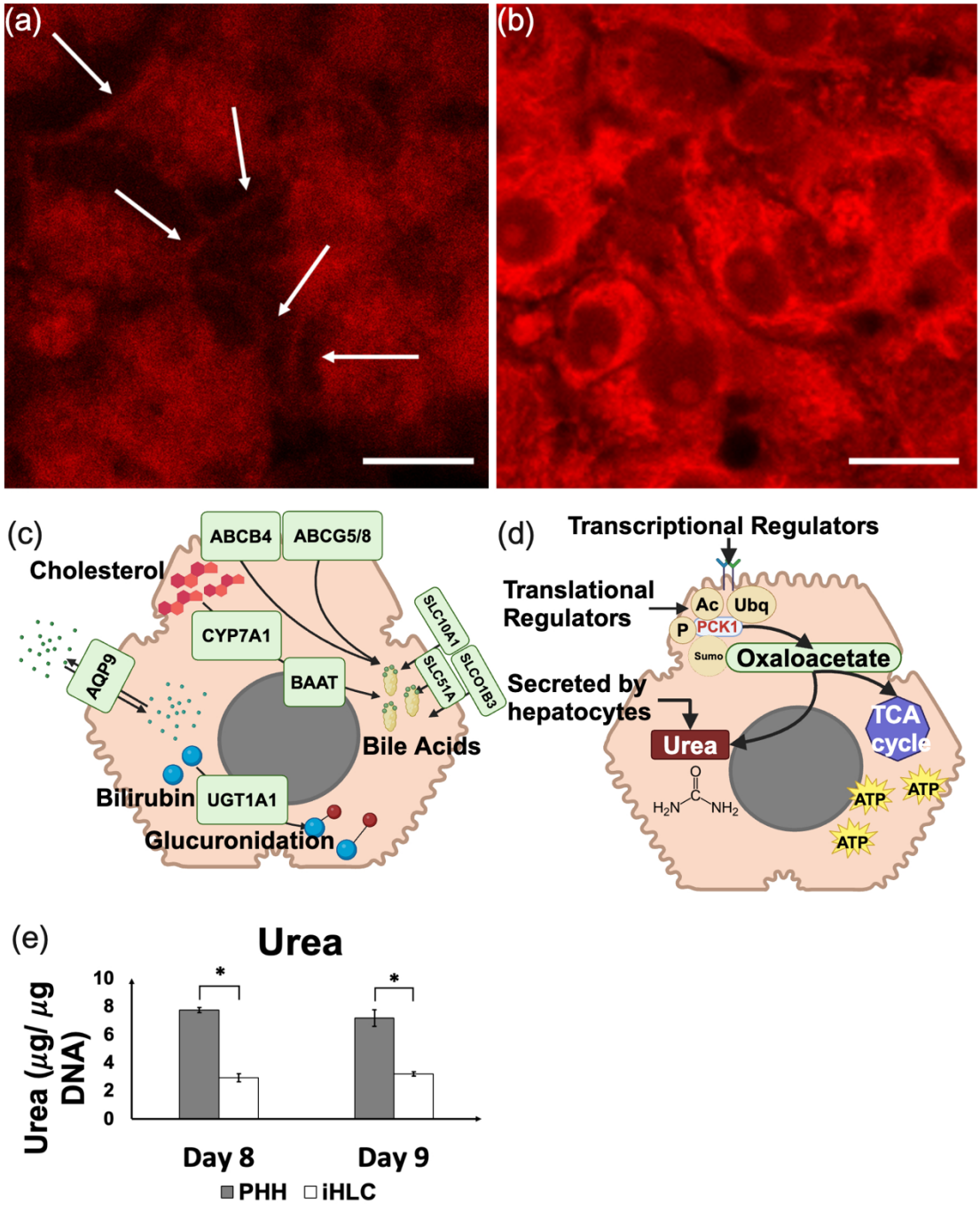

Figure 2.4 Immunostaining of bile canaliculi on Day 9 for (**A**) PHHs and (**B**) iHLCs. White arrows point to bile canaliculi. Scale bars = 50 μm. (**C**) Schematic of key proteins regulating bile secretion and bile canaliculi formation in hepatocytes. (**D**) Schematic of PCK1 regulating oxaloacetate which feeds into the TCA and urea cycles. (**E**) Urea secretion of PHHs and iHLCs at Day 8 and Day 9. *p < 0.05 relative to the iHLCs values at each respective time point, n ≥ 3.

2.3.4 TCA Cycle

The TCA cycle was upregulated in PHHs compared to iHLCs on Day 9 ($p < 0.05$). Of the 29 genes in this KEGG pathway, 19 genes were upregulated in PHHs. These genes corresponded to five out of the eight steps involved in the citric acid cycle (**Table 2.2**) (128).

Table 1.2 Upregulated genes corresponding to enzymes in TCA cycle in PHHs compared to iHLCs.

Enzyme Corresponding to Step in TCA Cycle	**Fold-Change in PHHs vs. iHLCs**
ACO1/ ACO2 (Aconitase)	1.990 / 1.891
IDH2/ IDH3G (Isocitrate Dehydrogenase)	1.542 / 4.968
SDHB (Succinyl-CoA Dehydrogenase)	1.536
FH (Fumarase)	2.073
MDH1/ MDH2 (Malate Dehydrogenase)	2.108 / 2.160

The most upregulated gene in the TCA cycle pathway was PCK1 (phosphoenolpyruvate carboxykinase 1), the primary regulator of gluconeogenesis (129). Gluconeogenesis can occur as a result of a low insulin-to-glucagon ratio and by downstream signaling through cAMP pathways to produce glucose (129). PCK1 was elevated by 87-fold in PHHs compared to iHLCs. This enzyme catalyzes the formation of phosphoenolpyruvate from oxaloacetate, derived from pyruvate (129, 130). This enzyme also promotes the TCA cycle by removing metabolic waste and contributing to pyruvate cycling, or the production of pyruvate to make ATP for the cell by initiating the citric acid cycle when glucose is low (**Figure 2.4D**) (131, 132). PCK1 expression is regulated transcriptionally, post-transcriptionally, and post-translationally (133, 134). However, the most common mechanism is transcriptional regulation (133, 134). Although, acetylation, ubiquitination, SUMOylation, and phosphorylation may also regulate the activity of PCK1 (133, 134). The translational regulation of rate-limiting enzymes, such as PCK1, may contribute to the differences exhibited in the gene expression and urea secretion in iHLCs compared to PHHs.

Additionally, OGDHL, or oxoglutarate dehydrogenase L, was upregulated in PHHs by 63.5-fold. OGDHL also downregulates protein kinase B (AKT) signaling cascades (135). AKT signaling can

be coupled with phosphoinositide 3-kinase (PI3K) and the mammalian target of rapamycin (mTOR), which is involved in cell proliferation, migration and protein and glucose metabolism (135). The PI3K/ AKT/ mTOR pathway is also involved in regulating glucose levels (135).

The transamination of oxaloacetate produces aspartate which reacts with citrulline which feeds into the urea cycle (136). We evaluated urea secretion as a metric for PHH and iHLC function (15, 106). The experimental results show normalized urea secretion in PHHs is 2 to 2.5-fold higher than in iHLCs on Days 8 and 9 in culture ($p < 0.05$, **Figure 2.4E**).

2.3.5 Hepatic Biotransformation

The CYP450 family of enzymes are primarily responsible for biotransformation, an important liver function that involves the metabolism of harmful toxicants and xenobiotics that enter the body (1, 11). Although several CYP450 enzymes are present in the liver, CYP3A4, CYP2C9, CYP2C19, CYP2D6, CYP1A2, and CYP2E1 are responsible for the majority of drug and toxicant metabolism (11, 137). Genetic polymorphisms in these enzymes are responsible for the variability to drug response between individuals (138). The UGT enzymes are also responsible for drug as well as bilirubin metabolism and hormone degradation (139). Polymorphisms in these enzymes can also contribute to adverse reactions to several non-polar, lipophilic drugs (139, 140).

Three KEGG pathways related to biotransformation were upregulated in PHHs compared to iHLCs on Day 9 (**Table 2.3**). Since the pathways had upregulated genes in common with each other, we discuss the differential gene expression of enzymes responsible for drug metabolism from all three pathways, with a focus on CYP450 and UGT enzyme families.

Table 2.3 KEGG pathways involved in drug metabolism upregulated in PHHs compared to iHLCs at Day 9.

KEGG Pathway	**Upregulated Genes/ Total Genes in Pathway**	***p*-value**
Metabolism of Xenobiotics by CYP450	48/ 66	4.61×10^{-9}

Drug Metabolism – CYP450	43/ 61	1.81×10^{-7}
Drug Metabolism – Other Enzymes	46/76	2.18×10^{-5}

2.3.5.1 CYP450 Enzymes

CYP450 enzymes are heme-containing proteins that catalyze the metabolism of various xenobiotics, drugs, carcinogens, steroids, eicosanoids, and vitamins (1, 138). The metabolism of these compounds by CYP450 enzymes can result in reactive metabolites which can cause liver injury (1, 12, 137, 138). The fold changes in gene expression between PHHs and iHLCs of CYP enzymes involved in the three KEGG pathways are presented in **Table 2.4**. CYP1A2 is one isoform of the CYP1 family, which also includes CYP1A1 and CYP1B1 (141). CYP1A2 metabolizes drugs, such as clozapine, used in the treatment of neurological conditions (141). The gene expression level of CYP1A2 was 8254-fold higher in PHHs compared to iHLCs. While the expression of 11 CYP enzymes was upregulated, we focused our investigation on two toxicants metabolized by CYP2E1. We specifically investigated CYP2E1 because it is the primary enzyme involved in the metabolism of APAP and EtOH, two common toxicants that can lead to significant liver damage, and is shown to be upregulated 21810-fold in PHHs compared to iHLCs at Day 9 (7, 12, 142, 143). APAP is one of the leading causes of acute liver failure in the U.S. and ethanol can lead to a variety of liver diseases, including alcoholic fatty liver disease, fibrosis, and death (7, 142).

Table 2.4 CYP450 enzymes upregulated in the KEGG drug metabolism pathways and the fold changes in PHHs compared to iHLCs.

CYP450 Enzyme	**Fold Change in PHHs Compared to iHLCs**
CYP2C9	36.362
CYP2E1	21810.944
CYP1A2	8254.906
CYP2A6	39409.052
CYP2B6	18165.926
CYP1A1	7.648
CYP2A7	1811.516
CYP2D6	494.059
CYP2S1	10.086

CYP2A13	36.722
CYP1B1	3.831

The activity of CYP enzymes, such as CYP2E1, can result in the production of reactive oxygen species (ROS) (144). Although ROS are produced by several reactions in the body, the build-up of these molecules can cause severe damage to cells by denaturing proteins, damaging RNA, DNA, and deactivating enzymes (137, 145). Therefore, antioxidants such as GSH prevent damage caused by ROS through enzymatic and non-enzymatic mechanisms (137). Generally, there is a balance between free radicals and neutralizing molecules. When disrupted, an increase of ROS causes a depletion of GSH, which leads to oxidant stress and cellular damage (12). Mitochondria, peroxisomes, and smooth endoplasmic reticulum (ER) are the three organelles in hepatocytes that produce the most ROS (137). CYP2E1 is primarily located in the ER and mitochondria of hepatocytes (146). The production of ROS affects the mitochondrial respiratory chain, which aids in the production of cellular ATP (145). These free radicals directly damage the complexes involved in the electron-transport chain in addition to proteins, lipids, and DNA (145). This cascading effect can lead to the damage of mitochondria by decreased transcription and translation of mitochondrial proteins, increased permeability of the organelle membrane, and the release of cytochrome C and apoptosis (145) (**Figure 2.5A).**

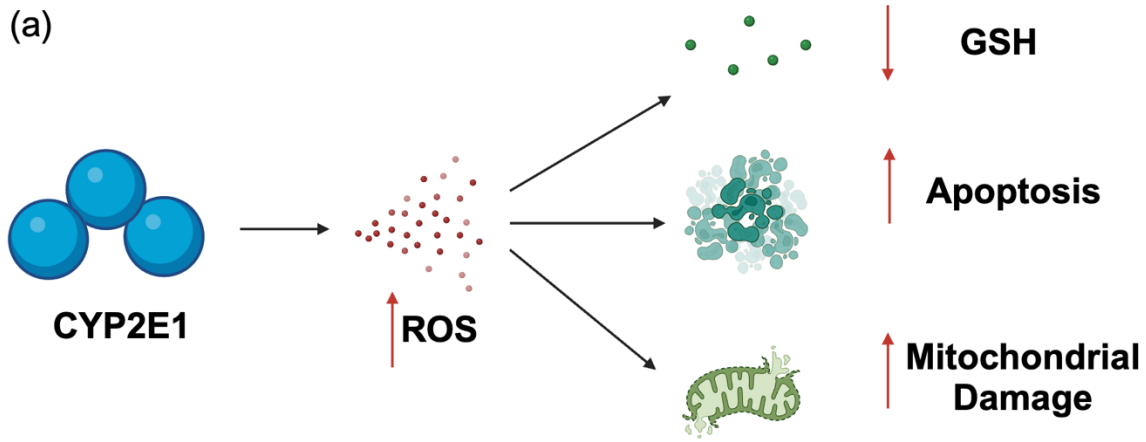
(a)
GSH
Apoptosis
CYP2E1
ROS
Mitochondrial Damage

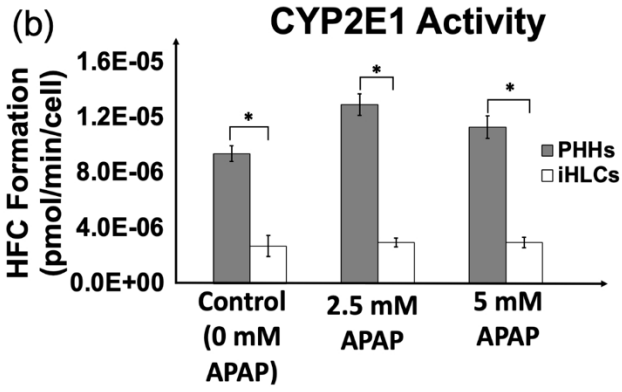
(b)
CYP2E1 Activity
HFC Formation (pmol/min/cell)
1.6E-05
1.2E-05
8.0E-06
4.0E-06
0.0E+00
PHHs
iHLCs
Control (0 mM APAP)
2.5 mM APAP
5 mM APAP

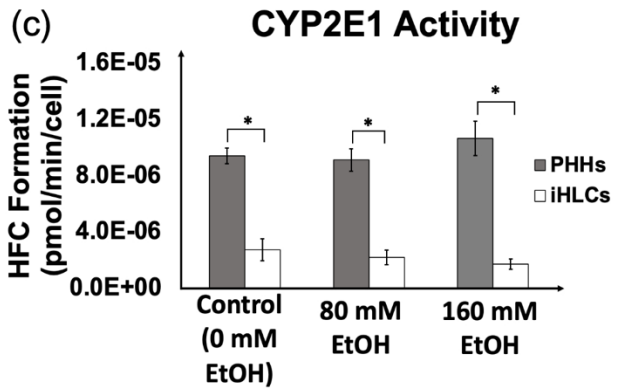
(c)
CYP2E1 Activity
HFC Formation (pmol/min/cell)
1.6E-05
1.2E-05
8.0E-06
4.0E-06
0.0E+00
PHHs
iHLCs
Control (0 mM EtOH)
80 mM EtOH
160 mM EtOH

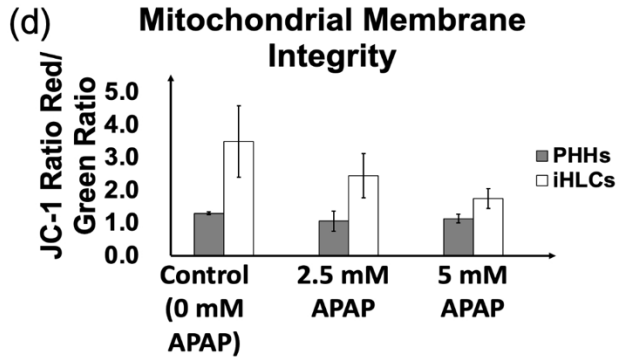
(d)
Mitochondrial Membrane Integrity
JC-1 Ratio Red/ Green Ratio
5.0
4.0
3.0
2.0
1.0
0.0
PHHs
iHLCs
Control (0 mM APAP)
2.5 mM APAP
5 mM APAP

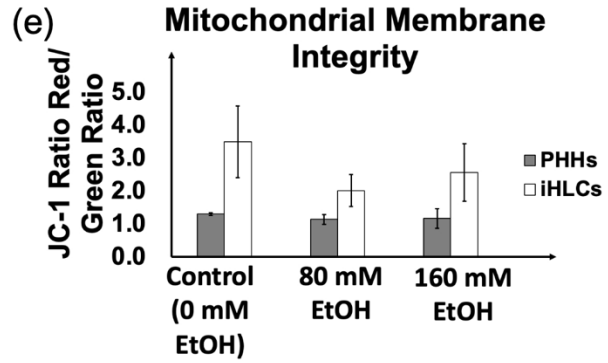
(e)
Mitochondrial Membrane Integrity
JC-1 Ratio Red/ Green Ratio
5.0
4.0
3.0
2.0
1.0
0.0
PHHs
iHLCs
Control (0 mM EtOH)
80 mM EtOH
160 mM EtOH

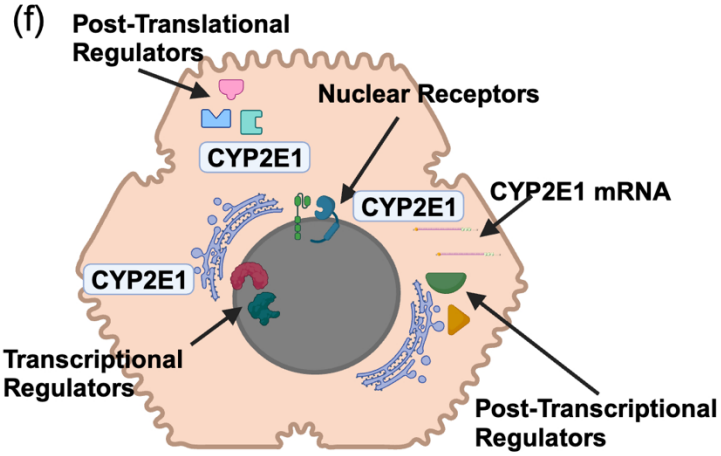
(f)
Post-Translational Regulators
Nuclear Receptors
CYP2E1
CYP2E1
CYP2E1 mRNA
CYP2E1
Transcriptional Regulators
Post-Transcriptional Regulators

Figure 2.5 (**A**) When ethanol and acetaminophen are administered to hepatocytes, CYP2E1-mediated biotransformation can result in an increase in ROS, which then causes a depletion of GSH and increases in apoptosis and mitochondrial membrane damage. After APAP and EtOH administration to iHLCs and PHHs on Day 8. Data is shown for Day 9. (**B**) CYP2E1 activity measured by HFC formation after APAP administration; (**C**) CYP2E1 activity measured by HFC formation after EtOH administration; (**D**) Red/ Green JC-1 ratio after APAP administration; (**E**) Red/ Green JC-1 ratio after EtOH administration. *$p < 0.05$ relative to the iHLC values for each respective culture model, $n \geq 3$. (**F**) Schematic of different regulators of CYP2E1 enzymes in hepatocytes.

To further evaluate CYP2E1 activity in PHHs and iHLCs, we measured the formation of HFC when APAP and EtOH were administered to cultures (12, 119). Two concentrations of APAP, 2.5 mM (LC_{50} for humans) and 5 mM (2 X LC_{50}), and EtOH, 80 mM (1/2 LC_{50}) and 160 mM (LC_{50}), were administered. For each of the concentrations, there was a statistically significant difference ($p < 0.05$) in CYP2E1 activity in PHHs compared to iHLCs. The baseline CYP2E1 activity in PHHs was $1.16 \times 10^{-5} \pm 0.321 \times 10^{-5}$ pmol/ min/ cell compared to $0.317 \times 10^{-5} \pm 0.00827 \times 10^{-5}$ in iHLCs, representing an approximate 3.7-fold change (**Figures 2.5B** and **2.5C)**. CYP2E1 activity in PHHs was 4.30-fold and 3.79-fold higher than in iHLCs at 2.5 and 5 mM APAP, respectively. Similarly, after ethanol administration, CYP2E1 activity for PHHs was 4.12-fold and 6.20-fold higher than in iHLCs for EtOH concentrations of 80 and 160 mM, respectively.

Regulation of CYP2E1 occurs through transcriptional, post-transcriptional, translational, and post-translation mechanisms (**Figure 2.5F**). However, activity of this enzyme most commonly occurs due to post-transcriptional events (147). For example, a study by Kocarek et. al. indicated that the CYP2E1 mRNA has high turnover and is not immediately degraded upon translation (147, 148). The turnover is translation-dependent, indicating that the same mRNA strand may yield high quantities of the protein (147, 148). The structure of the CYP2E1 mRNA can also affect protein synthesis (147, 148). Proteinases that modify mRNA and deplete the 5' UTR end resulted in increased CYP2E1 expression (147, 148). The poly(A) tail of the CYP2E1 mRNA and sequences in the 3' UTR sequence protect from RNase activity and degradation (147, 148). These

mechanisms may explain the drastic differences observed between the activity and fold-change of CYP2E1 in iHLCs and PHHs (12, 147, 148).

Mitochondrial membrane integrity was also studied to understand the effects of CYP2E1 metabolism (**Figures 2.5D** and **2.5E)** for cultures treated with APAP and EtOH (12, 149). A decrease in the JC-1 ratio is an indication of increased mitochondrial membrane damage (12). For both toxicants, the ratio was decreased in iHLCs compared to PHHs; however, the difference was not statistically significant ($p < 0.05$). We also measured GSH fold changes in APAP and EtOH treated samples, however, changes in GSH were statistically insignificant. The RNA-seq analysis concluded that the GSTT1 gene, a glutathione transferase enzyme, had a 19860-fold change in PHHs compared to iHLCs. More investigation on glutathione depletion due to biotransformation in each cell type is needed.

2.3.5.2 UDP-Glucuronosyltransferase Enzymes

UGT enzymes are involved in the metabolism of bilirubin, hormones, and vitamins (139, 150). Here, we report their upregulation in PHHs compared to iHLCs with respect to the drug metabolism pathways. UGT enzymes are involved in conjugation reactions in biotransformation of toxicants and xenobiotics (150). Glucuronidation reactions occur because of UGT enzymes, where glucuronic acid is covalently linked to a substrate, which neutralizes metabolic activity and aids in elimination (150). UGT1A10 is the most upregulated UGT enzyme in the pathways with a 2618.5-fold change in PHHs compared to iHLCs. UGT2B17 was differentially expressed with a 679-fold change. More investigation of glucuronidation reactions in iHLC drug metabolism is needed. Additionally, the versatility of these enzymes warrants further investigation on their involvement in multiple pathways (150).

2.3.6 Actin Organization

Hepatocytes require organized actin filaments to self-assemble (151). The actin cytoskeleton is usually confined to the peripheral regions in PHHs (**Figure 2.6A**) (14). However, the actin cytoskeleton in iHLCs was observed throughout the cross-section of the cell (**Figure 2.6B**). The dedifferentiation of hepatocytes can result in the organization of actin stress fibers that span the entire cell (14, 152). PHHs have a 1.32-fold difference in the ACTB, the actin gene, compared to iHLCs, which could explain the difference in the actin cytoskeleton.

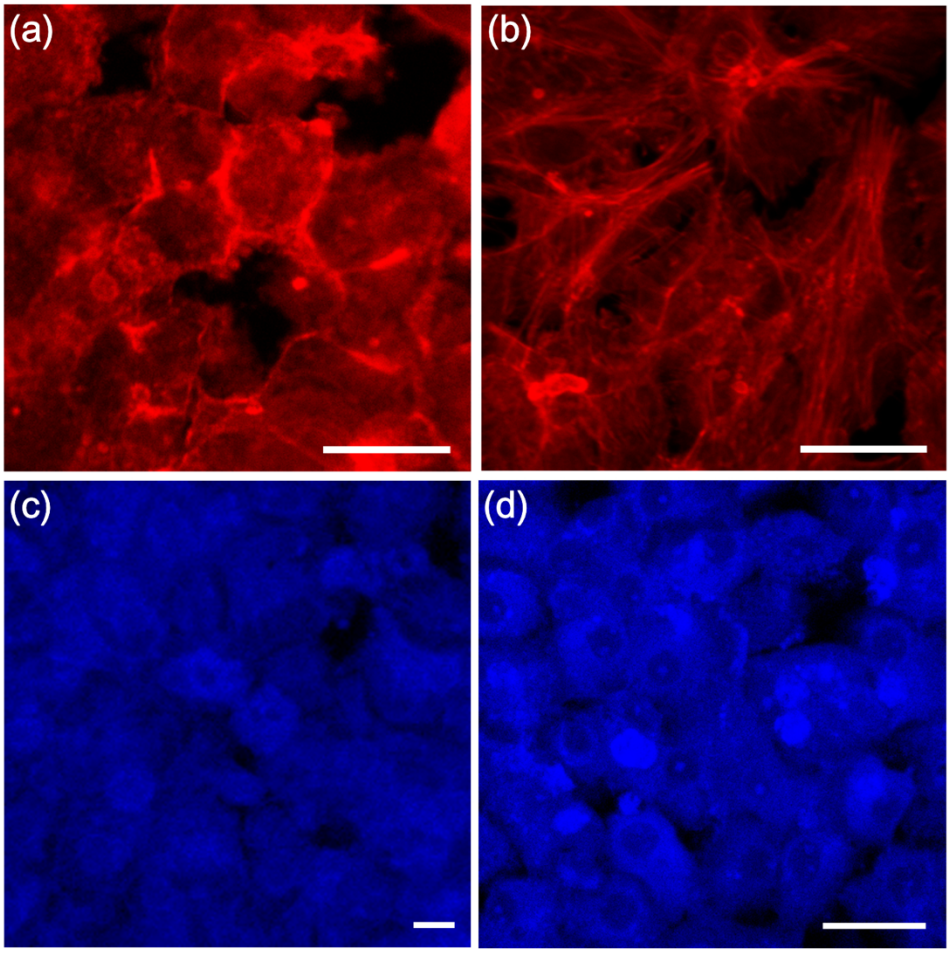

Figure 2.6 Immunostaining of the actin cytoskeleton in (**A**) PHHs and (**B**) iHLCs on Day 9. Immunostaining for albumin in (**C**) PHHs and (**D**) iHLCs on Day 9. Scale bars = 50 μm.

2.3.7 Intracellular Albumin Expression

Albumin is used as a marker for hepatic maturation, specifically in studies on the differentiation of iHLCs (11, 45). Based on immunofluorescence images, the expression of intracellular albumin appears to be similar between iHLCs and PHHs (**Figures 2.6C** and **2.6D)**. The albumin gene, ALB, is not differentially expressed between these cell types, which could explain the experimental results.

2.3.8 Developmental Pathways and Transcriptional Regulators in iHLCs

The phenotypic and transcriptomic analyses in the present study indicate that iHLCs have lower liver-related functions compared to PHHs. We sought to determine if any developmental pathways were upregulated in iHLCs compared to PHHs on Day 9. Functional enrichment analysis did not reveal any such pathways in the KEGG database. However, the Wnt signaling pathway in the GO database was significantly upregulated at this time point ($p < 0.05$) in iHLCs (**Figure 2.7**). The activation of this pathway is key in differentiating iPSCs to the definitive endoderm, leading cells towards the hepatic lineage (45, 53, 67, 76, 98). Additionally, the Wnt pathway is activated during embryogenesis and regulates hepatobiliary development as well as adult liver regeneration (153). This pathway is active when hepatocytes are not maintaining hepatic homeostasis or when they may require additional maturation (153).

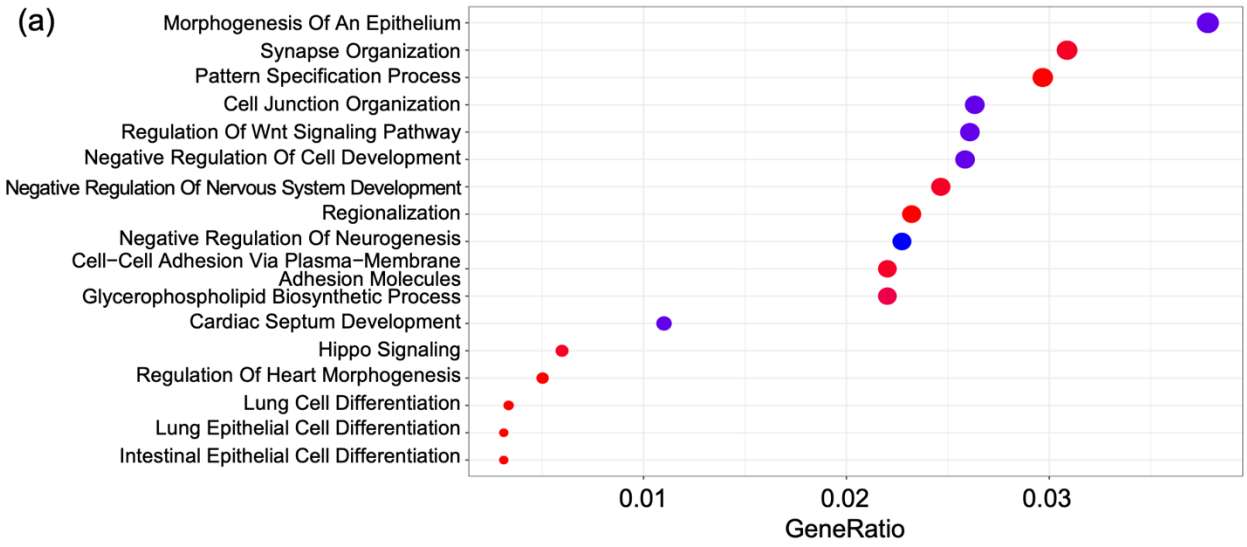
(a)
Morphogenesis Of An Epithelium
Synapse Organization
Pattern Specification Process
Cell Junction Organization
Regulation Of Wnt Signaling Pathway
Negative Regulation Of Cell Development
Negative Regulation Of Nervous System Development
Regionalization
Negative Regulation Of Neurogenesis
Cell−Cell Adhesion Via Plasma−Membrane Adhesion Molecules
Glycerophospholipid Biosynthetic Process
Cardiac Septum Development
Hippo Signaling
Regulation Of Heart Morphogenesis
Lung Cell Differentiation
Lung Epithelial Cell Differentiation
Intestinal Epithelial Cell Differentiation
0.01
0.02
0.03
GeneRatio

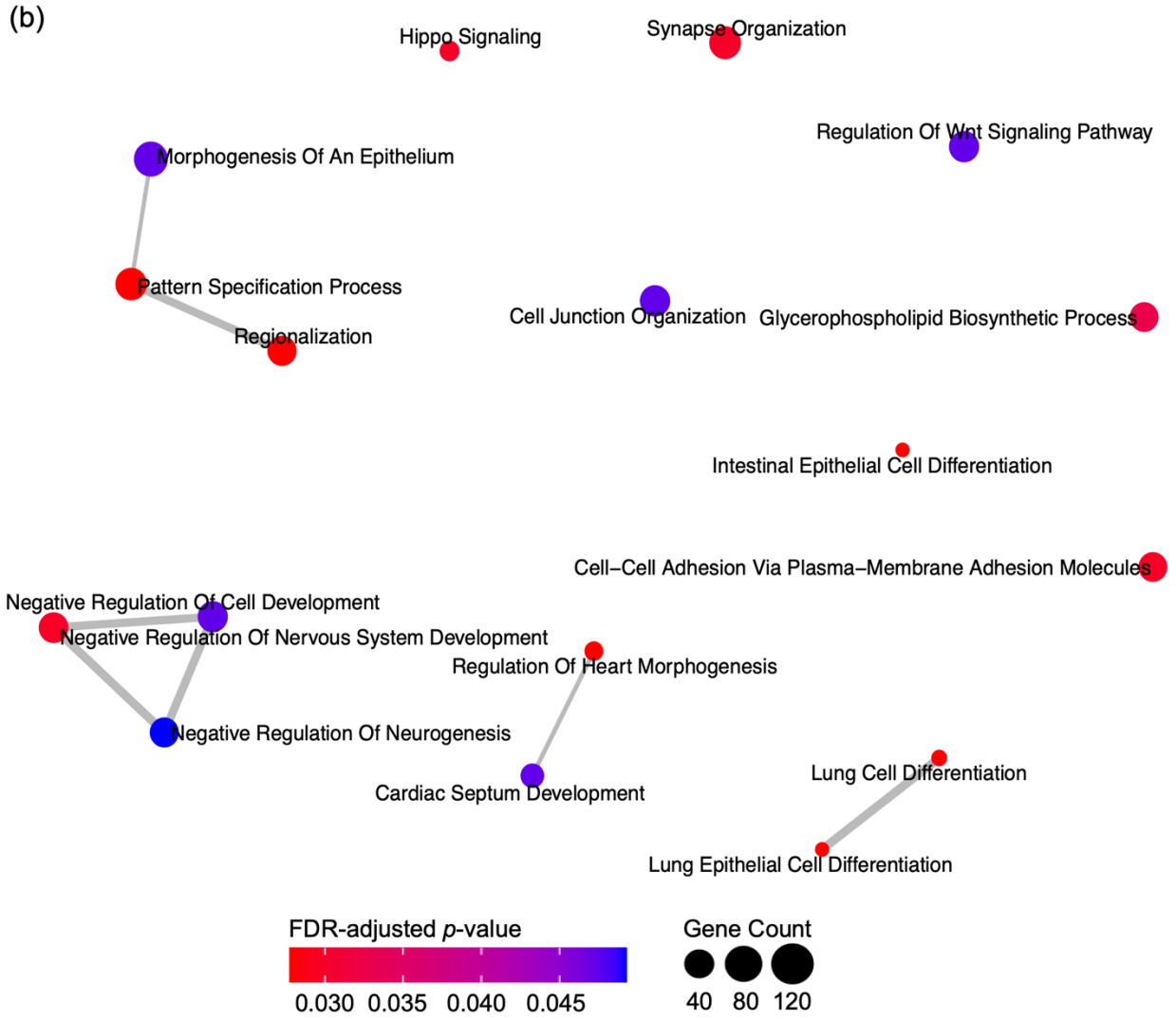
(b)
Hippo Signaling
Synapse Organization
Regulation Of Wnt Signaling Pathway
Morphogenesis Of An Epithelium
Pattern Specification Process
Regionalization
Cell Junction Organization
Glycerophospholipid Biosynthetic Process
Intestinal Epithelial Cell Differentiation
Cell−Cell Adhesion Via Plasma−Membrane Adhesion Molecules
Negative Regulation Of Cell Development
Negative Regulation Of Nervous System Development
Regulation Of Heart Morphogenesis
Negative Regulation Of Neurogenesis
Cardiac Septum Development
Lung Cell Differentiation
Lung Epithelial Cell Differentiation
FDR-adjusted p-value
0.030 0.035 0.040 0.045
Gene Count
40 80 120

Figure 2.7 (**A**), (**B**) GO pathways upregulated in iHLCs compared to PHHs on Day 9. (**A**) Each row represents a GO pathway. The x-axis corresponds to the fraction of genes in the pathway that are also differentially expressed. The legend for the color and size of the circles appears in the right of the panel. (**B**) Network of overlaps between enriched pathways. Each node is a pathway, and each edge connects pairs of pathways that overlap in differentially expressed genes. Node color indicates the FDR-corrected p-value of enrichment for the corresponding pathways while node size reflects the number of genes in the pathway.

Additionally, transcription factors including FOXA3, ATF5, CEBPA, FOXA1, GATA4, and GATA6 were significantly downregulated ($p < 0.05$) between iHLCs and PHHs. These transcription factors are reported to be highly expressed during liver embryogenesis and regeneration (54, 89, 92). These transcription factors further differentiate hepatoblasts to mature hepatocytes (54, 89, 92). In maturation protocols, such transcription factors have been added to iHLCs by lentivirus plasmid infection to further induce hepatic lineage (54, 89, 92). However, studies vary between which factors effectively lead to maturation, since some combinations have resulted in varying phenotypes, rather than a homogenous iHLC population (54, 87, 89, 92).

2.4 Discussion

While iHLCs have potential for future *in vitro* liver studies, it is known that they do not exhibit the same levels of hepatic functionality as PHHs (11, 104). In particular, the differences in their transcriptional programs have not been studied in detail. In this study, we present an RNA-seq analysis comparing PHHs and iHLCs on Day 9. Hierarchical clustering, PCA, and t-SNE visualizations of the gene expression profiles showed clear separation between these cell types, indicating that their transcriptional programs may be considerably dissimilar. We used unbiased computational analysis to find specific pathways that are differentially expressed between the two cell types. We reported pathways that impact key functions of hepatocytes, including bile secretion, the citric acid cycle, and biotransformation pathways. The transcriptomic results were validated by cellular analysis, which provides additional unique insights to understanding the

differences between iHLCs and PHHs. This study has reported that iHLCs require additional maturation before they can be used instead of PHHs. We have identified several genes that are downregulated in iHLCs in comparison to PHHs that may have contributed to the lower liver functions exhibited. Additional maturation protocols may need to be utilized with iHLCs in order for them to exhibit the same levels of hepatic functions as PHHs. A potential route to mature iHLCs could be the administration of growth factor cocktails to target the downregulated genes. For example, FGF-19 could be added to cultures to target the farnesoid X receptor (FXR) receptor that leads to bile canaliculi formation (154). Oncostatin M and dexamethasone may also be added to increase CYP enzyme expression (54, 155, 156).

Since bile canaliculi are only present in PHHs but not iHLCs, the absence could be explained by the lower expression of key enzymes in the bile formation, glucuronidation and cholesterol metabolism cascades. RNA-seq analyses from polarized iHLCs on Transwell® filters report the upregulation of the FXR/ retinoid X receptor pathways, involved in bile acid metabolism, compared to non-polarized iHLCs (157). Bile acids are typically secreted from the apical membrane of hepatocytes (157). Other studies have also shown that polarized iHLCs can lead to more bile functions (70, 158).

The lower expression of enzymes in the TCA cycle could explain the differences observed in urea secretion between the two cell types. With less enzymatic activity in the TCA cycle, a lack of buildup of oxaloacetate could yield lower transamination to aspartate, which feeds into the urea cycle. The lower expression of OGDHL downregulates the PI3K/ AKT/ mTOR pathway, which is involved in maintaining glucose metabolism (135). Acetyl-CoA is derived from pyruvate, the final product of the glycolysis pathway, and is a regulator of both the TCA and urea cycle (136, 159). Acetyl-CoA is also a regulator for carbamoyl phosphate synthetase 1, the enzyme that catalyzes the first step in urea production (159). Without acetyl-CoA production, the urea cycle would be

halted as a result of lack of enzymatic regulation (160). Therefore, the lower gene expression of these enzymes could explain why the urea secretion in iHLCs was lower compared to PHHs.

It has been well-established that iHLCs do not have the same CYP activity as PHHs (56, 79). There was a 3.8–39409-fold change in CYPs that were upregulated in the three biotransformation pathways investigated (**Table 2.4**). Interestingly, in our analysis, CYP3A4 was not upregulated in PHHs compared to iHLCs. CYP3A4 is the most abundant enzyme in the liver, metabolizing antidepressants, antibiotics, steroids, and anti-HIV agents (104, 161). In the future, we will conduct cellular measurements to determine if these trends hold.

We focused our analysis on CYP2E1, which was upregulated in PHHs by a factor of 2.18×10^4 compared to iHLCs. CYP2E1 has been implicated in APAP and EtOH metabolism, which have been widely studied in *in vitro* liver models (7, 12, 162). Since CYP2E1 activity was decreased in iHLCs, the lack of enzyme activity may explain why there were no significant differences in the JC-1 ratio. The cascading effect from this enzyme leads to mitochondrial damage and depletion of glutathione caused by the production of ROS (162).

Gene expression of liver enzymes, specifically CYP450 enzymes, is idiosyncratic (163, 164). More than 2,000 single nucleotide polymorphisms (SNPs) have been identified within CYP450 enzymes which could contribute to vast differences in drug response and clearance amongst individuals (163, 164). For example, a SNP mutation in the CYP3A4 gene could result in reduced enzyme activity (165). It could be possible that variations in differentiation protocols contribute to differences in fold-changes of certain genes between studies. For example, Viiri et. al. reported significant differences in CYP1A1 expression in iHLCs derived from protocols that used two different chemical cocktails (104). Genetic reprogramming, another differentiation protocol, of iHLCs with FOXA2 and HNF4α resulted in unstable phenotypes (87). Additionally, the donor's

background can significantly impact gene expression and phenotypic data during experimentation, which is also a challenge when using PHHs for *in vitro* studies (21). iHLCs can be derived easily from the skin, allowing for multiple sustainable sources for potential patient-specific toxicity studies (27). However, the results from this study and others exhibit the significant differences in several genes, pathways, and functions between iHLCs and PHHs, indicating that these cells require significant maturation before their widespread use (56, 79, 104).

In the present study, only transcriptomic data conducted with bulk RNA-seq was examined. Although, other 'omic data may also be investigated. Viiri et. al. used GRO-Seq to investigate differences in nascent RNAs including long non-coding RNA, primary miRNAs, and transcription factor binding sites of all lncRNAs (104). The mRNA results from Virii et. al. and the present study show some overlap. For example, CYP2E1, CYP1A1, CYP1A2, CYP2C9, and CYP2A6 were significantly upregulated in PHHs in both studies (104). Additionally, we have identified 13 UGT enzymes that were upregulated in PHHs compared to iHLCs, which were also reported by Viiri et. al. (104). Since iHLCs can be derived by various methods and donors, additional 'omics analyses could provide a deeper understanding of the differences between the two cell types.

In addition to bulk RNA-seq methods, individual cell differences in the transcriptomic programs of iHLCs and PHHs have also been investigated using single cell RNA-sequencing (scRNA-seq), which can be used to understand heterogeneity of a population (84, 166-168). These studies differ in the ways they induce the differentiation of iPSCs or progenitor cells into iHLCs, whether they incorporate iHLCs into organoids or not, or in their source for PHHs. Nevertheless, they point to similar trends between iHLCs and PHHs, especially the fact that protocols to create iPSCs often yield cells with characteristics of fetal hepatocytes (84, 168-170).

One study compared scRNA-seq measurements of human liver organoids derived from storable foregut progenitors (themselves induced from iPSCs) and PHHs (84). The organoids included hepatocyte-like cells that were virtually identical to PHHs and non-parenchymal cells (84). However, half the cells were in a state similar to hepatoblasts (84). scRNA-seq allows computation and comparison of the differentiation and developmental trajectories of iHLCs from hepatoblasts (169). These analyses indicated that while on day 14, iHLCs aligned with hepatoblasts, their subsequent development diverged from that of hepatocytes (169). These differences corresponded to downregulation in iHLCs of genes involved in bile acid transport, lipid metabolism, and xenobiotic metabolism (169). Another study that characterized iHLCs and PHHs with scRNA-seq analyses found that populations of these cells formed distinct clusters in a PCA plot (168), similar to our finding for bulk RNA-seq data (**Figure 2.2B**). Furthermore, iHLCs showed expression of selected liver and intestinal genes within the same cells. In contrast, the expression of intestinal genes was not detectable in PHHs (168).

After 48–72 h in monolayer culture, PHHs also dedifferentiate and lose their key functions (15, 106). A CS assembly has helped PHHs remain stable for up to a two-week period (106, 171). However, homeostasis of hepatocytes is maintained by cell-cell signaling with other non-parenchymal cells (NPCs) of the liver (15, 152, 172). We have previously showed that PHHs, when co-cultured in a 3D model with other NPCs, including liver sinusoidal endothelial cells (LSECs) and Kupffer cells, exhibit enhanced functionality including urea and albumin secretion and CYP activity (7, 12, 15, 21, 106). Additionally, a culture with these three cell types can elicit a response to administered toxicants closer to what occurs *in vivo*, creating a platform for further toxicity measurements (7, 12).

Additionally, the maturation of iHLCs could lead to their use in liver models if these cells can exhibit hepatic functions comparable to PHHs. Co-culturing iHLCs with other cell types such as

LSECs, human umbilical vein endothelial cells, adipose-derived stem cells, and hepatic stellate cells, for longer periods of time in a 3D matrix have shown improved urea and albumin secretion, expression of hepatic markers, protein secretion, bile canaliculi formation, and CYP activity (54, 72, 75, 173, 174). However, many of these are spheroid cultures which do not emulate liver architecture (72, 75). These spheroids are also assembled with cellular ratios that do not match *in vivo* conditions but are optimized for *in vitro* culture instead (72, 173).

2.5 Conclusions

The RNA-seq conclusions from this analysis correspond with previous studies and experimental results. Our study gives insight into the genome-wide transcriptomic analysis and the specific fold-changes of genes in differentially regulated pathways between the two cell types. Our study encourages targets of potential pathways that could improve the functionality of iHLCs. There remains tremendous potential to investigate how culturing iHLCs with other NPCs in a 3D organoid that closely recapitulates both cellular composition and architecture found *in vivo* can enhance their maturation and hepatic functions

Chapter 3: Multi-Cellular Human Liver Organoids Enable Complete Maturation of Induced Pluripotent Hepatocyte-like Cells Through Purely Endogenous Signals

U.S. Patent No. 63/64,336. May 31, 2024

N. Gandhi and P. Rajagopalan, Multi-Cellular Human Liver Organoids Enable Complete Maturation of Induced Pluripotent Hepatocyte-like Cells Through Purely Endogenous Signals. Submitted for Publication.

3.1 Introduction

Primary human cells are critical for biomedical translational science; however, they are very difficult to obtain. The tissue engineering community needs a sustainable source of primary human cells which are usually obtained from biopsies or cadavers while exhibiting donor-to-donor variations (21). Induced pluripotent stem cell (iPSC)-derived hepatocyte like cells (iHLCs) are considered a potential replacement for primary human hepatocytes (PHHs) since they can be obtained non-invasively (11, 33). Although iHLCs have been used in disease modeling, drug development, and regenerative medicine (29), several drawbacks limit their potential as a replacement to PHHs (11, 33, 55).

First, many protocols that have been used to differentiate and mature iHLCs (45, 50, 54, 60, 63, 73, 82, 83, 87, 101, 175) rely on generating artificial conditions that deviate significantly from the *in vivo* hepatic environment. A common approach is the addition of chemical cocktails, including different growth factors and their agonists or chemical molecules (50, 60, 63, 101). In the body, growth factors are present in the pg-ng/mL range (176). However, many maturation protocols administer chemicals at concentrations up to 10^6-fold higher (50, 60, 63, 101), which could potentially oversaturate receptors and alter signaling pathways and gene expression. Second,

variations among publications in the temporal administration of chemical cocktails have led to a lack of a systematic, repeatable approach to mature and differentiate iHLCs *in vitro* (45, 50, 60, 63, 101). Other protocols include culturing the cells on polymeric scaffolds, co-culturing with hepatic and non-hepatic cells, 2D and spheroid cultures, and genetic reprogramming with the addition of various transcription factors (54, 73, 82, 83, 175). Third, despite the different methods developed to mature them, iHLCs continue to express fetal markers such as alphafetoprotein (AFP) and cytochrome P450 (CYP) 3A7 and even exhibit unstable phenotypes (45, 50, 54, 60, 63, 73, 82, 83, 87, 101, 175).

During liver organogenesis, intercellular signaling from neighboring endothelial, developing stellate, and hematopoietic cells can regulate and induce multiple pathways for hepatocyte progenitor cells to undergo differentiation and maturation (177, 178). Motivated by this observation, we developed a reproducible methodology that used purely endogenous signals to promote the maturation of IHLCs. Our goal was to remove the limitations of existing protocols, especially to avoid overwhelming the cells with chemicals to stimulate developmental and functional pathways. We designed a novel 3D multicellular organoid that closely mimicked the tissue microenvironment in the liver. These organoids contained iHLCs, liver sinusoidal endothelial cells (LSECs) and Kupffer cells (KCs) arranged in a stratified architecture that mimics the liver sinusoid *in vivo*. Our goal was to demonstrate that endogenously secreted molecules drive iHLCs to maturation via signaling between the three hepatic cells (**Figure 3.1A**).

We provide a comprehensive comparison between iHLC and PHH markers to demonstrate that iHLCs in multi-cellular organoids are virtually indistinguishable from PHHs. To investigate how endogenous intercellular signaling may drive iHLC maturation, we measured the secretion of critical drivers of maturation: hepatocyte growth factor (HGF), prostaglandin E2 (PGE2), and Oncostatin M (OSM) in the organoids. We show that the secretion of PGE2 may be the key

molecule to drive maturation. Since the continued expression of PGE2 may be harmful to liver cells, we also sought to elucidate how the temporal concentrations of this prostaglandin can be modulated by liver-specific proteins.

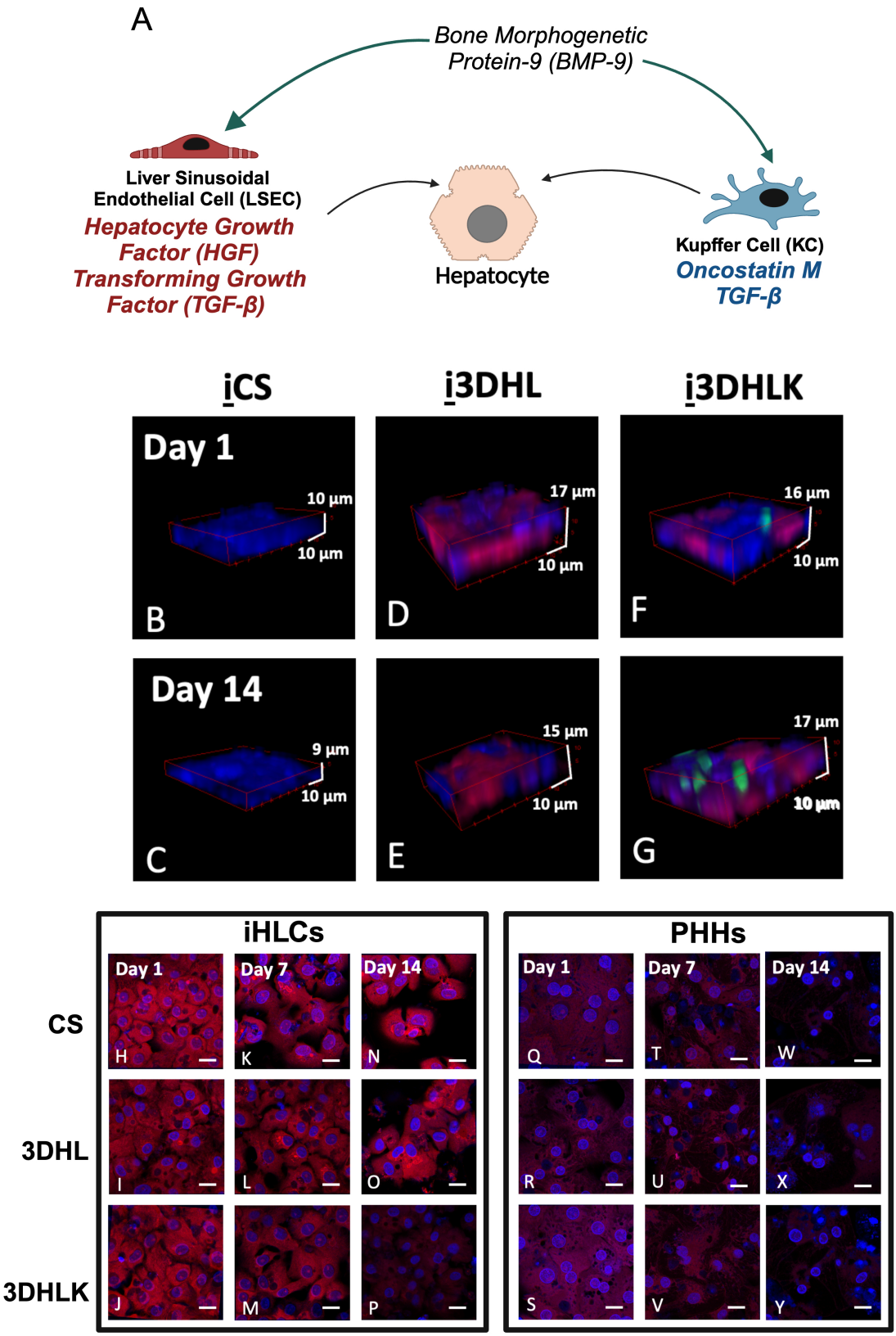
A
Bone Morphogenetic Protein-9 (BMP-9)
Liver Sinusoidal Endothelial Cell (LSEC)
Hepatocyte Growth Factor (HGF)
Transforming Growth Factor (TGF-β)
Hepatocyte
Kupffer Cell (KC)
Oncostatin M
TGF-β
iCS
i3DHL
i3DHLK
Day 1
10 µm
10 µm
B
17 µm
10 µm
D
16 µm
10 µm
F
Day 14
9 µm
10 µm
C
15 µm
10 µm
E
17 µm
10 µm
G
iHLCs
PHHs
CS
3DHL
3DHLK
Day 1
Day 7
Day 14
H
K
N
Q
T
W
I
L
O
R
U
X
J
M
P
S
V
Y

Figure 3.1 (**A**) Molecules secreted by LSECs and KCs that can signal maturation of hepatocytes during liver embryogenesis and development. 3D visual representations of iCS (**B**, **C**), i3DHL (**D**, **E**), and i3DHLK (**F**, **G**) cultures/ organoids on Days 1 and 14. iHLCs are immunostained for albumin (blue), LSECs for CD32b (red), and KCs for CD163 (green). Immunostaining for AFP (red) and nuclei (blue) for iHLC (**H-P**) and PHH (**Q-Y**) cultures on Days 1, 7 and 14. Scale bars = 20 μm. n = 3 biological replicates. Image analysis conducted on ≥12 images with ≥ 550 cells images for each culture.

We provide a comprehensive comparison between iHLC and PHH markers to underscore the need for a microenvironment with different liver cells that induces cellular maturation without the need for exogenous chemicals. To investigate how endogenous intercellular signaling may drive iHLC maturation, we measured the secretion of molecules such as hepatocyte growth factor (HGF), prostaglandin E2 (PGE2), and Oncostatin M (OSM) in the organoids. Our goal was to provide a mechanistic basis on how PGE2 may be the key molecule to drive maturation. Since the continued expression of PGE2 may be harmful to liver cells, we sought to elucidate how the secretion of this prostaglandin can be modulated by other proteins liver cells produce.

3.2 Methods

Phosphate buffered saline (PBS, 10 X), RPMI 1640, B-27, gentamicin, RIF, penicillin-streptomycin (Pen-Strep), sodium borohydride ($NaBH_4$), Triton-X, bovine serum albumin (BSA), GlutaMAX, goat serum, and horse serum were obtained from Thermofisher Scientific (Waltham, MA). Glutaraldehyde, human recombinant insulin, HEPES, APA) and EtOH were obtained from Sigma-Aldrich (St. Louis, MO). Dexamethasone was obtained from MP Biomedicals (Santa Ana, CA). Fibronectin was obtained from R&D Systems (Minneapolis, MN).

3.2.1 Culturing Hepatic Cells

All cells were maintained at 37℃ in a humidified environment at 5% CO_2. Spent culture medium was collected and stored at -80℃ until analyzed.

3.2.1.1 iHLCs: iHLCs (iCell Hepatocytes 2.0: Fujifilm (Santa Ana, CA) were seeded on collagen gels at 300,000 cells/ cm^2 according to the manufacturer's protocol (55) (**Section 3.6**). Culture media was changed every 24 h. iHLCs were cultured for 7 days prior to organoid assembly (55).

3.2.1.2 PHHs: PHHs (Sekisui Xenotech, Kansas City, KS) were seeded on collagen gels at 35,000 cells/ well in a 96-well plate (12) and cultured according to the manufacturer's protocol. Briefly, cells were thawed in OptiThaw, then seeded in OptiPlate, and maintained with media changes every 24 h thereafter with OptiCulture. Cells were cultured for 24 h prior to organoid assembly.

3.2.1.3 LSECs: LSECs (ScienCell, Carlsbad, CA) with a passage number ≤ 5 were maintained in the manufacturer's endothelial cell medium prior to organoid assembly (12). LSEC monocultures were seeded on collagen gels on the day of organoid assembly and maintained in iHLC media.

3.2.1.4 KCs: KCs (Thermofisher Scientific, Waltham, MA) or Novabiosis, Durham, NC) were thawed according to the manufacturer's protocol 24 h before organoid assembly (**Section 3.6**).

3.2.2 Organoid Assembly

LSECs and KCs were mixed in a 1.1 mg/ mL collagen Type 1 solution that contained fibronectin (1% v/v). Initial seeding ratios were 5:1 hepatocytes: LSECs and 10:1 hepatocytes: KCs, which is similar to cellular ratios *in vivo* (1). To assemble the collagen sandwich (CS) models, a second layer of collagen was added on top of the iHLCs or PHHs (**Figure 3.6A**). All organoids were maintained for up to 14 days. Cultures were ended on Days 1, 7, or 14 post-organoid assembly (**Figure 3.6B**).

3.2.3 Statistical Analysis

A two-tailed Student's t-test with α = 0.05 was used to determine statistical significance while assuming unequal variance. The Bonferroni correction (multiple hypothesis testing) was also applied. All data are reported as the mean $\pm$ standard deviation where *n* represents the sample size.

3.3 Results

When referring to the multicellular models, the notation will indicate the following. Hepatocytes, either iHLCs (**i**) or PHHs (**p**), are denoted as '**H**'. LSECs and KCs are referred to as '**L**' or '**K**', respectively. Organoids are denoted as **3D**. Organoid models with LSECs and KCs are referred to as **i**3DHLK and **p**3DHLK, when assembled with either iHLCs or PHHs, respectively. When organoids are assembled only with LSECs and either iHLCs or PHHs, they will be referred to as **i**3DHL and **p**3DHL, respectively. Collagen sandwich (CS) models with iHLCs or PHHs only will be referred to as **i**CS or **p**CS.

3.3.1 Multicellular iHLC Organoids Maintain 3D Structure

iHLC organoids were immunostained with cell-specific markers (**Section 3.6**, **Figure 3.6**, **Table 3.5**). iHLCs were identified by albumin (blue), LSECs by CD32b (red), and KCs by CD163 (green) expression (**Figures 3.1B-G**). Throughout the 14-day culture period, the expression of albumin (iHLCs), CD32b (LSECs) and CD163 (KCs) was observed indicating that all cells maintained their phenotypic markers.

Although, the heights of organoids remained constant for all iHLC models over the 14 days, there were differences between the heights of mono- and multi-cellular cultures. (**Table 3.6**). By Day

14, the height of **i**3DHL and **i**3DHLK organoids was up to approximately 1.6-1.8-fold higher compared to **i**CS cultures due to the inclusion of LSECs and KCs.

3.3.2 Fluorescence Intensity of AFP Decreases in Maturing iHLCs

In differentiation and maturation protocols, the expression of AFP, a fetal marker, is used to determine if stem cells have committed to a hepatic lineage (45). On Day 1, differences in AFP fluorescence intensities were statistically insignificant ($p > 0.05$) across all iHLC models (**Section 3.6, Figures 3.1H-J**). By Days 7 and 14, the fluorescence intensity for AFP in **i**3DHLK organoids decreased ($p < 0.05$) by approximately 1.6-fold compared to **i**CS and **i**3DHL cultures (**Figures 3.1K-P**). There was no significant difference in AFP expression between PHH cultures at any time point (**Figures 3.1Q-Y**). While AFP fluorescence intensity in PHH cultures was 2.2-fold lower ($p < 0.05$) on Day 1 compared to iHLC organoids (**Figures 3.1H-J, Q-S**) by Days 7 and 14, there was no difference ($p > 0.05$) between **i**3DHLK and **p**3DHLK organoids (**Figures 3.1M, P, V, Y, Figures 3.7A-C**). This trend indicates that iHLCs, specifically in the presence of LSECs and KCs, are beginning to adopt a mature phenotype.

3.3.3 Decrease in HNF4α⁺ Correlates to an Increase in Albumin⁺ iHLCs

HNF4α, a marker of immature hepatocytes, plays a role in regulating liver development and maturation (179). Although HNF4α is present in adult hepatocytes to maintain liver function, its expression is lower compared to hepatoblasts (91). On Day 1, approximately 50% of cells in all iHLC cultures were HNF4α-positive (HNF4α⁺) (**Section 3.6, Figures 3.2A-C)**. By Day 7, the percent of HNF4α⁺ cells in **i**3DHLK organoids was lower ($30.0 \pm 1.5\%$, $p < 0.05$) than **i**CS cultures ($45.3 \pm 3.5\%$) (**Figures 3.2D-F**)**.** By Day 14, both **i**3DHL ($30.0 \pm 4.5\%$) and **i**3DHLK ($35.9 \pm 1.0\%$) organoids exhibited a significant ($p < 0.05$) decrease in the percentage of HNF4α⁺ cells compared to **i**CS cultures ($53.7 \pm 3.5\%$) (**Figures 3.2G-I**). In comparison, approximately 20% of

PHHs were HNF4α^+ in all cultures over the 14-day culture (**Figures 3.2J-R**). By Day 7, the percentage of HNF4α^+ cells was similar (p > 0.05) between **i**3DHLK and **p**3DHLK organoids (**Figures 3.2F, O**). In contrast, it took up to Day 14 for the percentage of HNF4α^+ cells in **i**3DHL and **i**3DHLK organoids to be equivalent to PHH models (p > 0.05) (**Figures 3.2H, I, Q, R, Figure 3.8A-C**).

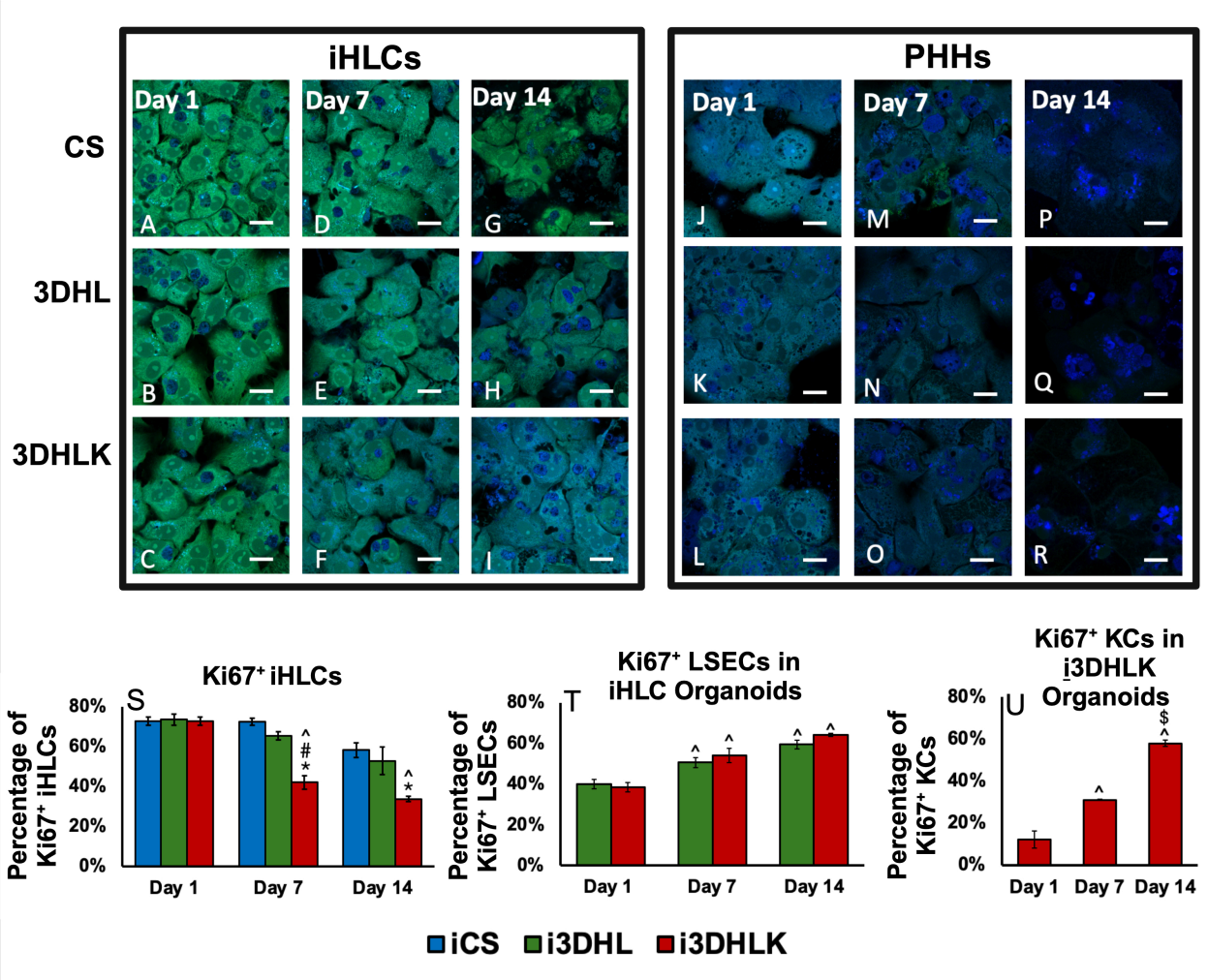

Figure 3.2 Immunostaining for HNF4α (green) and albumin (blue) in iHLC (**A-I**) and PHH (**J-R**) cultures on Days 1, 7, and 14. Scale bars = 20 μm. n = 3 biological replicates. Image analysis conducted on ≥12 images with ≥ 550 cells images for each culture. Proliferating cells in iHLC organoids from Days 1 through 14. (**S**) Percentage of Ki67$^+$ iHLCs on Days 1 – 14. (**T**) Percentage of Ki67$^+$ LSECs in iHLC organoids on Days 1 – 14. (**U**) Percentage of Ki67$^+$ KCs in iHLC organoids on Days 1 - 14. n = 3 biological replicates. Image analysis conducted on ≥12 images for each culture with ≥ 250 hepatocytes, ≥ 70 LSECs, and ≥ 100 KCs. *p < 0.05

indicates statistical significance compared to **i**CS culture. $^{\#}p < 0.05$ indicates statistical significance compared to **i**3DHL model. ^$p < 0.05$ indicates statistical significance compared to Day 1. $^{\$}p < 0.05$ indicates statistical significance compared to Day 7.

Albumin secreted by adult hepatocytes (11) is used as an indicator of maturation (45, 54). We first present results on albumin-positive cells (albumin$^+$) which are further validated by secretion (**Section 3.3.6**). On Day 1, approximately 50% of iHLCs are albumin$^+$ in all cultures (**Section 3.6**, **Figures 3.2A-C**). On Day 7, 70.0 $\pm$ 1.5% of iHLCs in **i**3DHLK organoids were albumin$^+$($p < 0.05$) compared to **i**CS cultures (54.7 $\pm$ 3.5%, **Figures 3.2D-F**). By Day 14, the percentage of albumin$^+$ iHLCs in **i**3DHL (63.7 $\pm$ 4.5%) and **i**3DHLK (64.1 $\pm$ 1.0%) organoids was higher ($p < 0.05$) than **i**CS cultures (46.3 $\pm$ 3.5%, **Figures 3.2G-I**). In PHH cultures, there were no significant ($p > 0.05$) differences in albumin$^+$ cells between any timepoints (**Figures 3.2J-R**). Interestingly, by Day 7, the percentage of albumin$^+$ cells were similar ($p > 0.05$) between **i**3DHLK and **p**3DHLK organoids (**Figures 3.2F, O**). It took 14 days for the percentages of albumin$^+$ iHLCs in **i**3DHL and **i**3DHLK organoids to be equivalent to PHH models ($p > 0.05$) (**Figures 3.2H, I, Q, R, Figure S3D-F**). These trends correlate with the decrease in HNF4α expression, suggesting that an increase in mature hepatic characteristics is accompanied by a decrease in fetal markers (179).

3.3.4 Decreases in Ki67$^+$ iHLCs through Day 14 in i3DHLK organoids

Mature hepatocytes usually exist in a non-proliferative state (21). In contrast, iHLCs are known to multiply (11). To identify if there were temporal shifts, the organoids were immunostained with Ki67, a marker that indicates that a cell may be entering a proliferative state (180) (**Section 3.6, Figure 3.2S-U, Figure 3.9)**.

On Day 1, approximately 70% of iHLCs were Ki67$^+$ in all cultures (**Figures 3.7, Figures 3.9A-C**). However, by Day 14, the percentage of Ki67$^+$ iHLCs in **i**3DHLK organoids (33.7 $\pm$ 1.3%) had decreased by approximately 2-fold compared to Day 1 (**Figures 3.9G-I**). In PHH cultures, the

percentage of Ki67$^+$ hepatocytes remained approximately 10% (**Figures 3.9J-R**, **Figure 3.9AK**). The significant decrease in Ki67$^+$ iHLCs in **i**3DHLK organoids by Day 14 demonstrates that cells are progressing towards a non-proliferative state, a characteristic of adult hepatocytes.

Hepatic non-parenchymal cells exhibited differing proliferation trends. Ki67$^+$ LSECs increased approximately 10% ($p < 0.05$) at each time point in iHLC organoids (**Figures 3.2T, Figures 3.9S-X)**, Since LSECs proliferate primarily during liver regeneration and development, their proliferation was only detected in iHLC organoids (**Figure 3.9AL)**. KCs exhibited greater changes in proliferation in iHLC organoids. Ki67$^+$ KCs in **i**3DHLK organoids increased ($p < 0.05$) approximately 4.7-fold from Day 1 (12.2 $\pm$ 4.1%) through Day 14 (57.9 $\pm$ 1.5%) (**Figures 3.2U**, **Figure 3.9AE-AG**) During this same period, the percentage of Ki67$^+$ KCs in PHH organoids decreased ($p < 0.05$) (**Figures 3.9AH-AJ, Figure 3.9AM**). KC proliferation can occur due to the secretion of HGF, a potent mitogen (181). In iHLC organoids, HGF increased significantly from Day 1 onwards (**Section 3.3.6**).

In order to understand if the potential shift to a proliferative state by KCs could result in an inflammatory microenvironment, we measured the endogenous levels of TGF-β1 (**Section 3.6**), since this cytokine can cause inflammation (182). TGF-β1 secretion decreased by approximately 3.3-fold in **i**3DHLK organoids from Days 1 to 14 (**Table 3.7**), suggesting that while KCs may be undergoing a shift towards a proliferative state, the organoids did not exhibit inflammation. TGF-β1 secretion did not change in **p**3DHLK organoids from Days 1 to 14, which corresponds to the virtually constant percentages of Ki67$^+$ cells in PHH cultures.

3.3.5 CYP2E1 and CYP3A4 Fluorescence Intensity and Biotransformation Increase in Maturing iHLCs

PHHs are used to test CYP-mediated biotransformation of drugs, toxicants, and xenobiotics (1). iHLCs have been reported to exhibit up to 40,000-fold lower expression of CYP genes than PHHs making it difficult to substitute these cells (11, 55). We measured the fluorescence intensity and biotransformation of CYP2E1 and CYP3A4 (**Section 3.6**) (12).

3.3.5.1 CYP2E1 Fluorescence Intensity: The fluorescence intensity of CYP2E1 was statistically insignificant ($p > 0.05$) between iHLC cultures on Days 1 and 7 (**Section 3.6, Figures 3.3A-F**). However, by Day 14, fluorescence intensity in both **i**3DHL and **i**3DHLK organoids was higher (approximately 2-fold, $p < 0.05$) compared to **i**CS cultures (**Figures 3.3G-I).** There were no significant ($p < 0.05$) differences in CYP2E1 fluorescence intensity in PHH cultures on any day (**Figures 3.3J-R**). Compared to iHLC cultures, the fluorescence intensity of CYP2E1 was up to 1.7-fold higher ($p < 0.05$) in PHH cultures on Days 1 and 7 (**Figures 3.3A-F, J-O**). However, by Day 14, CYP2E1 fluorescence intensity in **i**3DHL and **i**3DHLK organoids was similar ($p > 0.05$) to **p**3DHL and **p**3DHLK organoids (**Figures 3.3H, I, Q, R, Figures 3.7D-F**).

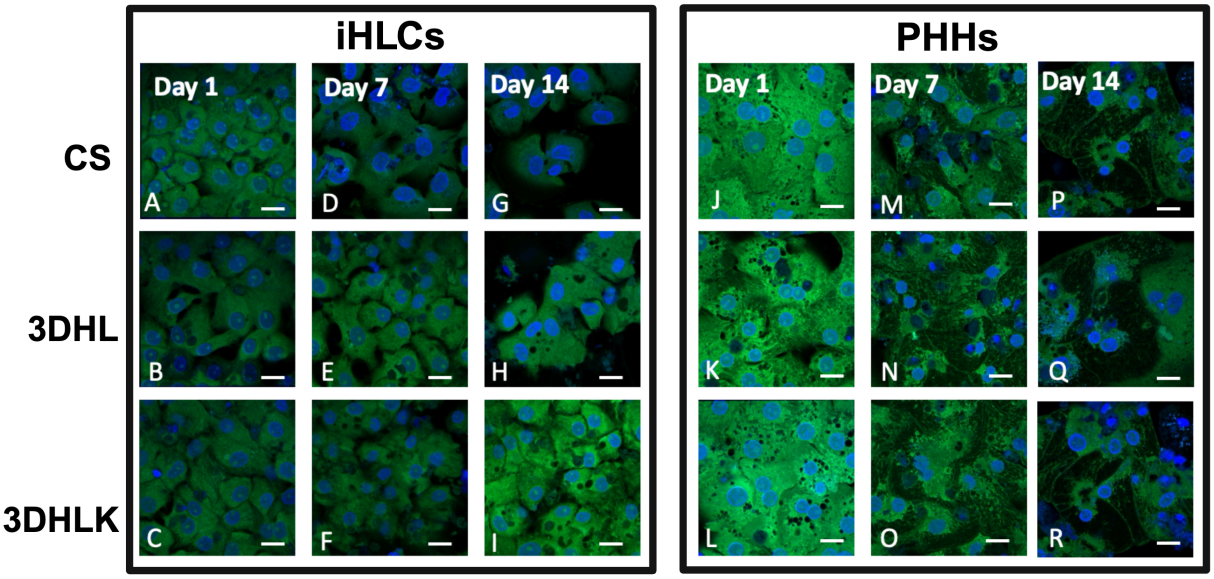

Figure 3.3 Immunostaining for CYP2E1 (green) and nuclei (blue) for iHLC (**A-I**) and PHH (**J-R**) cultures on Days 1, 7 and 14. Scale bars = 20 μm. n = 3 biological replicates. Image analysis conducted on ≥12 images with ≥ 550 cells images for each culture.

3.3.5.2 Effects of CYP2E1 Biotransformation: APAP is the leading cause of acute liver failure in the U.S (183). EtOH can result in cirrhosis, fatty liver, and cancer (184). (**Section 3.6**). When APAP (2.5 mM, LC_{50}) was administered on Day 1, iHLC cultures exhibited no response to the toxicant (**Table 3.8**). APAP administration on Day 7 resulted in higher (p < 0.05) apoptosis in **i**3DHLK organoids compared to **i**CS or **i**3DHL cultures (**Table 3.1**). The percentage of apoptotic cells in **i**3DHLK organoids did not change (p > 0.05) when APAP was administered on Day 14 (**Table 3.1**). The percent of apoptotic cells was approximately 16% in both **i**3DHLK and **p**3DHLK organoids when APAP was added on Day 7 (**Table 3.1**). However, PHH models exhibited approximately 3.5-fold higher (p < 0.05) necrosis (12) (**Table 3.1**). Due to higher necrotic death in the PHH cultures, overall cell death was higher when compared to iHLC organoids.

Table 3.1 Percentages of apoptotic, necrotic, and total cell death measured 24 h after 2.5 mM APAP administration. n ≥ 3 biological replicates.

	Administration on Day 7			Administration on Day 14		
Model	**Apoptosis (%)**	**Necrosis (%)**	**Cell Death (%)**	**Apoptosis (%)**	**Necrosis (%)**	**Cell Death (%)**
iCS	2.2 ± 1.2	6.2 ± 3.4	8.3 ± 2.9	3.9 ± 1.7	4.5 ± 0.9	8.4 ± 2.5

i3DHL	1.7 ± 0.9	5.0 ± 3.2	6.8 ± 3.8	2.1 ± 3.1	2.9 ± 3.1	5.0 ± 2.7
i3DHLK	19.6 ± 1.6	7.9 ± 2.4	27.4 ± 0.8	16.5 ± 2.8	14.1 ± 2.1	30.6 ± 2.6
pCS	12.6 ± 2.2	4.5 ± 1.1	17.2 ± 3.3	16.0 ± 0.7	20.6 ± 4.2	36.6 ± 3.9
p3DHL	6.2 ± 1.0	6.2 ± 3.4	12.4 ± 3.7	18.4 ± 3.4	22.4 ± 6.6	40.8 ± 6.4
p3DHLK	16.3 ± 2.9	27.3 ± 2.8	43.6 ± 2.7	18.1 ± 1.1	16.7 ± 2.0	34.8 ± 0.8

When EtOH (160 mM, LC_{50}) was administered on Day 1, iHLC organoids exhibited no response to this toxicant (**Table 3.10**). By Day 7, apoptosis was higher ($p < 0.05$) in the **i**3DHLK organoids compared to **i**3DHL or **i**CS cultures while necrosis was similar ($p > 0.05$) in all models (**Table 3.2**). When EtOH was added either on Day 7 or 14, both **i**3DHLK and **p**3DHLK organoids exhibited similar ($p > 0.05$) percentages of apoptotic cells (**Table 3.2**). However, the percentage of necrotic cells in **p**3DHLK organoids was consistently higher ($p < 0.05$) than **i**3DHLK models. iHLC and PHH organoids exhibited similar levels of apoptosis but differed in necrotic cell death due to EtOH administration.

Table 3.2 Percentages of apoptotic, necrotic, and total cell death measured 24 h after 160 mM EtOH administration. n ≥ 3 biological replicates.

	Administration on Day 7			**Administration on Day 14**		
Model	**Apoptosis (%)**	**Necrosis (%)**	**Cell Death (%)**	**Apoptosis (%)**	**Necrosis (%)**	**Cell Death (%)**
iCS	1.8 ± 1.4	3.6 ± 1.4	5.3 ± 2.2	12.3 ± 0.4	4.2 ± 1.1	16.4 ± 0.8
i3DHL	3.8 ± 1.0	3.5 ± 1.1	7.3 ± 2.0	3.6 ± 2.0	6.5 ± 0.2	10.1 ± 2.0
i3DHLK	20.6 ± 1.9	9.8 ± 2.9	30.3 ± 1.9	24.7 ± 1.12	5.5 ± 1.6	30.2 ± 2.1
pCS	12.7 ± 1.3	6.6 ± 1.2	19.3 ± 1.5	22.1 ± 3.5	25.7 ± 4.2	47.9 ± 6.8
p3DHL	5.3 ± 1.1	6.0 ± 3.4	11.3 ± 4.4	21.3 ± 7.0	24.3 ± 7.1	45.6 ± 13.1
p3DHLK	19.7 ± 1.0	29.0 ± 3.2	48.6 ± 4.2	21.6 ± 7.3	36.0 ± 2.7	57.5 ± 7.9

3.3.5.3 CYP3A4 Fluorescence Intensity: CYP3A4 is an enzyme that metabolizes approximately 50% of drugs and pharmaceuticals (12). The fluorescence intensity of CYP3A4 was identical in all iHLC models on Day 1 (**Section 3.6**, **Figures 3.4A-C**). The fluorescence intensity of CYP3A4 was 2.1-fold and 2.8-fold higher ($p < 0.05$) in **i**3DHLK cultures on Days 7 and 14, respectively compared to **i**CS cultures (**Figures 3.4D, F, G, I**). The fluorescence intensity did not vary significantly in any PHH culture at any timepoint **(Figures 3.4J-R**). On Days 7 and 14, CYP3A4

fluorescence intensity in **i**3DHLK and **p**3DHLK organoids was similar ($p > 0.05$) (**Figures 3.7G-I**), indicating that iHLCs were now expressing another marker of mature hepatocytes.

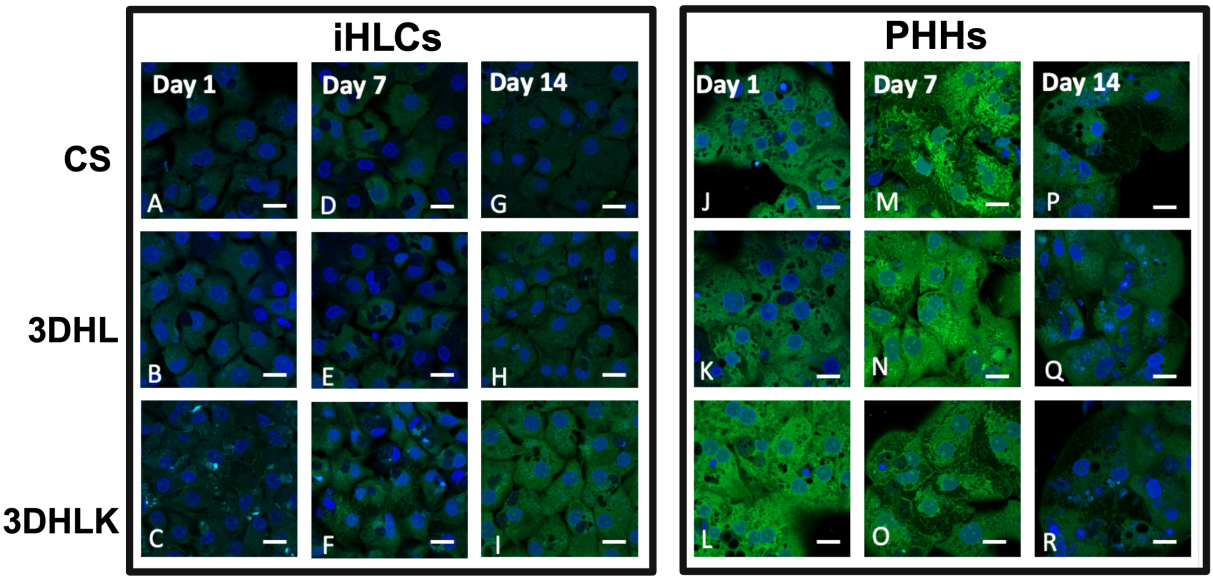

Figure 3.4 Immunostaining for CYP3A4 (green) and nuclei (blue) for iHLC (**A-I**) and PHH (**J-R**) cultures on Days 1, 7 and 14. Scale bars = 20 μm. n = 3 biological replicates. Image analysis conducted on ≥12 images with ≥ 550 cells images for each culture.

3.3.5.4 CYP3A4 Effects of CYP3A4 Biotransformation: When RIF, an anti-tuberculosis antibiotic (185) (0.36 μM, EC_{50}) (186) was administered on Day 1, iHLC organoids did not exhibit any response ($p > 0.05$) to the toxicant (**Section 3.6**, **Table 3.12**). After administering on either Day 7 or 14, **i**3DHLK organoids exhibited higher ($p < 0.05$) apoptosis compared to both **i**CS and **i**3DHL cultures (**Table 3.3**). Overall cell death was higher ($p < 0.05$) in **i**3DHLK organoids compared to **i**CS and **i**3DHL cultures on Days 7 and 14 (**Table 3.3**).

Table 3.3 Percentages of apoptotic, necrotic, and total cell death measured 24 h after 0.36 μM RIF administration. n = 3 biological replicates.

	Administration on Day 7			Administration on Day 14		
Model	**Apoptosis (%)**	**Necrosis (%)**	**Cell Death (%)**	**Apoptosis (%)**	**Necrosis (%)**	**Cell Death (%)**
iCS	8.0 ± 3.3	1.8 ± 1.4	9.8 ± 1.9	3.2 ± 0.0	3.9 ± 0.8	7.1 ± 0.8
i3DHL	7.5 ± 2.3	1.7 ± 1.2	9.1 ± 3.2	5.6 ± 1.5	5.3 ± 2.5	10.9 ± 3.9
i3DHLK	20.3 ± 2.8	9.4 ± 2.5	29.6 ± 4.9	18.1 ± 2.3	14.5 ± 2.8	32.5 ± 4.2
pCS	9.2 ± 2.1	2.0 ± 0.5	11.2 ± 2.5	11.5 ± 1.0	2.9 ± 0.3	14.4 ± 1.3

p3DHL	16.8 ± 3.0	6.4 ± 0.6	23.3 ± 2.4	9.4 ± 1.4	7.6 ± 1.1	17.0 ± 2.4
p3DHLK	28.2 ± 1.9	15.7 ± 2.0	41.8 ± 3.9	23.5 ± 3.1	21.7 ± 3.0	45.2 ± 1.1

By Day 7, approximately 20% of cells were apoptotic in **i**3DHLK and **p**3DHLK ($p > 0.05$) organoids. Overall, on Day 7, cell death was higher ($p < 0.05$) in **p**3DHLK cultures compared to **i**3DHLK models due to higher necrosis ($p < 0.05$). However, by Day 14, there were no significant differences ($p > 0.05$) in the percentage of apoptotic or necrotic cells between **i**3DHLK and **p**3DHLK organoids (**Table 3.3**). The progressive capability in biotransformation highlights that if iHLCs are present in a microenvironment that includes LSECs and KCs, after 14 days, they can exhibit similar CYP3A4 metabolism as PHHs. We hypothesized that autocrine and paracrine signaling among the three cell types may be essential for iHLC maturation. Accordingly, we measured the concentrations of signaling molecules over the 14-day period to obtain a deeper understanding on maturation.

3.3.6 Endogenous Secretion of Maturation Molecules Promotes iHLC Maturation

We measured the endogenous secretion of HGF, OSM, and PGE2 (**Section 3.6**), three molecules that are critical regulators of liver maturation (181, 187, 188), to elucidate the mechanisms that drive the decrease in fetal and increase in adult hepatocyte markers in the organoids. The secretion of each molecule was first measured in monocultures to determine which cell type was primarily responsible for its production. Endogenous secretion of proteins from NPC monocultures were only measured on Day 1 since these cells de-differentiate in 2D cultures (7).

3.3.6.1 LSECs Secrete HGF: HGF In LSEC monocultures, HGF secretion was approximately 137-fold higher compared to other cell types (**Table 3.4**). Therefore, we identified LSECs as primarily responsible for endogenous HGF in the organoids (189). Over the first seven days of the culture period, HGF increased by 2.9 and 1.7-fold in **i**3DHL and **i**3DHLK organoids, respectively and plateaued thereafter (**Figure 3.5A)**. In cultures that did not contain LSECs, HGF

remained virtually constant. In contrast, PHH organoids did not exhibit any HGF secretion (**Table 3.4**). HGF is secreted during injury or development, which may explain why it is detected only in iHLC organoids (181).

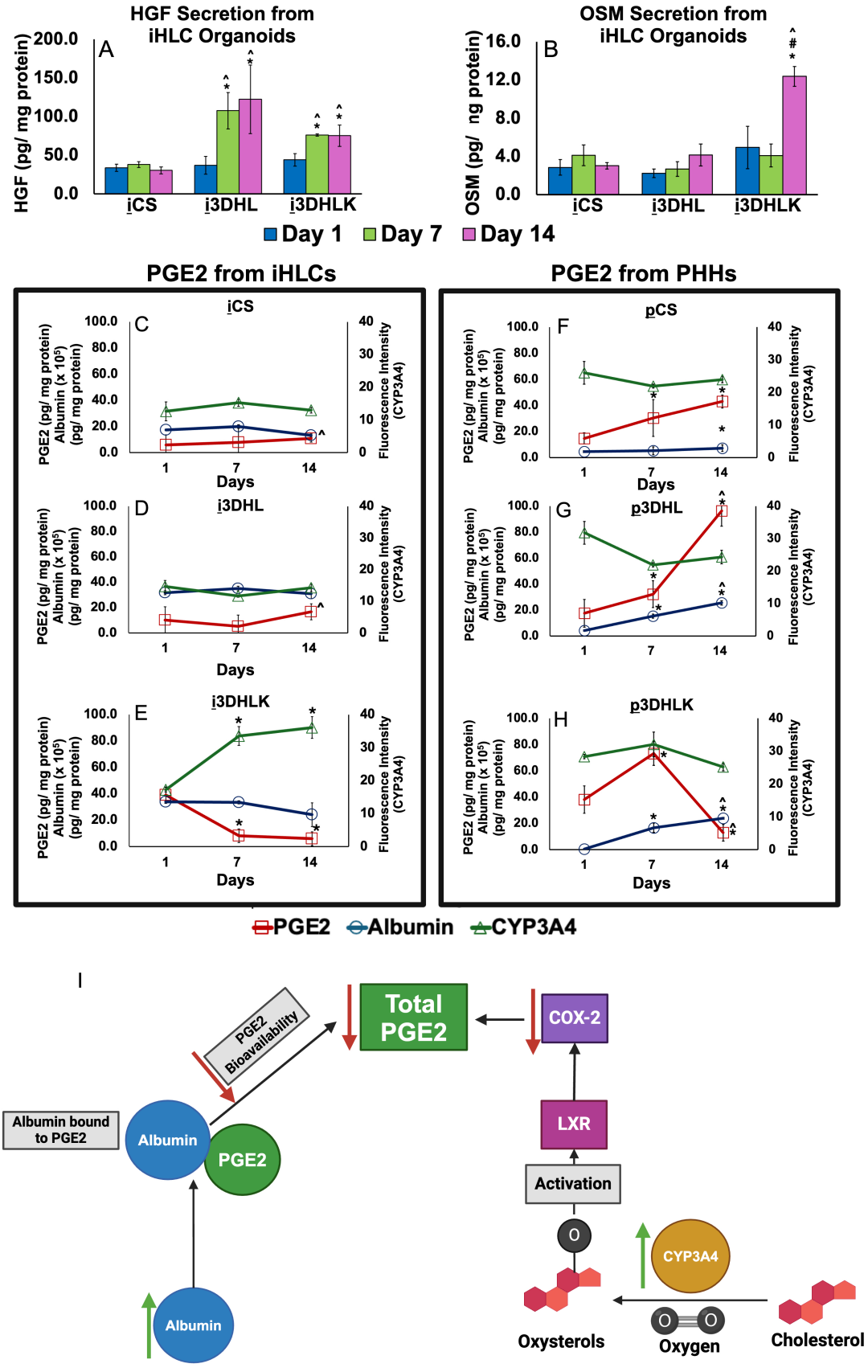
HGF Secretion from iHLC Organoids
A
HGF (pg/ mg protein)
200.0
150.0
100.0
50.0
0.0
iCS
i3DHL
i3DHLK
OSM Secretion from iHLC Organoids
B
OSM (pg/ ng protein)
16.0
12.0
8.0
4.0
0.0
Day 1
Day 7
Day 14
PGE2 from iHLCs
PGE2 from PHHs
iCS
pCS
i3DHL
p3DHL
i3DHLK
p3DHLK
C
D
E
F
G
H
PGE2 (pg/ mg protein)
Albumin (x 10⁵) (pg/ mg protein)
Fluorescence Intensity (CYP3A4)
Days
PGE2
Albumin
CYP3A4
I
Total PGE2
PGE2 Bioavailability
COX-2
Albumin bound to PGE2
Albumin
PGE2
LXR
Activation
CYP3A4
Oxysterols
Oxygen
Cholesterol

Figure 3.5 Endogenous secretion of maturation molecules in iHLC and PHH cultures. (**A**) HGF and (**B**) OSM secretion in iHLC organoids (pg/ mg protein). n = 3 biological replicates. The value obtained from culture medium was subtracted from the raw data and then normalized to protein content in the organoid at each time point. *$p < 0.05$ indicates statistical significance compared to CS model. #$p < 0.05$ indicates statistical significance compared to 3DHL model. ^$p < 0.05$ indicates statistical significance compared to Day 1. PGE2 (pg/ mg protein) and albumin (x 10^5 pg/ mg protein) secretion and fluorescence intensity (CYP3A4) from (**C-E**) iHLC and (**F-H**) PHH models. n = 3 biological replicates for each organoid for all measurements. Culture medium values were subtracted from the raw data and then the concentration was normalized to protein content in the organoid at each time point. Image analysis was conducted on ≥12 images with ≥ 550 cells for each culture/organoid. *$p < 0.05$ indicates statistical significance compared to Day 1. ^$p < 0.05$ indicates statistical significance compared to Day 7. (**I)** On Days 7 and 14, albumin and CYP3A4 may modulate PGE2 expression. As albumin increases, it binds to and reduces the amount of available PGE2, preventing this ligand from binding to its receptor on the cell membrane. In the cell, CYP450 enzymes, e.g. CYP3A4, can oxidize cholesterol to form oxysterols, which activate LXR. COX-2 is inhibited when LXR increases, leading to decreased PGE2 production.

Table 3.4 Secretion of HGF, OSM and PGE2 in LSEC, KC, iHLC, and PHH organoids/ cultures (pg/ mg protein). Concentrations were calculated by subtracting individual culture medium values and then normalized to the protein content in the organoid at each time point. n = 3 biological replicates. (-) indicates that the concentration of the molecule in the culture was lower than that of the culture medium.

		HGF (pg/ mg protein)	OSM (pg/ mg protein)	PGE2 (pg/ mg protein)
Day 1	**LSECs**	302.3 ± 40.3	0.4 ± 0.7	15.4 ± 0.8
	KCs	2.2 ± 1.9	12.9 ± 4.6	7.0 ± 6.1
	iCS	35.0 ± 8.5	2.8 ± 0.8	6.0 ± 7.3
	i3DHL	39.3 ± 15.0	2.2 ± 0.5	10.8 ± 10.2
	i3DHLK	44.5 ± 8.2	4.9 ± 2.2	39.4 ± 6.7
	pCS	–	–	14.8 ± 3.8
	p3DHL	–	–	17.6 ± 9.4
	p3DHLK	–	–	38.4 ± 18.3
Day 7	**iCS**	39.7 ± 5.8	4.1 ± 1.1	7.8 ± 11.7
	i3DHL	115.6 ± 33.7	2.7 ± 0.8	5.3 ± 8.0
	i3DHLK	76.4 ± 2.9	4.1 ± 1.2	8.1 ± 4.5
	pCS	–	–	30.4 ± 12.3
	p3DHL	–	–	32.3 ± 9.1
	p3DHLK	–	–	73.6 ± 2.3
Day 14	**iCS**	33.0 ± 5.3	3.0 ± 0.3	10.8 ± 2.3
	i3DHL	123.3 ± 43.9	4.1 ± 1.2	17.0 ± 6.0
	i3DHLK	76.0 ± 14.1	12.4 ± 1.0	6.1 ± 4.6
	pCS	–	–	43.1 ± 5.0
	p3DHL	–	–	96.4 ± 11.8
	p3DHLK	–	–	13.0 ± 9.8

3.3.6.2 KCs Secrete OSM: In monocultures, OSM secretion by KCs was up to 32.3-fold and 4.5-fold higher compared to LSECs and iHLCs on Day 1, respectively (**Table 3.4**) (178). On Day 14, OSM secretion was higher ($p < 0.05$) than Days 1 or 7 only in **i**3DHLK organoids (**Figure 3.5B)**. The increase in OSM is correlated to a higher number of $Ki67^+$ KCs on Day 14. In PHH organoids, endogenous OSM was not detected throughout the culture period (**Table 3.4)**.

3.3.6.3 iHLC and PHH Organoids Exhibit Different Temporal Patterns for PGE2 Secretion:

The secretion of PGE2 in LSEC monocultures was approximately 2-fold higher than KC or iHLC but similar to PHH monocultures on Day 1 (**Table 3.4**). In iHLC organoids, we focus upon the tri-cellular systems since they exhibit the highest maturation and most significant temporal variations in PGE2 levels. On Day 1, PGE2 concentration in **i**3DHLK organoids was approximately 28% higher than the additive secretion from each monoculture (**Figure 3.5E**). By Days 7 and 14, PGE2 levels went down by 4.9-fold and 6.5-fold, respectively. During the culture period, $Ki67^+$ iHLCs decreased by approximately 2-fold, which correlated with the PGE2 trends. Since PGE2 is implicated in liver developmental pathways (188), its levels may be decreasing since iHLCs have begun to exhibit multiple markers of maturation. In contrast, PGE2 levels decrease by 3-fold from Days 7 to 14 in **p**3DHLK cultures (**Figure 3.5H**). These trends suggest that other mechanisms may be activated (**Section 3.4**).

3.3.6.4 PGE2 Levels Correlate to Albumin Secretion and CYP3A4 Expression in 3DHLK Organoids: PGE2 can be modulated by the bioavailability of albumin and through the activation of the liver X receptor (LXR) (**Figure 3.5I**) (190, 191). CYP450 enzymes, specifically, CYP3A4, can form oxysterols that induce LXR, which in turn inhibits PGE2 (192, 193). Albumin can also modulate PGE2 bioavailability upon binding to the prostaglandin (190).

A significant increase in the fluorescence intensity of CYP3A4 was observed only in **i**3DHLK organoids on Day 7 and maintained up to Day 14 (**Section 3.3.5**). PGE2 secretion and CYP3A4 expression exhibit an inverse relationship in **i**3DHLK organoids throughout the culture period suggesting that CYP3A4 may be one mechanism by which PGE2 levels are modulated. However, albumin levels in iHLCs organoids did not vary significantly over time in any of the culture conditions, indicating that the bioavailability of this protein may not play a role in PGE2 regulation in **i**3DHLK organoids.

In **p**3DHLK organoids, albumin secretion increased approximately 4 and 5-fold on Days 7 and 14, respectively, compared to Day 1. The increase in albumin levels (**Table 3.14**) correlated to a 5.7-fold decrease in PGE2 by Day 14 compared to Day 7. The fluorescence intensity for CYP3A4 did not change in PHH models, suggesting that regulation of PGE2 in the presence of PHHs may be controlled by albumin bioavailability. We hypothesize that either CYP3A4 expression or albumin may contribute to the reduction in PGE2 levels but only in the presence of KCs. Taken together, we demonstrate that LSECs and KCs are primarily responsible for the secretion and regulation of molecules that drive maturation in multicellular iHLC organoids.

3.4 Discussion

The primary goal of this study was to demonstrate that the unique hepatic microenvironment established when human LSECs and KCs are in close proximity to iHLCs in an organoid can lead to complete iHLC maturation through the endogenous secretion of signaling molecules. Previous studies on iHLC maturation have reported the administration of chemical cocktails using a variety of temporal profiles where the concentrations of exogenously added reagents can be up to 6-orders of magnitude higher than present *in vivo* (50, 60, 63, 101). Non-physiological concentrations of exogenous chemicals cause alterations in cellular signaling. We demonstrate

that the *in vivo*-like concentrations of endogenously secreted HGF, OSM, and PGE2 (**Table 3.4**) are sufficient to completely and reproducibly mature iHLCs. In the presence of both LSECs and KCs, iHLCs can mature more rapidly due to a combination of inter- and intra-cellular signaling from both hepatic cell types while the inclusion of LSECs alone requires more time for iHLC maturation.

Two critical signaling molecules that mark hepatocyte differentiation, HGF and OSM, are detected only in iHLC organoids. Even more significant was that the concentrations of each signaling molecule were similar or almost identical to those reported *in vivo* (**Table 3.4**) (176, 194, 195). The endogenous secretions of HGF, PGE2, and OSM signaling can initiate different pathways that either inhibit fetal or induce adult hepatic markers. The synergism between these molecules may explain maturation is more rapid in organoids when both LSECs and KCs present.

HGF, a potent mitogen, activates the c-met receptor in hepatocytes by tyrosine phosphorylation (181). LSECs may secrete this molecule to stimulate proliferation (189). HGF can also be internalized and degraded rapidly through its receptor, c-met, in hepatocytes within 30 minutes (196). This could explain why HGF concentrations are lower in organoids (**Table 3.4**) compared to LSEC monocultures.

PGE2 is generated through the metabolism of arachidonic acid by cyclooxygenase-2 (COX-2) (197). HGF can upregulate COX-2 expression leading to PGE2 production (198). A positive paracrine feedback mechanism occurs wherein PGE2 can induce HGF (181, 188, 198). PGE2 can also initiate the secretion of OSM from KCs (199, 200). OSM, a member of the IL-6 family, induces hepatocyte maturation during liver organogenesis (187). We hypothesize that the significant increase in OSM secretion in **i**3DHLK organoids on Day 14 is due to potential KC proliferation (**Section 3.4**).

Temporal variations in PGE2 levels were observed in PHH and iHLC organoids although their patterns differed. To understand the underlying reasons behind the fluctuation, we correlated the temporal variation of PGE2 to albumin bioavailability and CYP3A4 expression (190, 191). Albumin decreases circulating PGE2 by reducing its binding capacity to EP-receptors (190). Additionally, the decrease in PGE2 levels in **p**3DHLK cultures may be due to IL-4 secretion by KCs that can suppress COX-2 (201). CYP450 enzymes can form oxysterols that activate the transcriptional activity of LXR (191-193). Oxysterols have important roles in embryonic development and organ regeneration by binding to the Hedgehog signaling pathway (202), which may explain why PGE2 and CYP3A4 have opposing trends over time in **i**3DHLK organoids.

Adult hepatocytes are typically quiescent and enter the G1 phase of the cell cycle upon injury or regeneration (21). The percentage of $Ki67^+$ iHLCs decreases only in **i**3DHLK organoids, indicating that the cells are transitioning from a stem-cell state to a differentiated phenotype. This trend coincides with a decrease in PGE2 levels. Continued secretion of PGE2 is detected primarily during stem cell proliferation (203). Both LSECs and KCs can proliferate during liver regeneration when mitogens such as HGF are secreted, which may explain why these NPCs only proliferate in iHLC organoids (189). Although KCs can proliferate, the decrease in TGF-β1 secretion in **i**3DHLK organoids indicates that inflammation is not occurring (182).

Cell-cell signaling has been shown to improve the functionality of iHLCs (74, 76). Takebe et. al. investigated how signaling from human umbilical vein endothelial cells and mesenchymal stem cells further differentiated iPSC-hepatic endoderm cells by generating functional and vascularized human liver buds that were transplanted in mice (76). Although the liver buds exhibited improved functionality compared to iHLCs alone, an *in vivo* environment was found to be necessary for maturation. Ouchi et. al. assembled an organoid with iHLCs, Kupffer-like cells, and hepatic

stellate-like cells to recapitulate steatohepatitis (74). While the organoids were able to emulate aspects of steatohepatitis, they exhibited significant downregulation of hepatocyte genes compared to the human liver (74). Neither study reported a phenotypic or functional comparison to PHHs *in vitro* (74, 76). If PHHs are to be substituted with iHLCs *in vitro*, it is critical to elucidate how iHLCs match adult hepatocyte properties (55).

3.5 Conclusions and Future Work

The maturation of iHLCs reported herein is based on the importance of and inherent need for cell-cell communications while also providing a novel and systematic platform for liver research. This approach relies on mimicking a hepatic microenvironment and modulated signaling instead of external additives. In the future, the inclusion of stellate cells and cholangiocytes may provide additional maturation mechanisms.

3.6 Supplemental Material

3.6.1 Supplemental Methods

3.6.1.1 KCs Secrete OSM: KCs from Thermofisher Scientific were maintained in Advanced DMEM supplemented with FBS (5% v/v) and a Thawing Cocktail (3.6% v/v) which comprised of Pen-Strep (10,000 U/ mL), human recombinant insulin (4 mg/ mL), GlutaMAX (200 nm), and HEPES solution (1 M) at a pH of 7.4. KCs from Novabiosis were thawed in Kupffer Plating Medium and then Kupffer Maintenance Medium from the manufacturer 24 h before organoid assembly. KC monocultures were seeded on collagen gels maintained in iHLC media.

3.6.1.2 Immunostaining for Phenotypic Studies: Glass-bottom well plates were activated to promote the adhesion of collagen gels using previously reported procedures (17). Cultures were fixed with a 2% (w/v) glutaraldehyde in PBS (1 X) solution followed by a 0.1% $NaBH_4$ solution in

PBS (1 X) and 0.1% Triton-X solution in PBS (1 X). A blocking solution of 1.5% (v/v) goat serum in 1% (w/v) BSA in PBS or 5% (v/v) horse serum in 1% (w/v) BSA in PBS (1 X) solution was added to cultures. A list of primary and secondary antibodies is presented in **Table 3.5**. The nuclei were stained with Hoechst 33258 (Thermofisher). Imaging was conducted on Zeiss LSM 800 and 880 confocal microscopes. Image analysis was conducted with Nikon® NIS-Elements Software. 3D renderings of the cultures/ organoids were constructed with ImageJ. Fluorescence intensity was measured for $\geq$ 550 cells for every culture and time point.

3.6.1.3 Administration of Toxicants and Measuring Mode of Cell Death: APAP (2.5 mM), EtOH (160 mM), and RIF (0.36 μM) were dissolved in culture medium at either their respective LC_{50} (lethal concentration 50) or EC_{50} (half maximal effective concentration) values and administered on Days 1, 7, and 14 (12, 186, 204). Percentages of apoptotic, necrotic, and live cells were determined through a commercially available kit (Apoptotic, Necrotic, and Healthy Cell Quantification Kit, Biotium, Fremont, CA). Imaging was immediately conducted on Zeiss LSM 800 or 880 confocal microscopes. Image analysis was conducted with Nikon® NIS-Elements Software.

3.6.1.4 Measuring Concentrations of Signaling Molecules: The concentrations of HGF, OSM, PGE2, and albumin were measured using commercially available kits (Abcam, Cambridge, UK) as per the manufacturer's protocol. The concentration of TGF-β1 was measured using a commercially available kit (Thermofisher). The concentrations of each protein were determined by calibrating to a standard curve at an absorbance of 450 nm.

3.6.2 Supplemental Figures

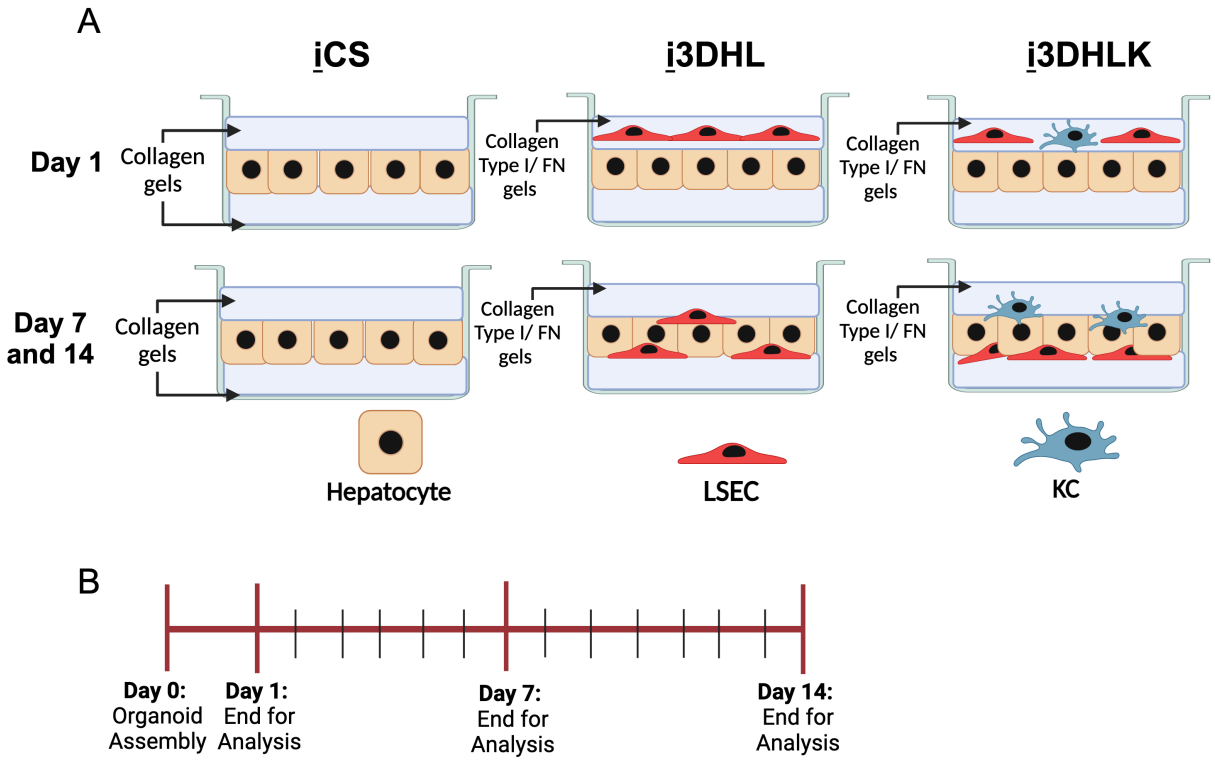

Figure 3.6 (**A**) Representative schematics of CS cultures or 3D organoids with iHLCs (**i**) (H), LSECs (L), and KCs (K) on Day 1 and Days 7 or 14. (**B**) Timeline of organoid assembly with iHLCs and PHHs.

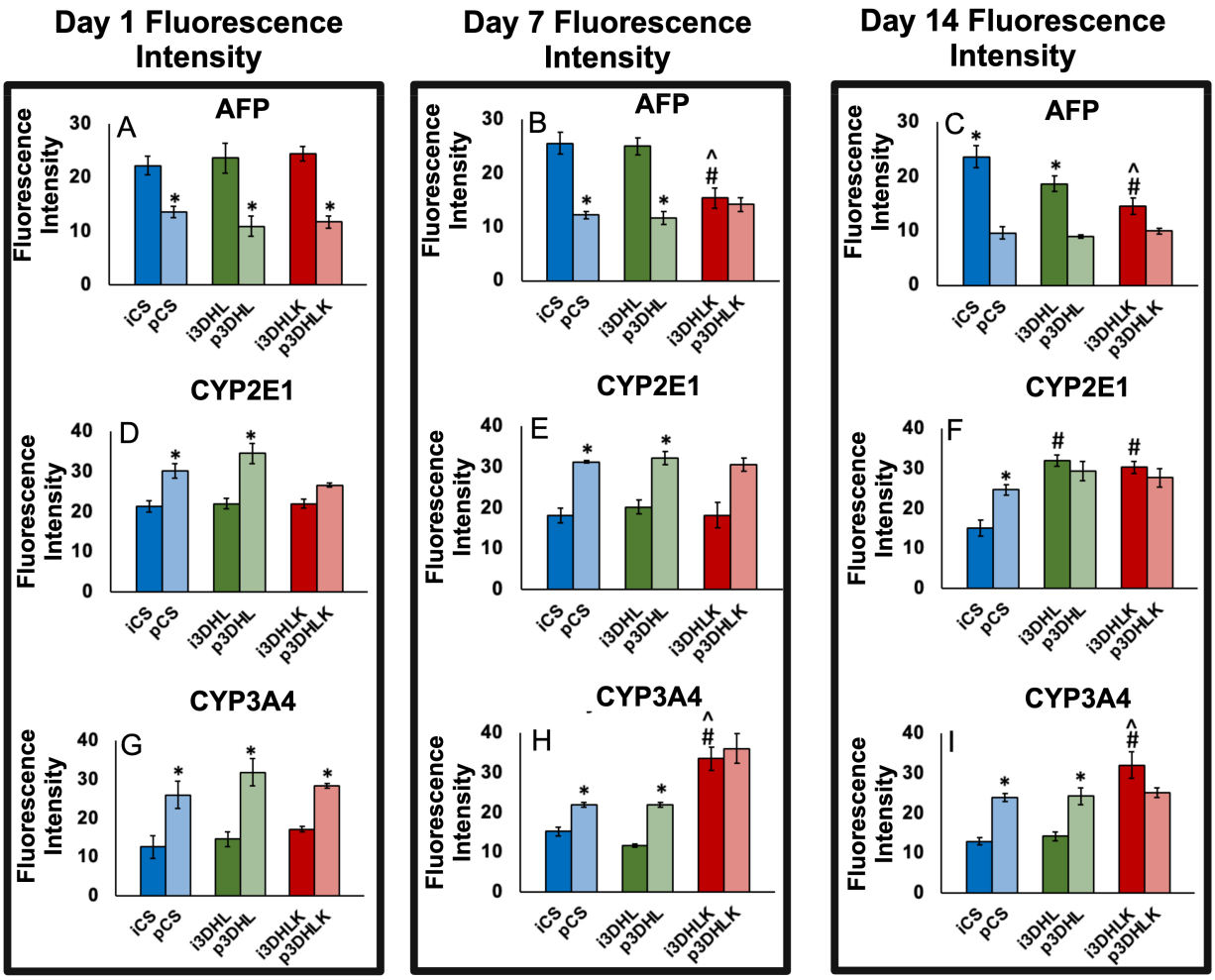

Figure 3.7 Fluorescence intensity analysis for AFP on Days 1 – 14 (**A-C**). Fluorescence intensity analysis for CYP2E1 on Days 1 – 14 (**D-F**). Fluorescence intensity analysis for CYP3A4 on Days 1 – 14 (**G-I**). $^{*}p < 0.05$ indicates statistical significance compared to equivalent iHLC culture/ organoid. $^{\#}p < 0.05$ indicates statistical significance compared to CS culture. $^{\wedge}p < 0.05$ indicates statistical significance compared to 3DHL model. n = 3 biological replicates. Image analysis was conducted on ≥12 images with ≥550 cells for each organoid.

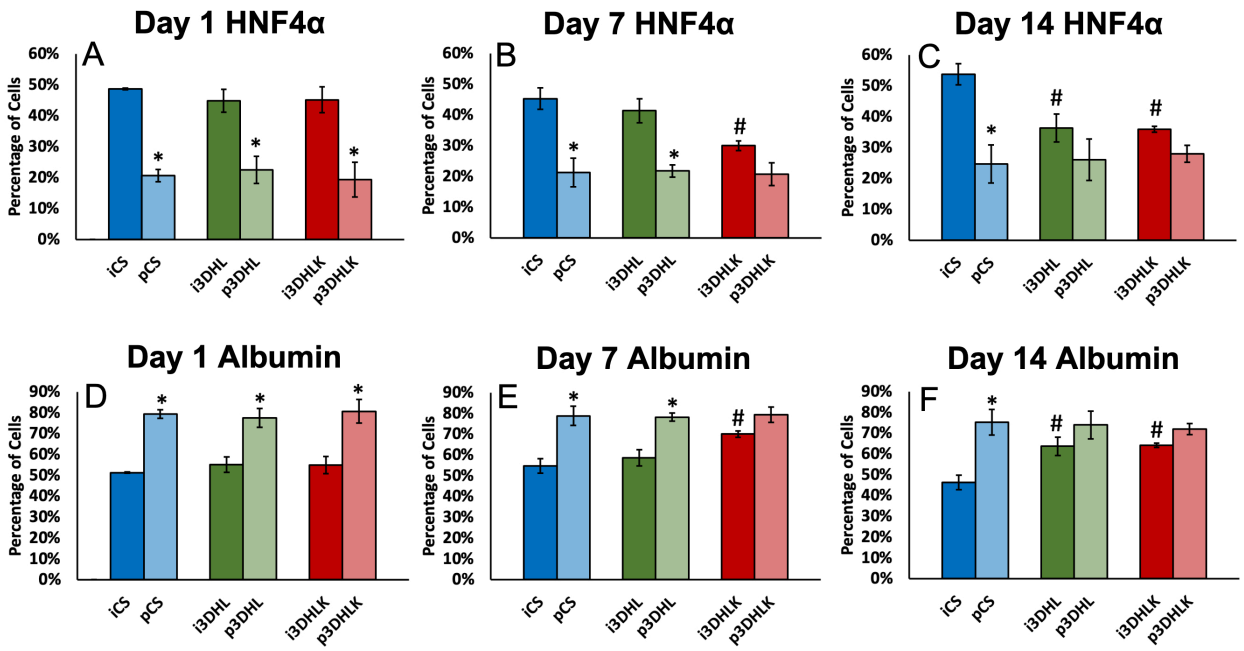

Figure 3.8 Percentage of cells expressing HNF4α on Days 1 – 14 (**A-C**). Percentage of cells expressing albumin on Days 1 – 14 (**D-F**). n = 3 biological replicates. Image analysis conducted on ≥12 images with ≥ 550 cells for each culture. *$p < 0.05$ indicates statistical significance compared to equivalent iHLC culture/ organoid. $^{\#}p < 0.05$ indicates statistical significance compared to CS culture. ^$p < 0.05$ indicates statistical significance compared to 3DHL model.

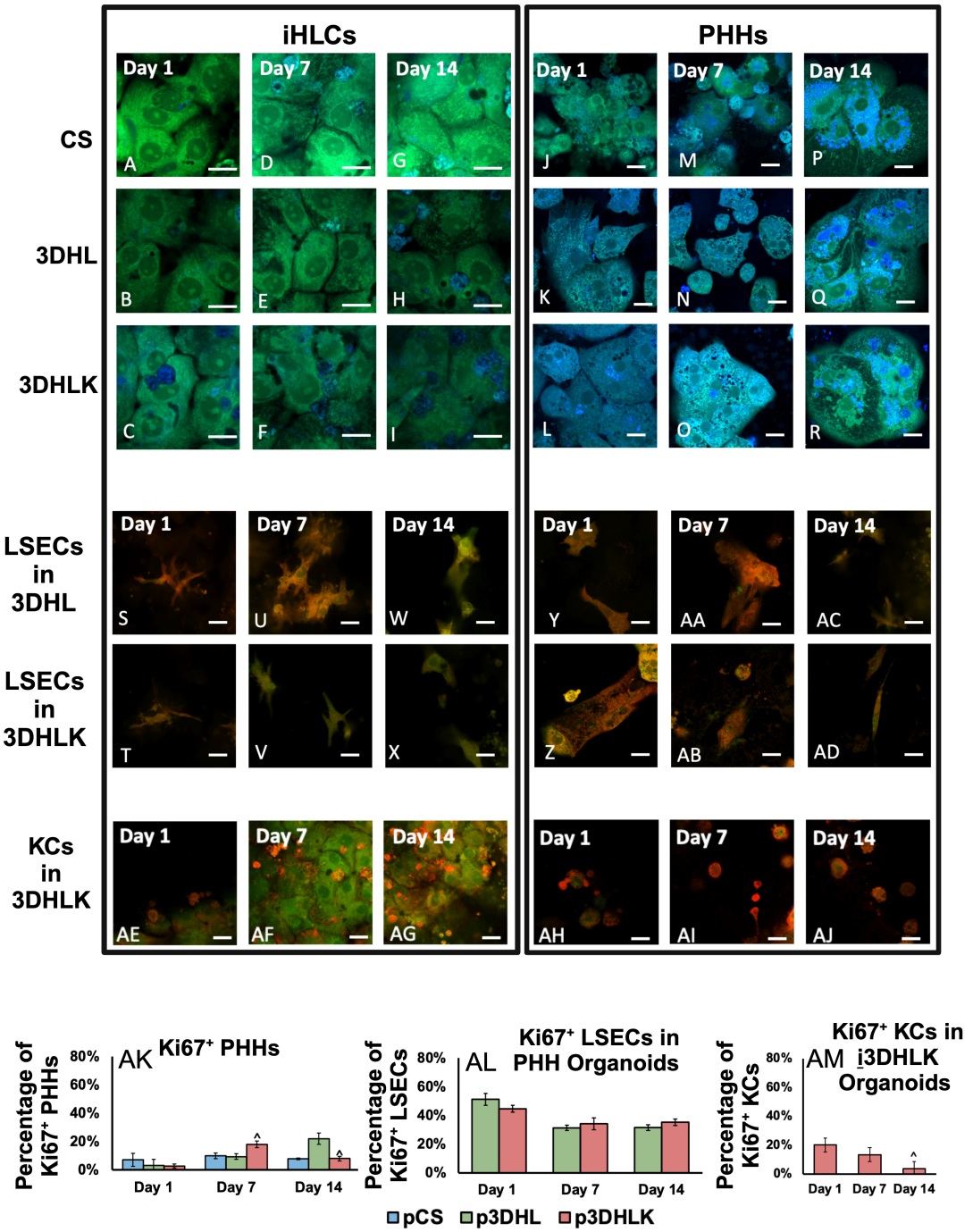

Figure 3.9 Immunostaining for Ki67 (green) and albumin (blue) for hepatocytes in iHLC (**A-I**) and PHH (**J-R**) cultures on Days 1, 7, and 14. Immunostaining for Ki67 (green) and SE-1 (red) for LSECs in iHLC (**S-X**) and PHH (**Y-AD**) organoids on Days 1, 7, and 14. Immunostaining for Ki67 (green) and CD163 (red) for KCs in **i**3DHLK (**AE-AG**) and **p**3DHLK (**AH-AJ**) organoids on Days 1, 7, and 14. All scale bars = 20 μm. Percentages of proliferating cells in PHH organoids from Day 1 through 14. (**AK**) Percentage of Ki67$^+$ PHHs on Days 1 – 14. (**AL**) Percentage of Ki67$^+$ LSECs in PHH organoids on Days 1 – 14. (**AM**) Percentage of Ki67$^+$ KCs in PHH organoids on Days 1 – 14. n = 3 biological replicates. Image analysis conducted on ≥12 images for each culture with ≥ 250 hepatocytes, ≥ 70 LSECs, and ≥ 100 KCs. ^$p < 0.05$ indicates statistical significance compared to Day 1.

3.6.3 Supplemental Tables

Table 3.5 Primary and secondary antibodies used for immunostaining phenotypic hepatic markers.

Primary Antibody	Secondary Antibody
Rabbit anti-human HNF-4α (Abcam, Cambridge, UK)	Chicken anti-rabbit FITC (Novus Biologicals, Englewood, CO)
Sheep Serum anti-human albumin (Abcam)	Donkey anti-sheep DAPI-conjugated (Thermofisher Scientific)
Mouse anti-human AFP (Santa Cruz Biotechnology, Dallas, TX)	Goat anti-mouse Alexa Fluor 594 (Thermofisher Scientific)
Rabbit anti-human CYP2E1 (Thermofisher Scientific)	Chicken anti-rabbit Alexa Fluor 488 (Thermofisher Scientific)
Rabbit anti-human CYP3A4 (Thermofisher Scientific)	Chicken anti-rabbit Alexa Fluor 488
Rabbit anti-human Ki67 (Abcam)	Chicken anti-rabbit Alexa Fluor 488
Mouse anti-human CD163 (Abcam)	Goat anti-mouse Alexa Fluor 594

Table 3.6 Z-heights of each iHLC culture/ organoid on Days 1 – 14. The z-heights were measured with n≥ 15 images across n ≥ 3 biological replicates for each condition.

	Day 1	Day 7	Day 14
iCS	11.5 ± 1.3	8.4 ± 2.7	9.0 ± 1.7
i3DHL	16.0 ± 2.2	15.8 ± 2.0	14.6 ± 1.5
i3DHLK	15.7 ± 1.4	16.7 ± 2.0	15.8 ± 1.6

Table 3.7 TGF-β1 secretion in **i**3DHLK and **p**3DHLK organoids on Days 1 and 14. Culture medium values were subtracted from the raw data and then the concentration was normalized to the protein content in the organoid at each time point (pg/ mg protein). n = 3 biological replicates. (-) indicates that the concentration was undetectable.

Media/Culture	pg/ mL	Day 1 (pg/ mg protein)	Day 14 (pg/ mg protein)
iHLC Media	–		
PHH Media	159.0 ± 89.0		
i3DHLK		117.4 ± 179.9	35.8 ± 59.0
p3DHLK		55.7 ± 58.9	55.5 ± 51.8

Table 3.8 Percentage of apoptotic, necrotic, and total cell death measured 24 h after 2.5 mM APAP administration on Day 1. n ≥ 3 biological replicates for each condition.

	Untreated on Day 1			Administration on Day 1		
Model	**Apoptosis (%)**	**Necrosis (%)**	**Cell Death (%)**	**Apoptosis (%)**	**Necrosis (%)**	**Cell Death (%)**
iCS	5.9 ± 2.2	0.9 ± 0.5	6.7 ± 2.4	5.3 ± 2.8	4.7 ± 1.9	10.0 ± 1.7
i3DHL	2.7 ± 1.2	5.1 ± 1.7	7.8 ± 2.7	2.2 ± 0.6	4.5 ± 1.1	6.7 ± 0.6
i3DHLK	3.4 ± 1.9	2.1 ± 0.9	5.5 ± 2.9	3.6 ± 2.7	2.3 ± 1.0	5.8 ± 3.7
pCS	6.8 ± 3.5	3.4 ± 2.4	10.2 ± 4.5	14.3 ± 1.6	3.6 ± 0.6	17.9 ± 2.2
p3DHL	8.4 ± 2.9	4.0 ± 0.6	12.3 ± 3.2	12.1 ± 3.5	14.2 ± 0.7	26.3 ± 9.4
p3DHLK	3.6 ± 1.4	2.8 ± 0.6	6.8 ± 2.0	16.2 ± 1.4	25.9 ± 3.3	42.1 ± 3.0

Table 3.9 Percentage of apoptotic, necrotic, and total cell death measured in untreated samples on Days 7 and 14. n ≥ 3 biological replicates for each condition.

	Untreated on Day 7			Untreated on Day 14		
Model	**Apoptosis (%)**	**Necrosis (%)**	**Cell Death (%)**	**Apoptosis (%)**	**Necrosis (%)**	**Cell Death (%)**
iCS	0.7 ± 0.2	6.2 ± 1.2	6.9 ± 1.1	5.4 ± 2.5	2.9 ± 1.2	8.4 ± 3.0
i3DHL	1.7 ± 0.8	4.1 ± 1.9	5.8 ± 2.6	5.0 ± 1.4	1.8 ± 0.5	6.7 ± 1.8
i3DHLK	2.5 ± 1.1	1.3 ± 1.4	3.9 ± 1.3	4.0 ± 2.03	0.7 ± 0.7	4.7 ± 2.5
pCS	6.4 ± 3.5	5.0 ± 2.2	11.4 ± 5.5	9.5 ± 4.7	14.6 ± 3.5	24.1 ± 7.4
p3DHL	7.8 ± 2.9	5.8 ± 1.6	13.6 ± 4.1	7.8 ± 2.1	19.1 ± 2.6	26.9 ± 4.5
p3DHLK	3.7 ± 1.5	4.0 ± 1.2	7.7 ± 0.5	8.5 ± 2.3	17.7 ± 3.2	26.1 ± 3.6

Table 3.10 Percentage of apoptotic, necrotic, and total cell death measured 24 h after 160 mM EtOH administration on Day 1. n ≥ 3 biological replicates for each condition.

	Untreated on Day 1			Administration on Day 1		
Model	**Apoptosis (%)**	**Necrosis (%)**	**Cell Death (%)**	**Apoptosis (%)**	**Necrosis (%)**	**Cell Death (%)**
iCS	5.9 ± 2.2	0.9 ± 0.5	6.7 ± 2.4	3.8 ± 1.4	1.4 ± 0.6	5.2 ± 1.9
i3DHL	2.7 ± 1.2	5.1 ± 1.7	7.8 ± 2.7	3.9 ± 3.2	5.2 ± 1.7	9.1 ± 1.6
i3DHLK	3.4 ± 1.9	2.1 ± 0.9	5.5 ± 2.9	3.5 ± 1.2	2.3 ± 0.9	5.8 ± 1.6
pCS	6.8 ± 3.5	3.4 ± 2.4	10.2 ± 4.5	13.3 ± 3.0	14.0 ± 1.0	27.3 ± 2.9
p3DHL	8.4 ± 2.9	4.0 ± 0.6	12.3 ± 3.2	17.0 ± 5.5	15.9 ± 4.2	32.9 ± 7.6
p3DHLK	3.6 ± 1.4	2.8 ± 0.6	6.8 ± 2.0	16.5 ± 5.0	24.8 ± 1.4	41.3 ± 4.3

Table 3.11 Percentage of apoptotic, necrotic, and total cell death measured in untreated samples on Days 7 and 14. n ≥ 3 biological replicates for each condition.

	Untreated on Day 7			Untreated on Day 14		
Model	**Apoptosis (%)**	**Necrosis (%)**	**Cell Death (%)**	**Apoptosis (%)**	**Necrosis (%)**	**Cell Death (%)**
iCS	2.6 ± 1.3	2.8 ± 1.4	5.4 ± 2.4	6.8 ± 2.5	5.6 ± 3.1	12.4 ± 5.6
i3DHL	4.4 ± 2.5	0.8 ± 0.8	5.2 ± 3.3	2.2 ± 1.7	1.7 ± 0.6	3.9 ± 1.7
i3DHLK	2.0 ± 0.1	0.5 ± 0.3	2.4 ± 0.4	5.0 ± 0.9	2.5 ± 0.5	7.5 ± 1.4
pCS	6.4 ± 3.5	5.0 ± 2.2	11.4 ± 5.5	9.5 ± 4.7	14.6 ± 3.5	24.1 ± 7.4
p3DHL	7.8 ± 2.9	5.8 ± 1.6	13.6 ± 4.1	7.8 ± 2.1	19.1 ± 2.6	26.9 ± 4.5
p3DHLK	3.7 ± 1.5	4.0 ± 1.2	7.7 ± 0.5	8.5 ± 2.3	17.7 ± 3.2	26.1 ± 3.6

Table 3.12 Percentage of apoptotic, necrotic, and total cell death measured 24 h after 0.36 μM RIF administration on Day 1. n ≥ 3 biological replicates for each condition.

	Untreated on Day 1			Administration on Day 1		
Model	**Apoptosis (%)**	**Necrosis (%)**	**Cell Death (%)**	**Apoptosis (%)**	**Necrosis (%)**	**Cell Death (%)**
iCS	6.6 ± 1.4	1.4 ± 0.6	8.0 ± 1.5	7.7 ± 4.0	2.7 ± 1.6	10.4 ± 5.6
i3DHL	7.0 ± 1.7	1.5 ± 0.2	8.5 ± 1.7	3.6 ± 1.8	2.5 ± 1.2	6.1 ± 3.0
i3DHLK	3.4 ± 1.2	1.8 ± 1.3	5.1 ± 2.4	5.2 ± 3.0	2.7 ± 1.4	7.9 ± 1.9
pCS	3.4 ± 2.3	0.7 ± 0.6	4.1 ± 2.0	5.7 ± 1.9	3.9 ± 2.8	9.6 ± 4.7
p3DHL	3.0 ± 2.0	2.8 ± 1.1	5.9 ± 2.9	9.2 ± 0.8	7.4 ± 0.9	16.5 ± 0.4
p3DHLK	4.1 ± 1.0	1.5 ± 1.3	5.6 ± 0.3	21.8 ± 2.6	19.3 ± 1.8	41.1 ± 1.2

Table 3.13 Percentage of apoptotic, necrotic, and total cell death measured in untreated samples on Days 7 and 14. n ≥ 3 biological replicates for each condition.

	Untreated on Day 7			Untreated on Day 14		
Model	**Apoptosis (%)**	**Necrosis (%)**	**Cell Death (%)**	**Apoptosis (%)**	**Necrosis (%)**	**Cell Death (%)**
iCS	5.1 ± 1.0	2.4 ± 0.6	7.5 ± 1.5	2.9 ± 1.1	4.0 ± 1.7	6.8 ± 2.7
i3DHL	5.1 ± 0.7	1.6 ± 0.5	6.7 ± 0.3	4.3 ± 1.0	3.2 ± 2.1	7.5 ± 2.2
i3DHLK	4.5 ± 0.8	2.2 ± 2.5	6.7 ± 2.7	4.0 ± 1.2	2.6 ± 1.0	6.6 ± 0.8
pCS	5.8 ± 2.7	0.8 ± 0.8	6.6 ± 2.7	4.3 ± 0.5	3.4 ± 1.8	7.7 ± 2.3
p3DHL	4.0 ± 1.1	4.4 ± 3.1	8.3 ± 2.8	6.7 ± 0.1	3.4 ± 1.10	10.1 ± 1.2
p3DHLK	6.5 ± 1.0	3.1 ± 1.7	9.6 ± 2.1	5.8 ± 0.8	3.5 ± 0.9	9.3 ± 0.2

Table 3.14 Albumin secretion in iHLC and PHH organoids/cultures and LSEC and KC monocultures on Days 1, 7, and 14. Culture medium values were subtracted from the raw data and then the concentration was normalized to the protein content in the organoid/culture at each time point (pg/ mg protein). n = 3 biological replicates.

Media/Culture	**pg/ mL**	**Day 1 (pg/ mg protein)**	**Day 7 (pg/ mg protein)**	**Day 14 (pg/ mg protein)**
iHLC Media	9169 ± 693			
PHH Media	7448 ± 117			
LSEC Monoculture		52.8 ± 91.41		
KC Monoculture		376.4 ± 651.9		
iCS		$17.4 \times 10^5 \pm 0.6 \times 10^5$	$19.9 \times 10^5 \pm 1.3 \times 10^5$	$13.1 \times 10^5 \pm 1.3 \times 10^5$
i3DHL		$31.7 \times 10^5 \pm 1.6 \times 10^5$	$35.2 \times 10^5 \pm 1.8 \times 10^5$	$30.9 \times 10^5 \pm 4.0 \times 10^5$
i3DHLK		$34.0 \times 10^5 \pm 0.1 \times 10^5$	$33.5 \times 10^5 \pm 1.2 \times 10^5$	$24.2 \times 10^5 \pm 9.1 \times 10^5$
pCS		$4.6 \times 10^5 \pm 0.7 \times 10^5$	$5.3 \times 10^5 \pm 3.0 \times 10^5$	$7.3 \times 10^5 \pm 2.5 \times 10^5$
p3DHL		$4.2 \times 10^5 \pm 0.6 \times 10^5$	$15.31 \times 10^5 \pm 1.57 \times 10^5$	$25.5 \times 10^5 \pm 1.6 \times 10^5$
p3DHLK		$4.6 \times 10^5 \pm 0.4 \times 10^5$	$16.7 \times 10^5 \pm 3.6 \times 10^5$	$23.9 \times 10^5 \pm 0.6 \times 10^5$

Chapter 4: Bovine Airway Models: Approaches for Investigating Bovine Respiratory Disease

*Chapter 4 reprinted with permission from N. Gandhi, T. J. Inzana, and P. Rajagopalan, Bovine Airway Models: Approaches for Investigating Bovine Respiratory Disease. ACS Infectious Diseases, 2023: **9, 6**, p. 1168-1179.*

4.1 Introduction

Bovine Respiratory Disease (BRD) is a multifactorial condition in which strains of bacteria, viruses, or both infect the cells of the upper respiratory tract of cattle (205-208). Common pathogens involved in BRD include *Mannheimia haemolytica*, *Histophilus somni*, *Pasteurella multocida*, *Mycoplasma bovis*, bovine respiratory syncytial virus (BRSV), and bovine viral diarrhea virus (BVDV), although other genera and species of bacteria and viruses have been shown to be implicated (208-210). The combined effects of these pathogens can cause severe disease or death within cattle populations, resulting in significant economic losses. In the United States (US) alone, the estimated cost of BRD is around $1-3 billion annually (211, 212) .

Antimicrobials or vaccines can be administered to protect livestock. However, with the escalation of BRD infections and the interplay between various species of invading pathogens, no treatment exists to provide complete protection for mitigation of the disease (213-215). Studies have shown that cattle susceptible to infection can be pre-treated with prophylactic antimicrobials, such as florfenicol and tilmicosin, to reduce morbidity and mortality (209, 216). However, concerns of antimicrobial-resistant bacteria have led to a debate over this method of treatment (209, 216). When antimicrobial-resistant bacteria proliferate, the severity of BRD increases, resulting in a more detrimental prognosis and faster spread of disease (207, 217). Nasopharyngeal swabs were taken from 68 cattle that died of BRD to screen for common pathogens of BRD including BVDV, BRSV, bovine herpes virus (BHV)-1, parainfluenza type 3 virus, *Mycoplasma bovis, M.*

haemolytica, *P. multocida*, and *H. somni*. PCR analysis detected the presence of antimicrobial-resistant *M. haemolytica*, *P. multocida*, and *H. somni*, all of which are major bacterial pathogens that contribute to BRD (218). Approximately 30% of the *M. haemolytica* and 12.5% of the *P. multocida* isolates from additional lung samples were resistant to at least seven antimicrobials. The isolates exhibited resistance to macrolides, a common class of antibiotics to treat BRD (218-220). In efforts to combat antimicrobial resistance in BRD pathogens, phytochemicals, metabolites found in plants, were assessed as an alternative to antibiotics (221). Out of seven phytochemicals studied, allyl isothiocyanate, cinnamaldehyde, eugenol, and benzyl isothiocyanate were the most effective at inhibiting growth of *H. somni*, *M. haemolytica*, and *P. multocida* (221, 222).

The sequence of infection by certain viruses and bacteria can determine a different outcome of BRD (208, 223, 224). For instance, initial infection by *H. somni* upregulates antiviral responses towards BRSV in *in vitro* epithelial cells (224). However, calves that are infected with BRSV first and then *H. somni* develop more severe disease (223). Although infection can be caused by many strains of bacteria and viruses, pre-disposing stress factors also play a role in the severity of infection (**Figure 4.1)**. Many cattle are subjected to crowding, especially during transportation (207-210). The proximity of cattle leads to easier spread of bacteria or viruses, which contributes to BRD (217). The stresses from weaning, prior infection, poor weather, and transport also provide an opportunity for pathogens to invade the lower respiratory tract of the host (210, 216, 220).

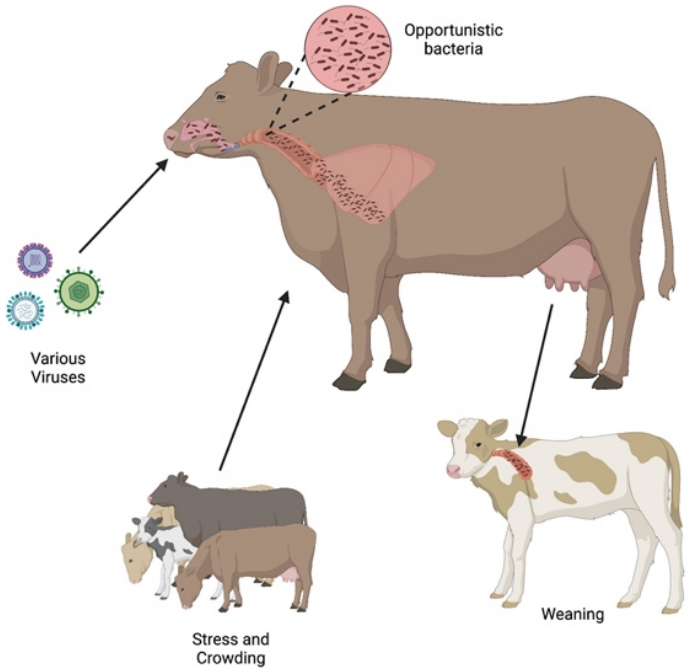

Figure 4.1 Bovine respiratory disease is caused by an array of factors. One method of pathogenesis is thought to occur through an initial viral infection, which causes opportunistic bacteria to enter and proliferate in the lower respiratory tract. Stress and crowding of cattle can encourage the infection to progress. Weaning can also result in infection of calves, spreading the infection among the livestock.

Currently, common *in vitro* culture models for the bovine respiratory system include submerged tissue cultures (STCs) and air-liquid interfaces (ALIs) (**Figure 4.2**) (225). Both culture systems have led to a better understanding of the mechanisms underlying bacterial and viral infections that contribute to the development of BRD. Although the ALI cultures can lead to differentiated cells, both systems start with only one cell type. However, STCs and ALIs do not fully recapitulate the environment of the respiratory tract. In order to illustrate the differences between current models and *in vivo* tissue structures, we first describe the respiratory tract, defense mechanisms, and the pathogens that lead to the multi-factorial complexity of BRD. Such information is vital not only to understand data obtained from current *in vitro* models but, more importantly, on how to refine and add to them in future studies. This review summarizes the current advancements of *in vitro* bovine airway cultures used to study BRD. Although these models have provided relevant information on BRD, there is a continued need for *in vitro* systems that emulate the respiratory

system even more closely. We recommend the need for 3D bovine airway organoids with architecture and cellular composition that mimic the bovine respiratory system. Such 3D models may provide even further insights into the complexities of disease progression and pathogenesis during infections that could further our understanding of BRD and aid in the design and development of therapeutics to treat cattle.

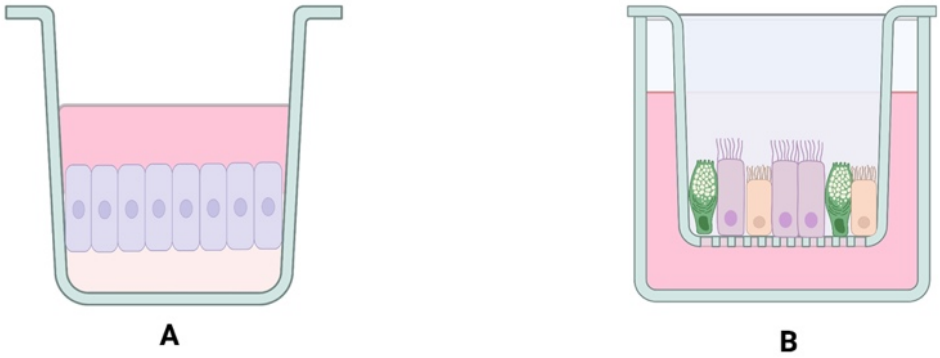

Figure 4.2 The two most common culture systems for respiratory models include the **(A)** submerged tissue system (STC) and **(B)** the air-liquid interface (ALI). The STC system only has one cell type, usually undifferentiated, submerged in media or supplement. The ALI is exposed on the apical surface to air, and fed through the basal compartment, allowing for differentiation to occur.

4.2 Anatomy and Defensive Mechanisms of the Bovine Respiratory System

The respiratory system is responsible for providing a barrier against pathogenic substances in the external environment, benefiting both physical and immunological functions (226-229). The bovine airway system can be divided into two regions: the upper respiratory tract, where air is filtered through the nasal cavities through the upper part of the larynx, and the lower respiratory tract, where air is subjected to gas exchange through the bronchi to the alveoli (230). The airway's luminal surface is lined with a layer of epithelial cells that serve primarily as a physical barrier against foreign particles (**Figure 4.3A**) (231). Invading particles and pathogens are blocked by tight junctions within the epithelium (227, 232-235). Furthermore, airway epithelial cells secrete

mucins that physically entrap invading pathogens (**Figure 4.3B**) (230, 235). Endothelial cells line the vasculature and constitute a barrier for the exchange of molecules as well as pathogens (236). Pulmonary endothelial capillaries clear toxic and vasoactive substances that can enter the respiratory circulation and enhance the disease (237). The endothelial cells are sensitive to small signaling molecules, including bradykinin, angiotensin I and II, neurotransmitters such as serotonin and dopamine, and prostaglandins (237). Without the clearance of substances and molecules initiated by a pathogen, pulmonary edema, emphysema, and pneumonia can result (237).

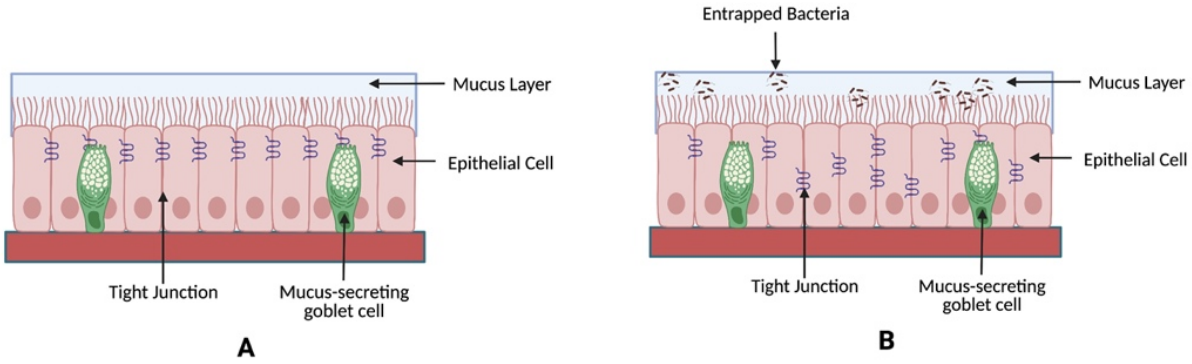

Figure 4.3 Two populations of cells within the bovine upper respiratory system include epithelial cells and mucus-secreting goblet cells; both cell types protect the host from pathogens and the outside environment. The epithelial cells construct a barrier through tight junctions and the **(A)** mucus-secreting goblet cells produce mucin, which **(B)** entraps bacteria.

Respiratory system infections, due to transcytosis, adherence, or secreted virulence factors by pathogens, can activate the immune system (209, 216, 238). Bacteria, such as *H. somni*, express immunoglobulin binding proteins (IgBP), which allow for the non-immune adherence of IgG to their cell surface(239). These gram-negative bacteria also have lipopolysaccharide (LPS) within their outer membrane, which is toxic, resulting in inflammation (240). The lipid A component of LPS (also known as endotoxin), attaches to the toll-like receptor (TLR)-4 on immune cells, such as macrophages and dendritic cells, initiating the innate immune response (**Figure 4.4**) (241, 242). From there, pro-inflammatory cytokines such as IFN-γ and TNF-α are released (243-245).

Neutrophils are then recruited to phagocytize the bacteria (246-248). However, secreted molecules from bacteria, such as IgBPs, protect against complement protein binding, which activates the immune system to target and clear the pathogen (239). These proteins also decrease phagocytosis of the bacteria by immune cells (239).

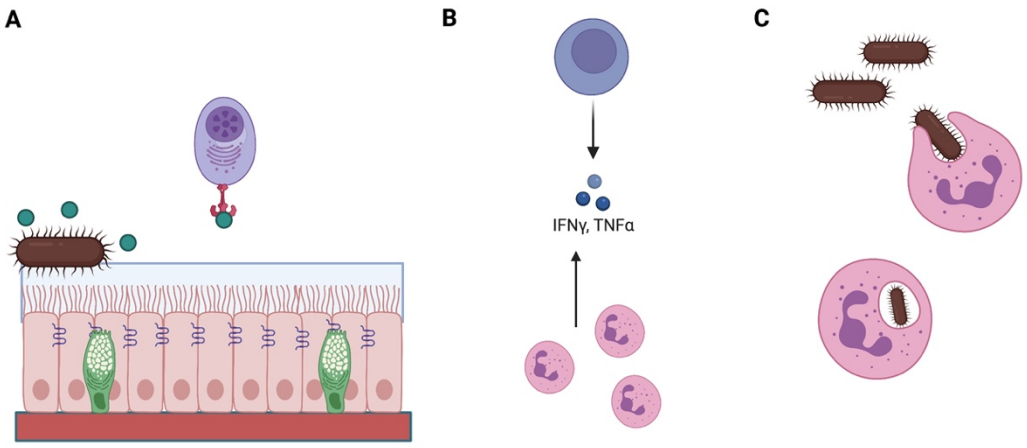

Figure 4.4 Immune response to bacterial infection. **(A)** Gram-negative bacteria have lipopolysaccharide (LPS) or endotoxin in their outer membrane, which can be released into the circulation. The lipid component of the endotoxin attaches to toll-like receptor 4 on the surface of immune cells. **(B)** Cytokines, such as IFN-y and TNF-α, are then released by host cells. These cytokines recruit neutrophils to the site of infection. **(C)** Neutrophils phagocytize and try to kill the invading bacteria.

4.2.1 Mucins and Ciliated Cells

The mucociliary escalator is the primary defense mechanism that physically entraps and removes pathogens attempting to invade the respiratory system (**Figure 4.3B**) (249). The airway is lined with ciliated cells that produce mucins, which form a gel-like layer where soluble particles are trapped before entering the cells beneath them (235, 250). Goblet cells secrete mucins as a first line defense mechanism in proximal and distal airways. When an infection occurs, mucus production increases (235, 251). In the human airway system, MUC5AC and MUC5B are the primary defense mucins (252). The roles of MUC5AC and MUC5B have been investigated in mice as well (253, 254). Specifically, MUC5B was found to be predominant, and plays the major role

in clearance of pathogens (253). When this gene is knocked out, increased inflammation occurs (254).

Human mucins are orthologs of those found in *Bos taurus*, serving as an initial point of investigation for the effect of mucins during BRD infections. Bovine mucins have been investigated in some depth. Boukahil and Czuprynski reported the use of various concentrations of mucin from a bovine submaxillary gland to study biofilm formation by *M. haemolytica* (255). Results showed that incorporating 1 mg/mL of mucin led to less biofilm formation (255). Cozens et. al. reported the detection of MUC5AC from differentiated bovine epithelial cells in an ALI culture (225). Thus, studying mucins with respect to bovine cells and the respiratory tract remains an area of interest in the investigation of biofilm formation in the future.

Ciliated cells are differentiated epithelial cells that are interspersed between the goblet cells (**Figure 4.3A**) (252). These cells extend to the bronchioles of the respiratory tract. The cilia are composed of dyneins and motor proteins that provide force to expel the pathogens upwards, known as ciliary beating, that are subsequently released by coughing (252). The tips of the cilia, lining the apical membrane, are coated by the periciliary layer, which is a low viscosity, glycolipid-rich fluid underneath the mucus layer that promotes ciliary beating (256). Currently, the ALI models incorporate ciliated cells through differentiation protocols of the epithelial layer (257-259). However, the specific characteristics of the bovine mucociliary escalator may require additional investigation before *in vitro* cultures can mimic the structure and cellular phenotypes found *in vivo*.

4.2.2 Tight Junction Barriers

Epithelial cells express tight junction proteins that prevent particles or pathogens from invading underlying tissues (260, 261). This barrier is present on the apical side of the membrane and prevents the flow of solutes and ions in between cells (260). When bacteria or viruses come in

contact with the epithelium, the tight junctions can be disrupted, resulting in inflammation, edema, and even death (261). In humans, a common feature of acute respiratory disease, asthma, and chronic obstructive pulmonary disease includes the disruption of the epithelial tight junction barrier (261). Similar clinical signs arise due to bacterial and viral infection in BRD, where pathogens specifically target these proteins (257).

4.2.3 Antimicrobial Peptides

Antimicrobial peptides (AMPs) are short amino acid chains that are part of the innate immune system (262). Most commonly, these peptides exhibit a net positive charge, which can aid in the disruption of negatively charged bacterial cell membranes (262). AMPs inhibit viruses by specifically interfering within their replication cycle and directly interacting with the virions (262).

Diamond et. al. initially reported the identification of tracheal antimicrobial peptide (TAP), a member of the β-defensin family obtained from the bovine mucosa. TAP has been shown to exhibit antimicrobial activity against *in vitro* cultures of *Escherichia coli*, *Staphylococcus aureus*, *Klebsiella pneumonia*, and *Pseudomonas aeruginosa* (263). TAP-expressing transgenic mice were able to produce this peptide within mammary glands, which could then be extracted and utilized to inhibit the growth of *E. coli*, (264).

The bactericidal effects of synthetic TAP were also investigated with bacterial isolates responsible for BRD, including *M. haemolytica*, *H. somni*, *P. multocida*, and *M. bovis* (265). TAP exhibited antibacterial effects on *M. haemolytica*, *H. somni*, and *P. multocida* with a minimum inhibitory concentration (MIC) of up to 5 μg/ mL (265). However, *M. bovis* was not susceptible to TAP even when 300 μg/ mL was administered (265). A non-synonymous single nucleotide peptide (A137G) was sequenced from Exon 2 of the TAP gene in 23 cattle (265). A synthetic peptide was then

tested with both wild type and mutant *M. haemolytica* (265). The results revealed bactericidal effects, indicating that this bacterium was susceptible to this SNP in the TAP (265).

TAP production is inhibited by glucocorticoids, which are secreted upon stress conditions, and viral infection (266, 267). However, TAP expression is activated by LPS, Pam3CSK4, a toll-like receptor agonist that increases production of pro-inflammatory cytokines, and IL-17a, which activates immune cells (266, 268). The upregulated expression of TAP was confirmed in bovine tracheal epithelial cells (266). Western blot analysis indicated that LPS, Pam3CSK4m and IL-17a induced the nuclear factor kappa light chain enhancer of activated B cells (NF-κB) pathway, indicating that this is one mechanism for the expression of TAP (266). Another study showed through RT-PCR measurements that BVDV type 2 inhibited TAP expression in bovine tracheal epithelial cells via LPS induction (269).

Cattle infected with aerosolized *M. haemolytica* were treated with TAP or water (control) at 20 min, 2-, and 6-hrs post infection (hpi) (270). However, the administration of TAP did not improve pneumonia in these cattle (270). There were no significant differences between TAP treatment and water (270). The bactericidal activities of 6.25 μg/ mL and 12.5 μg/ mL TAP were investigated with *M. haemolytica* seeded at 2 x 10^4 CFU/ mL (270). Increasing concentrations of sodium chloride (up to 200 mM) and bovine serum (up to 2.5%) were administered and resulted in significantly greater numbers of surviving bacteria compared to controls (no sodium chloride or bovine serum), explaining a potential reason as to the lack of TAP activity *in vivo* (270).

Epithelial cells and neutrophils express cathelicidins, another class of AMPs (271, 272). Baumann et. al. reported that seven of these AMPs, including bactenecin 1 (Bac1), Bac5, bovine myeloid antimicrobial peptide (BMAMP)-27, -28, and -34, and indolicidin, were identified in bovine granulocytes. The study concluded that BMAMP was most effective at inhibiting growth of *S.*

aureus, *Streptococcus uberis*, and *E. coli* (272). However, investigation of these peptides in response to BRD-specific bacteria or their presence in the respiratory tract was not conducted.

4.3 Pathogens Involved in BRD

4.3.1 Bacteria Implicated in BRD

4.3.1.1 *Mannheimia haemolytica*: *M. haemolytica* is a member of the family *Pasteurellaceae* and is often the most common bacterial agent isolated from cases of BRD worldwide (211-214, 217, 243, 244, 255, 273-280). The A2 serotype of this gram-negative bacterium colonizes the upper respiratory tract of healthy cattle and maintains a commensal relationship with the host cells (207, 208, 214). However, through mechanisms unknown, but hypothesized to result from crowding, stress, and/or viral infection, the presence of the A2 serotype diminishes and is replaced with the A1 serotype, which proliferates and can invade the lower respiratory tract (207, 214). A common feature of *M. haemolytica* infection in cattle is pneumonia. Isolates obtained from cattle with pneumonia have shown the presence of multiple serotypes of *M. haemolytica*, most commonly A1, but also A6, A7, A9, and A11 (281).

4.3.1.2 *Histophilus somni*: *H. somni* is a gram-negative bacterium and also a member of the *Pasteurellaceae* family (208, 282, 283). *H. somni* can be implicated in BRD, but also plays a role in several other systemic diseases, such as thrombotic meningoencephalitis, myocarditis, polysynovitis, mastitis, otitis media, and reproductive failure (207, 208, 284). Post-mortem investigation of BRD caused specifically by *H. somni* has demonstrated the presence of pleuritis, and inflammation of tissues in the chest cavity, and separation of lungs from the chest wall (208, 216). This separation leads to edema and increased IgE production (223, 224). Typically, an IgE response occurs against parasites and allergens, although it has been detected in the BRD complex with pathogens such as *H. somni* and BRSV (223, 245). The released IgE antibodies

attach to mast cells, which then cause the secretion of pro-inflammatory cytokines such as TNF-α and IFN-γ (245). The production of IgE, specifically caused by *H. somni*, has been reported in up to 40% of pneumonic lungs in cattle (208, 285). The production of IgE was also noted in cattle vaccinated with a commercial *H. somni* bacterin vaccine (286).

4.3.1.3 *Pasteurella multocida*: *P. multocida* is a gram-negative bacterium of the family *Pasteurellaceae* and has been isolated from the upper respiratory tract of healthy and diseased cattle (207, 208, 282, 287, 288). Post-mortem analysis of the respiratory systems of cattle infected with *P. multocida* has demonstrated the presence of bronchopneumonia, lesions infiltrated with neutrophils, and abundant fibrin deposition (208, 216). There are five capsule serotypes of *P. multocida* (A, B, D, E, and F), but most BRD isolates are of type A (207, 208, 287, 289).

4.3.1.4 *Mycoplasma bovis*: Infections due to *M. bovis* are one of the leading causes of disease in calves, rather than adult cattle (207, 290-292). This bacterium infiltrates the mammary glands and becomes aerosolized in the feeding process, explaining its prevalence in calves (208, 293). When the calves become stressed due to crowding, the bacteria spread more easily between them. *M. bovis* can be found in calves within one day to one week after crowding (207, 291, 293). Clinical signs of *M. bovis* include pneumonia, mastitis, otitis media, and infertility (292, 294, 295).

4.3.2 Viruses Implicated in BRD

4.3.2.1 Bovine Respiratory Syncytial Virus (BRSV): BRSV affects both upper and lower respiratory tracts. This virus has been isolated in countries worldwide, most commonly in the United Kingdom (UK) and the US, where outbreaks occur quickly amongst herds (296, 297). BRSV infections result in clinical signs that mimic pneumonia, such as nasal discharge, lung lesions, and epithelial necrosis (297, 298). The severity of this infection can increase if the animal becomes co-infected with bacteria such as *M. haemolytica* and *H. somni* (223, 255). BRSV-

infected epithelial cells showed the upregulation of reactive oxygen species (ROS) gene expression as determined by qPCR, potentially suggesting that BRSV leads to oxygen damage (299).

4.3.2.2 Bovine Viral Diarrhea Virus (BVDV): BVDV can contribute to BRD through immunosuppression and persistent infection (300). Not only is BVDV a factor in BRD, but it can be implicated in infections of the immune and gastrointestinal systems (301, 302). BVDV in BRD-infected cattle can be cytopathic and/or non-cytopathic (300, 302). Persistent infection may result when the calf is infected in the first 40-120 days of gestation (303). A calf with non-cytopathic BVDV is immunotolerant but can be a source of infection to other animals (300, 303). However, a non-cytopathic strain can mutate to a cytopathic strain. When both strains are present, mucosal disease can result after one to two weeks of clinical signs (215, 304).

4.3.2.3 Bovine Herpes Virus 1 (BHV-1): BHV-1 is also implicated in BRD (280). Like other Herpes viruses, BHV-1 maintains its presence throughout the host's lifespan and can be passed onto calves (305). Downstream effects of infection include upregulation of genes involved in responding to reactive oxygen species (ROS) (306). BHV-1 is also known to cause reproductive tract disease in infected cattle, resulting in infertility, miscarriages, and stillbirths (307) (308). Clinical signs of BHV-1 include a high fever, inflamed nares, and excessive nasal discharge (308).

4.3.2.4 Bovine Parainfluenza-3 Virus (BPIV-3): BPIV-3 was one of the first viruses implicated in BRD, based on two reports in 1959 (309-311). The pathophysiology of BPIV-3 includes immunosuppression and damage to the respiratory tract (312, 313). BPIV-3 has been found in various cell types in the respiratory tract including tracheal cells, ciliated and non-ciliated cells, epithelial cells, and Type I and Type II pneumocytes (313).

4.4 Bacterial Biofilms

Bacteria often form biofilms on top of infected cells in the respiratory tract (283, 314, 315). By the time chronic infection of BRD is detected, a biofilm may have already formed (255, 282). Bacteria form organized colonies by attaching to host cells where they form an extracellular polymeric substance consisting of polysaccharides, nucleic acids, and various proteins (273, 274, 283, 316). The bacterial biofilm acts as a protective mechanism against the host's immune response and enhances resistance to antimicrobial agents (273, 274). The close contact of bacteria and cells within biofilms creates a boundary against disruptive agents, such as the immune response or the exogenous administration of antimicrobials (255, 279). BRD agents that have been shown to form individual and polymicrobial biofilms *in vitro* or *in vivo* include *H. somni*, *M. haemolytica*, and *P. multocida* (273, 274, 282, 283, 314).

H. somni biofilms have been investigated *in vitro* to understand their potential contribution to BRD (283, 314, 316). The formation of *H. somni* biofilms could also contribute to the colonization of other bacterial pathogens, such as *P. multocida*, in the BRD complex (282). *P. multocida* isolates that do not form a substantial biofilm on their own have been shown to be incorporated in *H. somni* biofilms (282). The biomass of both genera of bacteria increased throughout the 48-hr time period by 5-fold for *H. somni* and 12-fold for *P. multocida* (282). Approximately 69% of *P. multocida* integrated in the polymicrobial biofilm and contributed to 39% of the total biomass (282).

Sandal et. al. compared biofilm formation in pathogenic and commensal strains of *H. somni* (283). The biofilms were investigated at four stages including attachment, growth, maturation, and detachment (283). During the maturation stage, the biomass of the pathogenic biofilm was 8.4-fold higher than the commensal biofilm (283). Pathogenic *H. somni* also forms a thicker biofilm (up to 10-fold higher) compared to a commensal strain, which lacks many of the virulence factors

of disease isolates (283, 317). The differences in the biofilm formed by the two strains of *H. somni* may correlate to pathogenicity of this bacterium *in vivo* (283). Therefore, the formation and effects of polymicrobial biofilms and their effects on bovine cells is an important aspect of studies on BRD.

4.5 *In Vitro* Respiratory System Models

4.5.1 Submerged Tissue Cultures (STCs)

STCs have been utilized frequently to study various bacterial infections in airway cells (213, 224, 255, 276, 278, 280, 299, 318, 319). Cells are initially seeded onto a well-plate or in a flask and covered with medium. The cells are then allowed to reach confluency (213, 224, 255, 276, 278, 280, 299, 318, 319). Thereafter, bacteria or concentrated cultured supernatant (CCS) obtained from microbial cultures can be administered to investigate bacterial adherence to cells and signaling factors from pathogens, respectively, that may alter the characteristic of mammalian cells (224, 280). Such studies have even investigated multi-infection in bovine epithelial cells including pathogens such as BHV-1, BRSV, *M. haemolytica*, and *H. somni*.

The effect of mucins, co-infection by viruses, antibiotic resistance, and antibodies to surface proteins were conducted on an *M. haemolytica* biofilm formation on top of bovine epithelial cells in a STC (255, 276). The addition of mucin had a protective effect over the epithelial cells by preventing the overpopulation of bacteria (255). The formation of a *M. haemolytica* biofilm was not affected by either BRSV or BVDV infections. In this report , infection of the bovine epithelial cells by the two viruses occurred prior to seeding of bacterial cells (255). It is possible that the order of initial viral infection followed by bacterial proliferation is an important factor. Antibiotic resistance caused by biofilm formation was elevated, requiring higher doses to kill the bacterial cells (255). The antibiotics investigated in this study included florfenicol, erythromycin,

tulathromycin, gentamycin, and chlortetracycline. At least two surface proteins, OmpA and Lipoprotein 1, which are expressed on *M. haemolytica*, were found to bind to bovine epithelial cells (274, 276). Antibodies to these two surface markers resulted in the inhibition of *M. haemolytica* binding to bovine epithelial cells, leading to a reduction in biofilm formation (276).

Biofilm formation by *M. haemolytica* and *P. multocida* on bovine epithelial cells in an STC was also studied to investigate co-infection by two different bacterial strains (273). Results showed that *P. multocida* inhibited biofilm formation by *M. haemolytica*, which was confirmed through qPCR. The authors attribute this decrease of *M. haemolytica* to the lack of soluble factors that would be present *in vivo*. However, this system could provide a basis for understanding co-infection (273). Another study on polymicrobial biofilm formation included *H. somni* and *P. multocida*. Encapsulated *P. multocida* by itself did not form a prominent biofilm, but *P. multocida* could be incorporated into the *H. somni* biofilm. Interestingly, RNA-Seq measurements revealed that *P. multocida* genes, such as *fur* and *exbB,* which are involved in iron acquisition, were upregulated in the polymicrobial biofilm (282). Bacterial infection is known to upregulate expression of bacterial iron binding proteins, which are required to obtain this element from the host *in vivo* (320).

Zekarias et. al. investigated how *H. somni*, the CCS of this strain, and the immunoglobulin binding protein A (IbpA) producing DR2/Fic cytoxin affected bovine epithelial type 2 (BAT2) cells seeded in a monolayer(319). After these treatments, BAT2 cells became rounded and retracted(319). A Western blot measurement confirmed that IbpA was present and caused ~35-90% cytotoxicity in the cell cultures(319). *H. somni*, inoculated at an MOI of 50 for 1.5 hrs attached to BAT2 and bovine epithelial cells(319). Upon immunostaining, the BAT2 cells exhibited DR2/Fic antigen on the cell surfaces of nonpermeabilized cells when bacteria were inoculated(319). However, high expression of DR2/Fic was expressed within the cytoplasm of retracting cells upon all three

conditions(319). A transmigration assay conducted with BAT2 cells seeded on a Transwell® insert exhibited *H. somni* invading the epithelial barrier between retracted cells, which was attributed to paracellular migration(319).

Submerged epithelial cells secrete chemokines and cytokines as a response to bacterial culture medium (224, 255, 280). Pro-inflammatory cytokines such as IL-1, IL-1β, IL-8, IL-12, IFN-γ and TNF-α have been secreted in the presence of *P. multocida, M. haemolytica*, and *H. somni* (213, 223, 275). CXCL2, a chemokine that signals pro-inflammatory responses, was significantly upregulated as a result of BHV-1 and *M. haemolytica* co-infection (278, 321). Studies have shown interferons play a primary role in the immune response and are expressed as a result of infection of bovine epithelial cells. Specifically, the expression of IFN-1 and IFN-γ, has been reported to be greater in response to BVDV, BRSV, and BHV-1 (301, 318, 322).

Lin et al. employed STCs to study the effects of *H. somni* and BRSV infection on bovine airway cells to investigate how two pathogens can impact protein expression (224). A Western blot showed that *H. somni* can increase Viperin, a virus inhibitory protein, and ISG15, a ubiquitin-like modifier. Microarray analysis showed that when CCS from *H. somni* cultures was administered, it caused an approximate 200-fold and a 180-fold increase in the mRNA of ISG15 and Viperin, respectively. The fold-increase was determined by comparing the samples to controls treated with standard culture medium. The authors suggest that an endotoxin released by *H. somni* was responsible for the increase in Viperin expression. However, the microarray analysis also revealed that dual infection with BRSV and CCS from *H. somni* did not cause more than a 10-fold increase of ISG15 and Viperin mRNA. If *H. somni* is present prior to the BRSV infection, the results suggest that this bacterium could exert a protective role against BRSV (224). However, infection by BRSV alone or followed by CCS did not increase the expression of antiviral proteins (224).

The contribution of leukocytes recruited to the site of infection in BRD has been further investigated in STCs. Medium obtained from epithelial cells infected by BHV-1 that were also exposed to the *M. haemolytica* leukotoxin was used to culture bovine leukocytes. The release of pro-inflammatory cytokines (IL-1, IL-8, and TNF-α) from epithelial cells as a result of BHV-1 infection recruited leukocytes, thereby amplifying inflammation (280). The inflammatory cytokines that were responsible for leukotoxin binding from *M. haemolytica* were stimulated by lymphocyte function-associated antigen 1 in bovine blood mononuclear cells (244, 277). From there, the *M. haemolytica* leukotoxin bound to integrins (CD11a and CD18) on bovine leukocytes and induced apoptosis or necrosis (280).

4.5.2 Air-Liquid Interfaces

As an improvement to studying BRD infections in *in vivo* cultures, work has been done to design air-liquid interfaces (ALIs), representing the physiological environment that surrounds epithelial cells in the airway (323). ALIs are commonly used to model the human respiratory system (323-325). These models can be used to study respiratory diseases and infections that lead to proliferation, differentiation, inflammation, and immunological responses specific to the airway system (325-328). ALI models are typically assembled on Transwell® plates, where the apical medium is removed from the culture after confluency and establishment of the epithelial barrier has been achieved, allowing cells to receive medium from the basolateral compartment only. This method prevents competition for nutrients among the pathogens and cells, diminishing toxins or byproducts that are secreted by each individual cell type (225, 258, 327). A differentiated epithelium is generated by exposure to the ALI with the addition of growth supplements in the culture media, such as retinoic acid, epidermal growth factor, insulin, and hydrocortisone (225, 257). Polarization and differentiation of epithelial cells results in ciliated and goblet cells (258, 327).

ALI models using bovine epithelial cells are emerging (225, 329). The period for full differentiation of the bovine epithelial cells in an ALI was found to range from 14 to 42 days (214, 225, 257, 329). After this period, cells exhibited cilia on their surfaces, representing one of the defense mechanisms seen in the pseudostratified epithelial layer in the respiratory tract (231). Fluorescent immunohistochemistry of the cultures showed differentiation of epithelial cells to basal, goblet, and ciliated cells. (225, 257). A feature of ALI systems includes the formation of tight junctions (257, 329). Immunostaining for zonula occuldens-1 (ZO-1) showed the presence of tight junctions throughout the differentiation process, resulting in a barrier against pathogens (329).

In an extensive study done by Cozens et al., exogenous growth factors were added to optimize the differentiation of bovine airway epithelial cells. Certain epidermal growth factors increased proliferation in ALI cultures, similar to human models (330, 331). Increased ciliation and cellular differentiation into mucus-producing cells were attributed to the addition of retinoic acid (329, 330, 332). Triiodothyronine (T3), which regulates mucus production in humans, was shown to not affect mucus production in bovine cells grown in a ALI model (333). Mucin production by these bovine ALI models was visualized using Jacalin-labeling, which is a lectin that specifically binds to the O-glycoproteins that make up mucin (225, 334).

In the investigation of *M. haemolytica,* Cozens et. al. examined the effects of the A1 and A2 serotypes of this bacterium for 5 days after differentiation of epithelial cells at an ALI (214). Unlike the A2 serotype, the pathogenic A1 serotype was responsible for infection in these models, with disruption of ZO-1 20 hpi. Disruption of tight junction barriers was also measured in the ALI by trans-epithelial electrical resistance (TEER) (214). There was a significant reduction in TEER between 16 to 48 hpi (214). IL-1β release for A1 serotype infection was approximately 3-fold higher at 6 hpi compared to infection caused by the A2 serotype (214). Similarly, TNF-α release

was approximately 4-fold higher at 20 hpi in infections caused by the A1 serotype compared to the A2 serotype (214). Scanning electron microscopy was used to visualize bacterial infiltration by transcytosis and showed that *M. haemolytica* specifically targeted non-ciliated epithelial cells in an ALI (214). Taken together, the ALI model provides an explanation for some infection mechanisms (214).

Su et. al. examined *P. multocida* infection in bovine epithelial cultures using an ALI model. They reported the proliferation of bacterial cells for up to 24 hpi (335). In this study, bacteria were inoculated onto the epithelial cell cultures at 10^5 CFU and incubated for four hrs, followed by rinsing of the cultures to remove any non-adherent bacteria (335). The cells at the ALI with this inoculation density maintained their barrier function for up to 24 hpi, indicated by no changes in TEER values throughout the culture period (335). A decrease in barrier function was only seen in infected cultures longer than 24 hpi (335). The authors attributed this finding to the commensal relationship between *P. multocida* and the bovine airway system, where this bacterial strain may only become pathogenic when allowed to proliferate (335). In addition, at this inoculation density, cilia coverage of the ALI at 24 hpi was significantly lower than in the control cultures with no bacteria (335). The authors concluded that this observation could be due to the lack of mucus-clearing in the ALI model compared to *in vivo* (335).

Two studies examined the susceptibility of bovine epithelial cells to BRD-related viruses using differentiated airway epithelial cells cultured at an ALI and precision-cut lung slices (PCLS). In PCLS the tissue was harvested from the animal (259, 336). Both studies showed that BPIV-3 only infected ciliated cells at the apical membrane in the ALI model and in PCLS. The study conducted by Kirchhoff et al. also examined the effects of BHV-1 on the two models. Apical differentiated and ciliated epithelial cells were resistant to infection by BHV-1. For BHV-1 to infect the epithelial cells, the tight junctions on the basal side had to be disrupted by either calcium depletion or

mechanical injuring (259). The PCLS model also exhibited BHV-1 infected cells only on their basal surfaces (259). These findings suggest that BHV-1 targets the basal side of cells, where the epithelium is undifferentiated. Both studies showed that BRSV inefficiently infected cells in the ALI model and PCLS. Goris et. al. reported that a multiplicity of infection of 3.5 was needed to infect ALI cells (336). Kirchhoff et. al reported that BRSV targeted subepithelial cells and resulted in infection up to 600-fold lower than infection caused by BPIV-3 (259). The authors concluded that viral infection preferentially targets cells based on phenotype. BPIV-3 and BRSV infected differentiated epithelial cells on the apical side, whereas BHV-1 infected epithelial cells on the basal side (259, 336). Goris et. al. postulated that BRSV did not target epithelial cells due to a lack of surface receptors (336). Since BRD is a multi-factorial condition, an initial bacterial infection could upregulate viral receptors (259). However, experiments in both studies were not conducted with bacterial and viral co-infection, but the potential for such investigations in the future was discussed (259).

4.6 Future Work

Although the ALI models clearly demonstrate differentiation of the epithelium similar to the structure *in vivo*, most studies on BRD bacterial biofilm formation have been conducted in two-dimensional (2D) cultures (213, 224, 280, 337). The respiratory system is a highly vascularized, complex system, in which multiple cell types contribute to architecture and function (252, 333, 338). For instance, multicellular human ALI models, including epithelial cells, endothelial cells, macrophages, and dendritic cells, have been developed to understand cell-cell interactions that more accurately represent respiratory architecture (339). Therefore, the addition of endothelial cells to epithelial cell culture systems could provide further insight into understanding the cellular mechanisms and signaling that occur during an infection. In addition, a 3D multi-cellular model could serve as a platform to study such diseases (340). Such cultures may better recapitulate the

in vivo environment and provide the desired structural complexity to better understand the progression of BRD (340, 341).

Limited research has been done with bovine endothelial cells (294). One study investigated drug delivery in cattle by using endothelial cells in an *in vitro* model (342). However, this study only focused on the carcinogenic effects and the life span of endothelial cells, rather than the effects of infection by a virus or bacterium (342). Bovine endothelial cell work has predominately been conducted for understanding diseased cardiac tissue or reproductive tracts (236, 343-346). For example, pulmonary vascular endothelial cells were used to investigate the effects of LPS on vascular thrombosis after *Pasteurella haemolytica* infection (345, 346). Another study showed that *P. haemolytica* infection on confluent monolayers of pulmonary artery endothelial cells with neutrophils had a protective effect, which was exhibited by lower levels of LPS (347). Additionally, adenomyosis, a condition that can lead to uterine dysfunction, was investigated in endothelial cells sourced from bovine uteri (343). These cells were used to evaluate gene and protein expression of vascular endothelial growth factor (VEGF) to study the underlying mechanism (343). Although these studies were not conducted in relevance to BRD, they showcase the importance of investigating other cell types that could be advantageous in furthering our understanding of this disease.

Lee et al. reported a co-culture model of bovine airway endothelial cells with two immortalized epithelial cell lines (BATII and B2AE) cultured for 14 days using Transwell® filters to emulate an ALI model (348). This study presents the potential for studying invading pathogens in the context of BRD by providing a protocol for assembling a co-culture model at an ALI that is representative of the bovine respiratory system. Characterization of this model included analysis techniques such as immunostaining to distinguish epithelial and endothelial cells, H&E staining for morphology, and TEER measurements for disruption of tight junctions. However, infection with bacteria or

viruses was not conducted(348). The importance of studying bacterial and viral infections in a co-culture model would allow for a more. holistic understanding of BRD. For instance, *H. somni* has been reported to induce apoptosis of endothelial cells (284, 316). Studies involving *H. somni* have been conducted on epithelial cells, but the inclusion of other cell types could provide a more comprehensive understanding (213, 224).

Human airway organoids have been developed for more accurate *in vitro* disease modeling studies (246, 349-351). In fact, a loss of lung architecture can promote disease *in vivo*, thus highlighting an imperative need for a 3D model that can be used for *in vitro* investigations (351). For example, organoids have been assembled by deriving cells from patients with cystic fibrosis and lung cancer biopsies and resections (246). The organoids are comprised of differentiated epithelial cells, including basal, secretory, and ciliated cells (246). The generation of these organoids has enabled further understanding of the pathogenesis of various diseases and mechanisms of bacteria and viruses (349, 350). For example, human airway organoids including club, ciliated, and alveolar type-2 cells infected with SARS-CoV-2 were used to develop a physiological model for investigating infectivity (352). Another study developed human airway organoids to study the interaction of mycobacteria with respiratory epithelial cells. In *Mycobacterium tuberculosis* infected epithelial cells, RT-qPCR measurements showed a significant upregulation of genes encoding an antimicrobial peptide, β-defensin 1, and IL-8, a cytokine (353). These reports underscore the potential for 3D multi-cellular bovine airway organoids to investigate BRD, specifically, to unearth defense mechanisms and pathways. Since BRD is multi-factorial, co-infections of pathogens should be investigated as well to study the interplay between different genera of bacteria and strains of viruses that are prominent in this disease. Such systems could provide a comprehensive understanding of the underlying mechanisms of infection and, therefore, the development of future treatments.

4.7 Discussion and Conclusion

While the STC and ALI models have the potential to provide valuable insight into bovine epithelial cell behavior, there are still limitations with these models. The STCs allows for direct pathogenic effects to be investigated and are easier to assemble (224, 278, 280). However, the epithelial barrier is highly dynamic, involving differentiation into polarized cells (324). The STC models do not accurately represent physiological conditions due to the lack of 3D architecture and the pseudostratified epithelial layer (354). *In vivo,* cells interact with mucus or synergistic bacteria, which are not represented when the cells are submerged in medium (225, 258, 327).

ALIs have been used to represent the *in vivo* architecture and environmental conditions surrounding cells in the respiratory tract (327, 339, 355). Multiple pathogenic effects of the BRD complex have the potential to be studied on differentiated bovine epithelial cells at the ALI. Although the ALI models can provide more detail of the interactions that occur between cells and surrounding gases, optimal environmental conditions, polymicrobial and bovine cell co-cultures still need to be investigated (225). Additionally, differentiating cells in an ALI can take up to 42 days, which is time intensive (327, 339, 355).

In conclusion, the need for an accurate 3D organoid that better represents the architecture of the bovine respiratory tract can advance understanding of BRD and provide a platform to study this disease and to develop therapeutics. A 3D organoid with the inclusion of other cell types, incorporation of respiratory defense mechanisms, and the development of biomaterials to mimic the bovine extracellular matrix can better recapitulate the respiratory system. Such organoids could be assembled more efficiently in shorter time periods which could further guide understanding of BRD. Co- or multi-infection of the models can be conducted to study the effects and interplay of pathogens. Thus, future work can advance knowledge of the detrimental effects

this multi-factorial disease causes in cattle and provide a basis for comprehensive therapeutic development.

Chapter 5: Infection of a Novel 3D Bovine Airway Model with *Histophilus somni*

Gandhi, N., Subhadra, B., Cao, D., Inzana, T.J., and Rajagopalan, P, Infection of a Novel 3D Bovine Airway Model with Histophilus somni. In preparation.

In **Chapter 4**, we have motivated the need for a 3D multicellular bovine airway model to study BRD and develop antimicrobials for treatment. Here, we report the assembly of a 3D multicellular bovine airway organoid composed of bovine epithelial and endothelial cells. We first administered the concentrated culture supernatant (CCS) from *H. somni* to understand how infectious particles might affect the cells in the organoid prior to inoculation of bacteria to investigate infection. Our goal was to design a model that is representative of the architecture of the bovine airway system that can be assembled systematically as a platform for BRD-related studies. The widespread use of these models may help better guide the testing and development of antimicrobials to combat BRD.

5.1 Materials and Methods

Phosphate buffered saline (PBS), sodium bicarbonate ($NaHCO_3$), Triton-X, and bovine serum albumin (BSA) were obtained from Thermo Fisher Scientific (Waltham, MA). Glutaraldehyde, sodium dodecyl sulfate (SDS), and collagenase were purchased from Millipore Sigma (St. Louis, MO).

5.1.1 Extraction of Collagen

Collagen was extracted from rat tails using previously described protocols (7, 12, 14, 15, 17). Briefly, tendons were extracted then dissolved in acetic acid before centrifugation at 13,000 x g. A 30% (w/v) sodium chloride solution was then added slowly to the supernatant and centrifuged

at 8500 x g. The collagen solution was then dialyzed in 1 mN hydrochloric acid. The solution was then sterilized with chloroform and used at a final concentration of 1.1 mg/ mL with a pH of 3.1 (7, 12, 14, 15, 17).

5.1.2 Assembly of Bovine Epithelial Monocultures

On day 1, monocultures of 50,0000 bovine epithelial cells (BE) (bovine turbinates; ATCC®) were encapsulated in collagen gels (0.25 mL of 1.1 mg/ mL rat tail Type 1 collagen) in 12-well tissue culture polystyrene plates. The encapsulated cells were placed in an incubator at 37°C and 5% CO_2 for 45 minutes to allow for the gelation of collagen and hydrated thereafter with bovine epithelial cell medium. Culture media was exchanged on the BE monocultures on Day 2.

5.1.3 Assembly of Bovine Endothelial Monocultures

On Day 2, 17,0000 bovine airway endothelial cells (BAE) (bovine pulmonary artery endothelial cells; CPA 47, ATCC® CRL-1733) were encapsulated in collagen gels (0.25 mL of 1.1 mg/ mL rat tail Type 1 collagen) in 12-well tissue culture polystyrene plates. The encapsulated cells were placed in an incubator at 37°C and 5% CO_2 for 45 minutes to allow for the gelation of collagen and hydrated thereafter with BAE cell media.

5.1.4 Assembly of Epithelial-Endothelial 3D Models

In order to assemble the 3D co-culture models, 17,000 BAE cells were added 24 hours later to enable the BE cells to adhere and spread within the collagen gels. BAE cells were mixed with collagen (0.08 mL of 1.1 mg/ mL rat tail Type 1 collagen) and seeded above the encapsulated epithelial cells (**Figure 5.1**). A 3:1 ratio of BE to BAE cells was based on prior reports on *in vitro* human airway culture models (355, 356). In the co-culture system an optimized cell media (3:1 BE cell media: BAE cell media) was used.

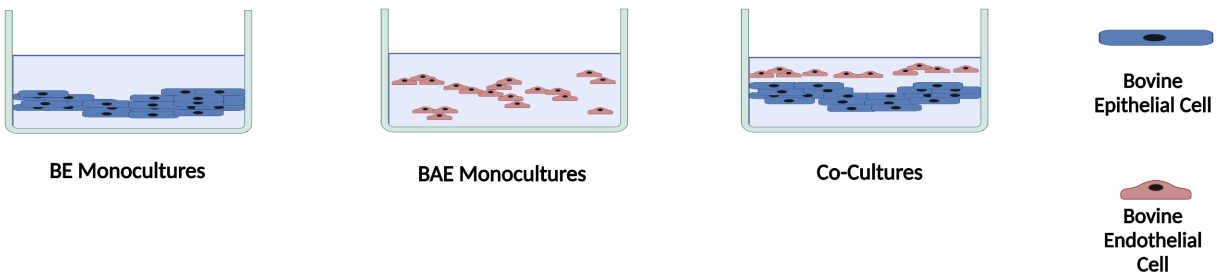

Figure 5.1 Schematic of the models assembled to study BRD. The three models include encapsulated bovine epithelial monocultures (BE), bovine airway endothelial cells (BAEC), and co-cultures with both cell types.

5.1.5 Bacterial Media

The medium from *H. somni* and *M. haemolytica* cultures was provided by Dr. T. J. Inzana. The *H. somni* ΔIbpA mutant strain lacks the Fic mutant, which causes cell death (283, 314). *M. haemolytica* TI619 is the wildtype strain generated by Dr. T. J. Inzana. Briefly, each bacterial strain was incubated and grown for 5 days. The supernatant of the biofilm cultures was collected, filtered, and sterilized. The bacteria medium suspension is referred to as concentrated culture supernatant (CCS), which contains molecules secreted in the medium from the cell culture (224, 357). The medium was maintained at -20°C until further use.

5.1.6 Different Culture Medium Formulations Used in this Study

The three medium conditions were 100% cell media (CM) – positive control, 50% CM and 50% bacterial media (BM), and 100% BM – negative control. The experiment was conducted with two timelines for media administration:

1. Continuous media: The same medium conditions were used throughout the culture period.
2. Revert media: 24 hours after the initial medium conditions were administered, cultures were then given respective cell media for the remainder of the culture period.

Here we describe the types and abbreviations used for different culture medium formulation:

Table 5.1 Descriptions of different media formulations.

Cell Media (CM)	100% cell media in monocultures or optimized to cell ratio in co-culture models
50/50 Revert	50% cell media, 50% bacterial media administered 24 h after organoids were assembled and then reverted back to 100% cell media 24 h later
50/50	50% cell media, 50% bacterial media (administered continuously through the culture period)
Bacterial Media (BM) Revert	100% bacterial media administered 24 h after organoids were assembled and then reverted back to 100% cell media 24 h later
BM	100% bacterial media (administered continuously through the culture period)

Different media formulations were administered over the culture period to mono- and co-cultures (**Figure 5.2**). On Day 3, three medium conditions were administered (**Table 5.1**). The three conditions include 100% cell media (CM), 50% CM and 50% bacterial media (BM) (50/50), and 100% BM. On Day 4, CM was given to 50/50 and BM (n = 3) to initiate 50/50 Revert and BM Revert. Cultures were ended on Day 4, Day 6, and Day 8. Culture medium was also exchanged in remaining models at each time point.

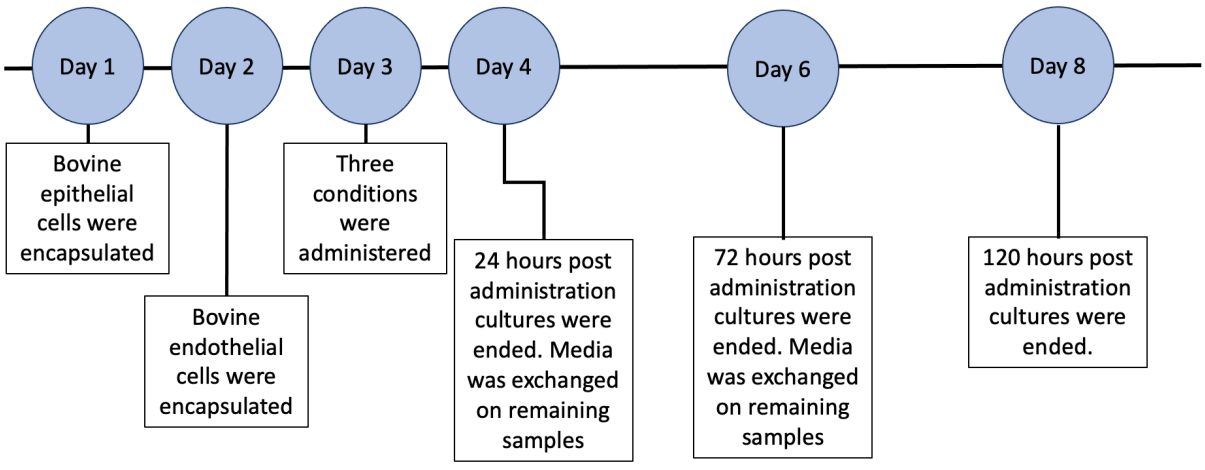

Figure 5.2 Experimental timeline for DNA analysis of various culture conditions of bacterial media.

5.1.7 DNA Measurements

At each time point, 0.1% w/v collagenase solution was added to cultures to break down the collagen gel (13-15, 17). The cells were collected, centrifuged, pelleted, and resuspended in 0.1% w/v SDS solution containing EDTA and TrisHCl. DNA quantification of the lysate was determined by the QuantIT Pico Green kit (Thermo Fisher Scientific). Absorbance was measured at an excitation/ emission wavelength of 480 and 520 nm, respectively (118). The DNA values were determined by calibrating to a standard curve generated with the provided Lambda DNA. The original samples were diluted 10 X in TE buffer prior to being assayed.

5.1.8 Immunostaining Cultures for Phenotypic Imaging

Cultures were fixed with a 2% (w/v) glutaraldehyde in PBS (1 X) solution followed by a 0.1% sodium borohydride ($NaBH_4$) solution in PBS (1 X) and 0.1% Triton-X solution in PBS (1 X) (7, 12, 358). A blocking solution of 5% horse serum in 1% BSA in PBS (1 X) solution was added to the cultures. Epithelial cells were visualized with a primary rabbit anti-bovine ZO-1 antibody followed by a secondary chicken anti-rabbit Alexa Fluor 488 antibody (Thermo Fisher Scientific). Endothelial cells were visualized with a mouse anti-bovine primary antibody followed by a goat anti-mouse Alexa Fluor 594 (Thermo Fisher Scientific). Imaging was conducted on a Zeiss LSM 800 confocal microscope.

5.1.9 Multiplex Assay for Cytokine Secretion

Cytokine analysis was conducted using a commercially available kit (EMD Millipore's MILLIPLEX® MAP Bovine Cytokine/ Chemokine Magnetic Bead Panel 1; Sigma Aldrich). The concentration of each cytokine was determined by calibrating to a standard curve on a Luminex® 200™. The median fluorescent intensity was analyzed using 5-parameter logistic or spline curve-fitting method for calculating analyte concentrations in each sample. This analysis was performed by Dr. Dianjun Cao and Dr. T. J. Inzana.

5.1.10 Statistical Analysis

A two-tailed Student's t-test with α = 0.05 was used to determine statistical significance assuming unequal variance. The Bonferroni correction (multiple hypothesis testing) was applied. All data is reported as the mean $\pm$ standard deviation where *n* represents the sample size. Comparisons were conducted between all models and days.

5.2 Results

5.2.1 Changes in Cell Proliferation with H. somni *CCS Administration*

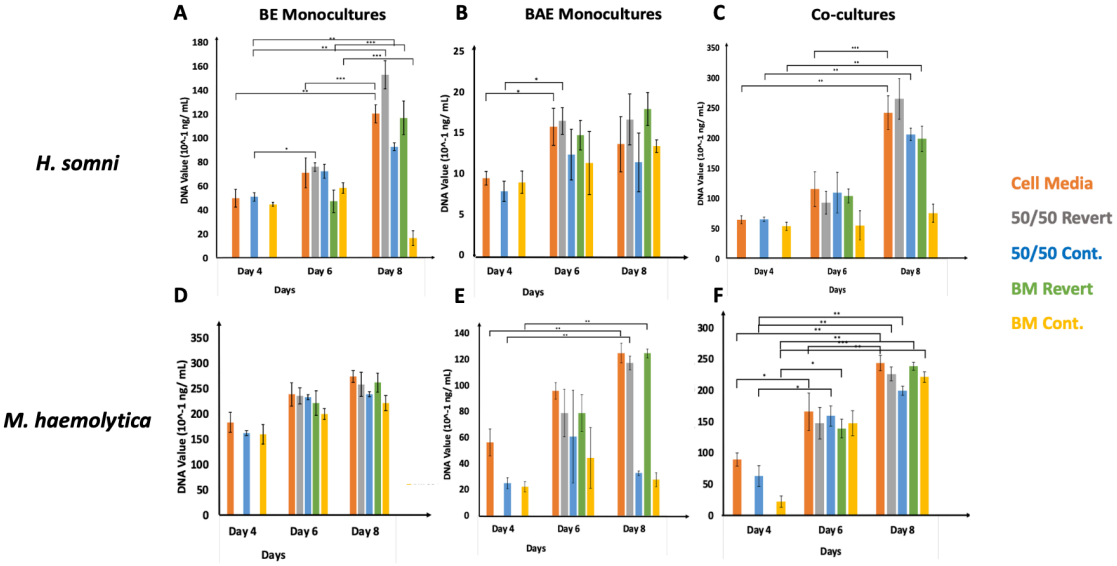

Figure 5.3 Cell proliferation due to effects of *H. somni* on (**A**) BE monocultures, (**B**) BAE monocultures, (**C**) co-cultures and *M. haemolytica* on (**D**) BE monocultures, (**E**) BAE monocultures, (**F**) co-cultures throughout the culture period. **p* < 0.05 Day 6 relative to Day 4 samples. ***p* < 0.05 Day 8 relative to Day 4 samples. ****p* < 0.05 Day 8 relative to Day 6 samples. n ≥ 3 for each sample.

BE monocultures do not exhibit cell proliferation upon *H. Somni* CCS administration (**Figure 5.3A**). However, if the BM is reverted back to CM, the cells recover, and show a 2.61-fold increase in proliferation on Day 8. There is a 7.18-fold difference in cell proliferation on Day 8 between

cells cultured under the condition of CM compared to continuous *H. Somni* CCS administration. 50/50 revert exhibited a 9.12-fold difference in cell proliferation compared to cells with continuous *H. Somni* CCS administration on Day 8. There was also a 6.98-fold increase in cell proliferation in BE monocultures on Day 8 when *H. Somni* CCS administration was reverted compared to continuous. Interestingly, cells with 50/50 continuous administration exhibited a 5.54-fold increase in DNA compared to continuous BM at Day 8. A lack of proliferation may be dependent on the concentration of soluble factors in the medium. A pathogenic genera of *H. somni*, which was used in this analysis, lacks the Fic mutant and secretes an IbpA protein, which is toxic to cells (283, 314).

The same trends are observed in co-cultures with *H. Somni* CCS administration compared to BE monocultures (**Figure 5.3C)**. Cultures do not proliferate upon *H. Somni* CCS administration continued throughout the time period. On Day 8, cells with continuous CM exhibit a 3.19-fold increase in proliferation compared to continuous *H. somni* CCS administration. Similar to BE monocultures, the concentration of soluble factors from *H. somni* in the culture medium administration affects proliferation. On Day 8, cells with 50/50 continuous administration proliferate 2.72-fold more than cells with continuous *H. somni* CCS administration. If the BM is reverted, the cells show a 2.62-fold increase in cell proliferation compared to continuous.

BAE monocultures with *H. Somni* CCS administration exhibit a different trend in comparison to BE mono- and co-cultures (**Figure 5.3B**). Despite medium conditions, proliferation of cells does not seem affected when cultured in the CCS of *H. somni*. A 1.65-fold increase in proliferation of BAE monocultures with CM was observed from Day 4 and Day 6. Additionally, there was a 2.07-fold increase in proliferation in cultures with 50/50 revert from Day Day 4 to Day 6. There were no significant differences in proliferation between media formulations at each time point.

5.2.2 Changes in Cell Proliferation with **M. haemolytica** *CCS Administration*

BE monocultures do not seem to be affected with *M. Haemolytica* CCS administration, as seen in **Figure 5.3D**. There were no significant increases in proliferation amongst the culture period and between medium formulations on each day.

BAE monocultures do not exhibit cell proliferation upon *M. Haemolytica* CCS administration (**Figure 5.3E**). On Day 8, there is a 5-fold decrease in cell proliferation for *M. Haemolytica* CCS continuous cultures compared to CM administered cultures. However, if the BM is reverted back to CM, proliferation occurs. There is a 4.68-fold and 5.61-fold increase in cell proliferation from Day 4 to Day 8 in both 50/50 and *M. Haemolytica* revert conditions, respectively, indicating that the cells seem to recover once the BM is removed and replaced with CM. However, there is not a significant increase in cell proliferation with continuous conditions (e.g. 50/ 50 and *M. Haemolytica* continuous) throughout the culture period, indicating that the CCS is preventing cell proliferation. This could potentially indicate that the soluble factors in *M. Haemolytica* CCS affect the BAE cells differently and cause cell death.

Co-cultures with revert and continuous media formulations exhibited significant increases in proliferation upon *M. Haemolytica* CCS administration from Day 4 to Day 8 (**Figure 5.3F)**. Initially, on Day 4, there is a 3.94-fold difference in cell proliferation between CM and *M. Haemolytica* CCS administration, indicating BM had an initial effect. From Day 4 to Day 6, there was a 6.06-fold increase in cell proliferation in BM revert administered co-cultures. Additionally, from Day 4 to Day 8, there is a 10-fold increase cell proliferation for BM cont. and BM revert administered co-cultures. This could indicate that the BAE cells are being affected at initial time points, but then, the effects of BE cells dominate.

5.2.3 Disruption of the Epithelial Barrier

The epithelial barrier serves as a physical defense mechanism to protect an organ from infection (252, 359). Bacteria can infiltrate the tissue or secrete endotoxins that can disrupt the tight junctions that adhere the cells (**Figure 5.4A**) (252, 359). Gram-negative bacteria secrete endotoxins, such as lipooligosaccharides, that initiate inflammatory responses in the host cells (360). The soluble factors secreted by both *H. somni* and *M. haemolytica* could cause the activation of such pathways which can alter the host cell's function and morphology (361). Tight junction formation was visualized by zonula occludens-1 (ZO-1) expression. CM cultures show the expression of tight junctions that are clearly visualized around the perimeter of the cells (**Figure 5.4B and C**). However, CCS causes a lack of this ZO-1 expression, indicating that pathogenic molecules secreted by the bacteria can interrupt this physial defense mechanism (**Figure 5.4D-G**).

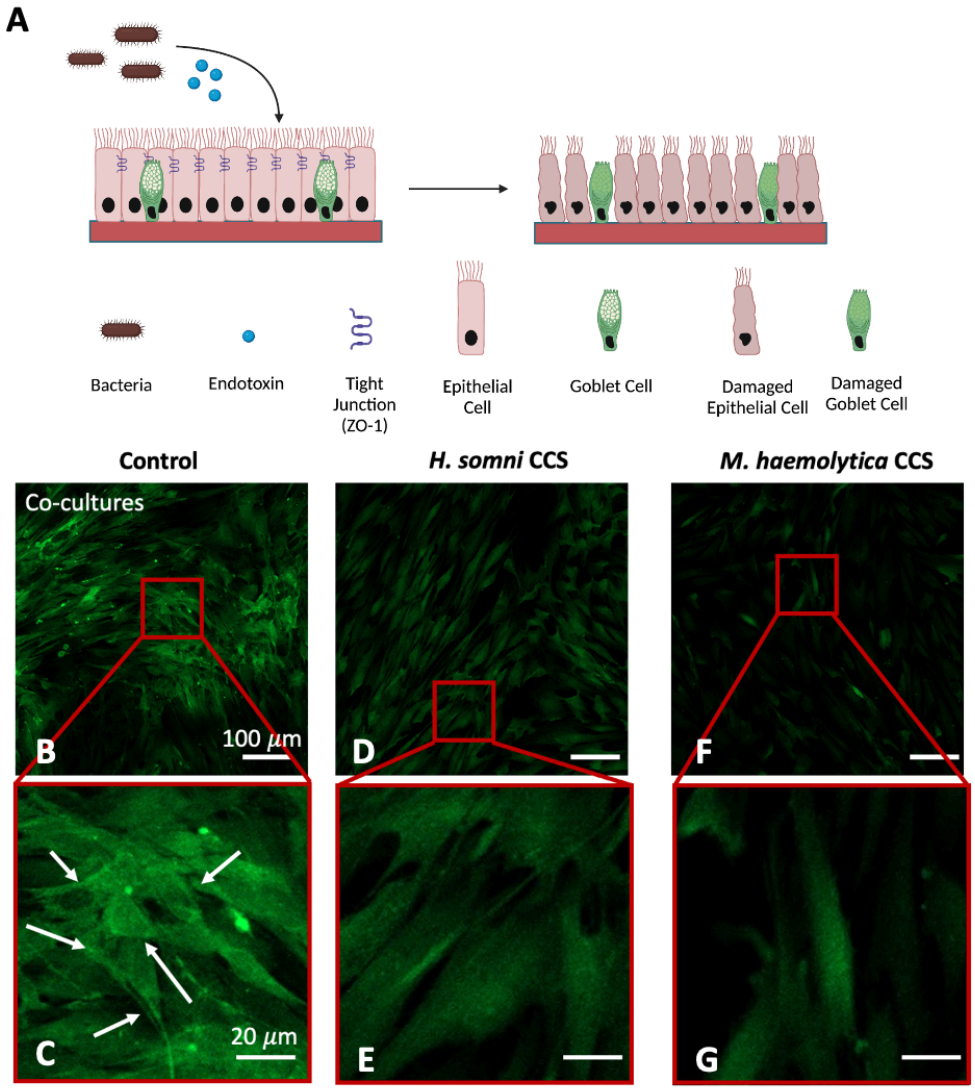

Figure 5.4 Schematic of the disruption of the epithelial barrier due to bacterial infection. Bacteria can either infiltrate the cells or secrete endotoxins that can alter protein expression. Representative images of co-cultures where BE cells are stained with ZO-1 where (**B**) and (**C**) show healthy, control cultures with clear membrane staining, (**D**) and (**E**) show a lack of ZO-1 due to *H. somni* CCS administration, and (**F**) and (**G**) show a lack of ZO-1 due to *M. haemolytica* CCS administration.

5.2.4 Secretion of Pro-Inflammatory Cytokines

Infection of host cells by bacteria can lead to an immune response and increases in pro-inflammatory cytokines (361-363). Pro-inflammatory cytokines secreted by BE cells after infection or CCS administration of BRD bacterial pathogens include TNF-α, IL-1, and IL-8 (224, 225, 299).

Different cytokines recruit immune cells, such as neutrophils, macrophages and T-cells, which further activate pathways that control inflammatory responses, such as (nuclear factor-κB) NF-κB (**Figure 5.5A**) (362, 363). A preliminary screening of pro-inflammatory cytokines released in the supernatant of the cultures was conducted. From Day 4 to Day 8, there is up a 28 and 31-fold increase in IL-6 secretion in 50/50 revert and 50/50 continuous (**Figure 5.5B**). Despite the BM being reverted, pro-inflammatory cytokines are still secreted. This could potentially indicate that the inflammatory pathways within the cells are still activated (362).

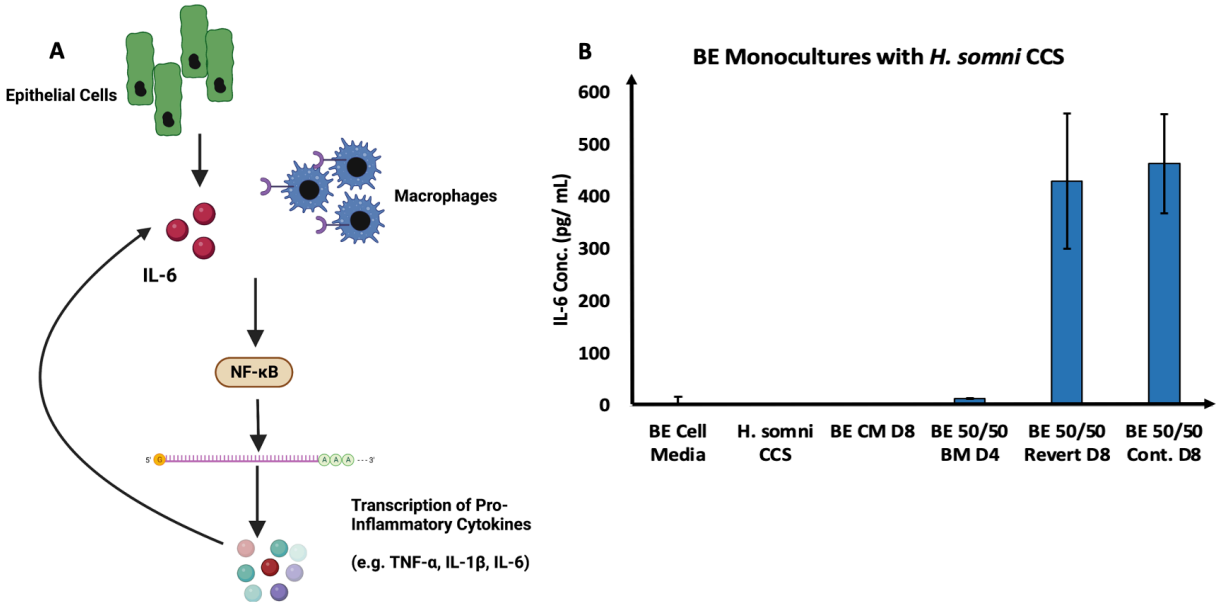

Figure 5.5 Schematic of IL-6 cytokine secretion from damaged epithelial cells. Epithelial cells secrete IL-6, which recruits the immune system, leading to activation of the NF-kB pathway and the further downstream transcription and translation of other pro-inflammatory cytokines. (**B**) IL-6 cytokine secretion from BE monocultures with *H. somni* CCS administration.

5.3 Discussion

We have designed a 3D co-culture model with BE and BAE cells. To the best of our knowledge, this is the first 3D bovine respiratory model. In the literature, submerged tissue cultures and air-liquid interface models, 2D cultures, are primarily used for BRD studies (214, 224, 225, 273, 274, 280). However, 3D cultures with more than one cell type have been shown to improve function of cells, which can be used with better accuracy for a wider range of applications (340, 341). The

bovine airway system needs to be studied in further depth before *in vitro* models can fully recapitulate the environment. Although mammalian systems have similar features, species-specific differences in cattle must be determined (323). Therefore, the current ratio of cells in the reported models was determined based on human airway organoids (355, 356).

The first step for investigating BRD infection in the 3D models was to use CCS from bacterial cultures. Signaling molecules from an infection site can travel through the bloodstream (364). Therefore, CCS can be used to mimic an infectious phase occurring inside the body (364). Bacteria cultures secrete cytokines, endotoxins, and leukotoxins which all contribute to an infectious response (224, 282, 314, 316). Although this is an initial step in studying infectious signaling mechanisms, inoculation with different genera of bacteria directly on cultures can be used to examine how the pathogens invade the host cells (365).

BE and BAE cells respond differently to *M. haemolytica* and *H. somni* CCS. In a report by Cozens et. al., the pathogenic serotype A1 strain of *M. Haemolytica* was inoculated on differentiated BE cells in an ALI model (214). Results showed that the bacterial cells enter the bovine cells by transcytosis and undergo intracellular replication (214). From there, the proliferated bacteria spread to neighboring cells and causes additional damage (214). Since the epithelium undergoes constant replication, the bacteria can infect subsequent cells and proliferate faster (214). In this analysis, only *M. Haemolytica* CCS is administered. When bacteria are inoculated on these encapsulated cells and allowed biofilm formation occurs, there may be a different response to *M. Haemolytica* that could provide insight into the mechanism of infection.

The BAE cells used in this model are already infected with BVDV. It could be possible that the initial viral infection prevents *H. Somni* from affecting these cells. This result could question the order of infection involved in BRD (207, 208, 282). In a report by Boukahil and Czuprynski, *M.*

Haemolytica biofilm formation was not affected by BRSV and BVDV infection of BE cells in a monolayer (255). Infection of the BE cells by the two viruses occurred prior to seeding of bacterial cells (255). However, another report by Gershwin et. al. reported a more diseased state when bovines were infected with BRSV first and then *H. Somni* (223). This study was conducted on calves and results were determined through clinical signs, biopsies, and histological examination (223).

Gram-negative bacteria secrete endotoxins that activate inflammatory and cell death pathways (360). The pro-inflammatory cytokines can cause downstream activation of the NF-κB and mitogen-activated protein (MAP) kinase signaling pathways (361, 366, 367). The NF-κB pathway controls immune and inflammatory responses upon infection (366). Cell growth and apoptosis mechanisms are also controlled by this pathway (366). MAP kinase pathways regulate cell proliferation and death (367). Such molecules could have been secreted in the bacterial CCS, which caused disruptions in protein expression, such as ZO-1, in host epithelial cells. Further quantification and determination of the signaling molecules secreted by the bacteria in the CCS requires investigation.

5.4 Future Work

We have used our co-culture model with administered CCS as an initial analysis of BRD infection. The 3D co-culture model includes more than one cell type and allows for intercellular signaling which better mimics *in vivo* architecture (340, 341). The next steps are to inoculate various genera of bacteria on the models to understand how infection occurs by bacterial-host cell interactions and signaling from soluble factors secreted by both cells (214). Further analysis of different cytokine and chemokine secretions will also provide insight into which pathways become activated upon infection. Determination of signaling molecules in the CCS may also provide

insight into how soluble factors impact host cells. The co-culture model can be further characterized by investigating intercellular signaling and migration between BE and BAE cells. After mechanism of infection is studied, these models can be used to test and develop antimicrobial treatments for BRD.

Chapter 6: Conclusions and Future Work

6.1 Conclusions

In this dissertation, the use of organoids for various applications has been described. Specifically, we (i) investigated the significant transcriptomic and phenotypic differences between iHLCs and PHHs, (ii) motivated a critical need for a systematic approach to mature iHLCs, (iii) assembled 3D multicellular human liver organoids that mature iHLCs solely through intercellular signaling, and (iv) showed how the versatility of organoids may be used to study other diseases, such as the bovine respiratory disease. The research presented here encompasses the following:

- **Chapter 2**: From RNA-seq analysis, iHLCs and PHHs exhibit significant differences in gene expression, including bile secretion, TCA cycle, and drug metabolism.
- **Chapter 2**: The transcriptomic analysis explains the phenotypic differences observed between the two cell types, which motivates a critical need to mature iHLCs before they can be used as a sustainable replacement for PHHs.
- **Chapter 3**: iHLCs are matured solely through intercellular signaling when assembled in a 3D multicellular human liver organoid with LSECs and KCs in a stratified architecture.
- **Chapter 3**: After either seven or 14-days, iHLCs exhibit significant decreases in fetal and increases in adult markers, similar to PHHs when cultured in equivalent organoids, indicating that the cells have matured.
- **Chapter 3**: The secretion and modulation of PGE2, only when KCs are present in the organoid, may be the primary driver of maturation, since a decrease in this molecule is observed when iHLCs exhibit adult markers and functions.
- **Chapter 4**: There is a critical need for a 3D model of the bovine airway to study BRD for antimicrobial development since current work primarily uses monolayers or

monocultures, which is not an accurate representation of the dynamic respiratory system.

- **Chapter 5**: We have developed a 3D co-culture bovine airway model with epithelial and endothelial cells that can be used for bacterial biofilm inoculation studies and antimicrobial development.
- **Chapter 5**: The 3D co-culture bovine airway models mimicked effects of infection after the administration of *H. somni* CCS potentially due to the secretion of IbpA which is toxic to cells.

6.2 Future Work

We designed a 3D multicellular human liver organoid with LSECs and KCs that can mature iHLCs solely through intercellular signaling. This unique approach can be systematically adapted throughout the liver research community for the efficient generation of matured iHLCs within seven or 14-days. This methodology can even be applied to the maturation of other iPSC-derived cells and huma organ systems. The widespread use of matured iHLCs holds tremendous potential for future patient-specific studies. Future areas of investigation include 3D human liver organoids (1) for the transcriptomic analysis of matured iHLCs, (2) organoids for iPSC differentiation, and (3) virology applications.

6.2.1 Transcriptomic Analysis of Matured iHLCs

In **Chapter 2**, we performed bulk RNA-seq to investigate the transcriptomic differences between iHLCs and PHHs. This work motivated the need to mature iHLCs before they can be used alongside PHHs. However, a transcriptomic analysis of matured iHLCs (**Chapter 3**) would elucidate differentially expressed gene changes throughout time and compared to PHHs. This can be done using single-cell RNA-seq (scRNA-seq). This method is more precise than bulk RNA-

seq because it examines the RNA transcripts from single cells rather than a population of cells. For example, one computational framework that could be used to analyze the scRNA-seq data includes Seurat, since it allows for multiple modalities to be measured and compares the expression values from the data to a reference database (368, 369). Other computational frameworks, such as Tricycle, which maps cells in different stages of the cell cycle (368), may also be useful in identifying if iHLCs are transitioning towards a mature rather than stem cell-like state, which would correspond to the phenotypic $Ki67^{+}$ observations.

6.2.2 Organoids for iPSC Differentiation

In **Chapter 3**, we showed how iHLCs can be matured by the interactions with LSECs and KCs in a 3D human liver organoid. In liver embryogenesis, NPCs secrete different molecules to mature hepatic progenitor cells to hepatocytes. Since secretion of maturation molecules improved adult markers of iHLCs in the organoids, we hypothesize whether signaling from NPCs may differentiate iPSCs towards a hepatic lineage. Typically, exogenous factors are administered to iPSCs to differentiate the cells towards the definitive endoderm and hepatoblast state. However, this method would be instrumental in maturing iPSCs without the need for experimental manipulation. The expression of markers including AFP and HNF4α would indicate that the cells are differentiating towards a the hepatoblast stage. Expression of mature hepatocyte markers, including albumin and CYP3A4 can be measured to determine if the cells have reached a matured state.

6.2.3 Organoids for Virology

In **Chapters 4** and **5**, we showed how organoids can be a valuable technology for various applications, such as studying BRD. The COVID-19 pandemic has been a lesson to prepare for future global infections (370). *In vitro* models could provide valuable insight into studying how viruses jump from species, adapt in specific cells (animal or human), and spread throughout the

population (370). The hepatitis E virus (HEV) is a common cause of acute hepatitis infection, with a mortality rate of 30% in infected individuals (371).

However, there is no specific treatment for HEV since the mechanism of infectivity is unknown and remains a challenge for researchers (371). The need for investigation and expansion of knowledge on HEV is tremendous as future mutations of this virus could spread. Organoids can be instrumental in understanding the mechanism of infection of viruses, including HEV. Ongoing work includes the assembly of liver organoids for HEV infection with the goal to better guide the development of specific therapeutics. In collaboration with the Meng research group at Virginia Tech, preliminary data shows that assembled liver organoids with PHHs, LSECs, and LX-2s, a hepatic stellate cell line, can be infected with HEV. Future work could include the use of iHLC-based liver organoids to reduce donor variations exhibited by PHHs. HEV could be used as a model virus to not only study its mechanisms but show how organoids for virology can be a highly adaptive technology.

Chapter 7: References

1. I. M. A. H. J. A. J. L. B. D. E. C. D. A. S. S. S. T. A. W. Wolkoff, *The Liver: Biology and Pathobiology* (Lippincott Williams and Wilkins, Philadelphia, PA, ed. 4th Edition, 2001).
2. S. R. Abdel-Misih, M. Bloomston, Liver anatomy. *Surg Clin North Am* **90**, 643-653 (2010).
3. H. Ishibashi, M. Nakamura, A. Komori, K. Migita, S. Shimoda, Liver architecture, cell function, and disease. *Seminars in Immunopathology* **31**, 399-409 (2009).
4. G. W. Telega, "17 - Hepatomegaly" in Nelson Pediatric Symptom-Based Diagnosis: Common Diseases and their Mimics (Second Edition), R. M. Kliegman, H. Toth, B. J. Bordini, D. Basel, Eds. (Elsevier, Philadelphia, 2023), https://doi.org/10.1016/B978-0-323-76174-1.00017-1, pp. 306-319.e301.
5. A. Joseph, H. Samant, "Jaundice" in StatPearls. (StatPearls Publishing Copyright © 2023, StatPearls Publishing LLC., Treasure Island (FL), 2023).
6. W. Hou, A. J. Sanyal, Ascites: diagnosis and management. *Med Clin North Am* **93**, 801-817, vii (2009).
7. S. M. Orbach, M. E. Cassin, M. F. Ehrich, P. Rajagopalan, Investigating acetaminophen hepatotoxicity in multi-cellular organotypic liver models. *Toxicology in Vitro* **42**, 10-20 (2017).
8. R. Guo, X. Xu, Y. Lu, X. Xie, Physiological oxygen tension reduces hepatocyte dedifferentiation in in vitro culture. *Scientific Reports* **7**, 5923 (2017).
9. C. Eipel, K. Abshagen, B. Vollmar, Regulation of hepatic blood flow: the hepatic arterial buffer response revisited. *World J Gastroenterol* **16**, 6046-6057 (2010).
10. J. Fan *et al.*, Hemodynamic changes in hepatic sinusoids of hepatic steatosis mice. *World J Gastroenterol* **25**, 1355-1365 (2019).
11. L. R. Wills, P. Rajagopalan, Advances in Human Induced Pluripotent Stem Cell-Derived Hepatocytes for Use in Toxicity Testing. *Annals of Biomedical Engineering* **48**, 1045-1057 (2020).
12. S. M. Orbach, M. F. Ehrich, P. Rajagopalan, High-throughput toxicity testing of chemicals and mixtures in organotypic multi-cellular cultures of primary human hepatic cells. *Toxicology in Vitro* **51**, 83-94 (2018).
13. S. M. Orbach, A. J. Ford, S.-E. Saverot, P. Rajagopalan, Multi-cellular transitional organotypic models to investigate liver fibrosis. *Acta Biomaterialia* **82**, 79-92 (2018).
14. Y. Kim, A. L. Larkin, R. M. Davis, P. Rajagopalan, The design of in vitro liver sinusoid mimics using chitosan-hyaluronic acid polyelectrolyte multilayers. *Tissue Eng Part A* **16**, 2731-2741 (2010).
15. A. L. Larkin, R. R. Rodrigues, T. M. Murali, P. Rajagopalan, Designing a multicellular organotypic 3D liver model with a detachable, nanoscale polymeric Space of Disse. *Tissue Eng Part C Methods* **19**, 875-884 (2013).
16. P. Gissen, I. M. Arias, Structural and functional hepatocyte polarity and liver disease. *J Hepatol* **63**, 1023-1037 (2015).
17. A. J. Ford, G. Jain, P. Rajagopalan, Designing a fibrotic microenvironment to investigate changes in human liver sinusoidal endothelial cell function. *Acta Biomaterialia* **24**, 220-227 (2015).
18. S. L. Friedman, Hepatic stellate cells: protean, multifunctional, and enigmatic cells of the liver. *Physiol Rev* **88**, 125-172 (2008).
19. T. Tsuchida, S. L. Friedman, Mechanisms of hepatic stellate cell activation. *Nature Reviews Gastroenterology & Hepatology* **14**, 397-411 (2017).

20. A. A. Palakkan, J. Nanda, J. A. Ross, Pluripotent stem cells to hepatocytes, the journey so far. *Biomed Rep* **6**, 367-373 (2017).
21. P. Godoy *et al.*, Recent advances in 2D and 3D in vitro systems using primary hepatocytes, alternative hepatocyte sources and non-parenchymal liver cells and their use in investigating mechanisms of hepatotoxicity, cell signaling and ADME. *Archives of Toxicology* **87**, 1315-1530 (2013).
22. W. L. Thompson, T. Takebe, Human liver model systems in a dish. *Dev Growth Differ* **63**, 47-58 (2021).
23. A. S. Serras *et al.*, A Critical Perspective on 3D Liver Models for Drug Metabolism and Toxicology Studies. *Frontiers in Cell and Developmental Biology* **9** (2021).
24. H. K. Kang *et al.*, Establishing a 3D In Vitro Hepatic Model Mimicking Physiologically Relevant to In Vivo State. *Cells* **10** (2021).
25. M. J. Ramos, L. Bandiera, F. Menolascina, J. A. Fallowfield, In vitro models for non-alcoholic fatty liver disease: Emerging platforms and their applications. *iScience* **25**, 103549 (2022).
26. C. Mora, M. Serzanti, A. Consiglio, M. Memo, P. Dell'Era, Clinical potentials of human pluripotent stem cells. *Cell Biology and Toxicology* **33**, 351-360 (2017).
27. Y. Shi, H. Inoue, J. C. Wu, S. Yamanaka, Induced pluripotent stem cell technology: a decade of progress. *Nature Reviews Drug Discovery* **16**, 115-130 (2017).
28. S. Yamanaka, Pluripotent Stem Cell-Based Cell Therapy-Promise and Challenges. *Cell Stem Cell* **27**, 523-531 (2020).
29. S. Yamanaka, Induced pluripotent stem cells: past, present, and future. *Cell Stem Cell* **10**, 678-684 (2012).
30. Y. Yoshida, S. Yamanaka, Induced Pluripotent Stem Cells 10 Years Later: For Cardiac Applications. *Circ Res* **120**, 1958-1968 (2017).
31. I. A. Charitos *et al.*, Stem Cells: A Historical Review about Biological, Religious, and Ethical Issues. *Stem Cells Int* **2021**, 9978837 (2021).
32. A. Leventhal, G. Chen, A. Negro, M. Boehm, The benefits and risks of stem cell technology. *Oral Dis* **18**, 217-222 (2012).
33. K. Takahashi *et al.*, Induction of pluripotent stem cells from adult human fibroblasts by defined factors. *Cell* **131**, 861-872 (2007).
34. K. Takahashi, S. Yamanaka, Induction of pluripotent stem cells from mouse embryonic and adult fibroblast cultures by defined factors. *Cell* **126**, 663-676 (2006).
35. J. de Jong, L. H. Looijenga, Stem cell marker OCT3/4 in tumor biology and germ cell tumor diagnostics: history and future. *Crit Rev Oncog* **12**, 171-203 (2006).
36. S. Masui *et al.*, Pluripotency governed by Sox2 via regulation of Oct3/4 expression in mouse embryonic stem cells. *Nature Cell Biology* **9**, 625-635 (2007).
37. D. C. Di Giammartino *et al.*, KLF4 is involved in the organization and regulation of pluripotency-associated three-dimensional enhancer networks. *Nature Cell Biology* **21**, 1179-1190 (2019).
38. R. Araki *et al.*, Crucial role of c-Myc in the generation of induced pluripotent stem cells. *Stem Cells* **29**, 1362-1370 (2011).
39. G. Pan, J. A. Thomson, Nanog and transcriptional networks in embryonic stem cell pluripotency. *Cell Res* **17**, 42-49 (2007).
40. L. Wang *et al.*, NANOG and LIN28 dramatically improve human cell reprogramming by modulating LIN41 and canonical WNT activities. *Biol Open* **8** (2019).
41. P. W. Burridge *et al.*, Chemically defined generation of human cardiomyocytes. *Nat Methods* **11**, 855-860 (2014).
42. E. M. Abud *et al.*, iPSC-Derived Human Microglia-like Cells to Study Neurological Diseases. *Neuron* **94**, 278-293.e279 (2017).

43. N. Gunhanlar *et al.*, A simplified protocol for differentiation of electrophysiologically mature neuronal networks from human induced pluripotent stem cells. *Molecular Psychiatry* **23**, 1336-1344 (2018).
44. O. H. Jeon *et al.*, Human iPSC-derived osteoblasts and osteoclasts together promote bone regeneration in 3D biomaterials. *Scientific Reports* **6**, 26761 (2016).
45. K. Si-Tayeb *et al.*, Highly efficient generation of human hepatocyte-like cells from induced pluripotent stem cells. *Hepatology* **51**, 297-305 (2010).
46. J. Wang, M. Sun, W. Liu, Y. Li, M. Li, Stem Cell-Based Therapies for Liver Diseases: An Overview and Update. *Tissue Eng Regen Med* **16**, 107-118 (2019).
47. S. Pauklin, L. Vallier, Activin/Nodal signalling in stem cells. *Development* **142**, 607-619 (2015).
48. D. C. Hay *et al.*, Highly efficient differentiation of hESCs to functional hepatic endoderm requires ActivinA and Wnt3a signaling. *Proc Natl Acad Sci U S A* **105**, 12301-12306 (2008).
49. M. Mossahebi-Mohammadi, M. Quan, J.-S. Zhang, X. Li, FGF Signaling Pathway: A Key Regulator of Stem Cell Pluripotency. *Frontiers in Cell and Developmental Biology* **8** (2020).
50. C. Du *et al.*, Highly efficient and expedited hepatic differentiation from human pluripotent stem cells by pure small-molecule cocktails. *Stem Cell Research & Therapy* **9**, 58 (2018).
51. A. Kamiya, T. Kinoshita, A. Miyajima, Oncostatin M and hepatocyte growth factor induce hepatic maturation via distinct signaling pathways. *FEBS Lett* **492**, 90-94 (2001).
52. G. K. Michalopoulos, W. C. Bowen, K. Mulè, J. Luo, HGF-, EGF-, and dexamethasone-induced gene expression patterns during formation of tissue in hepatic organoid cultures. *Gene Expr* **11**, 55-75 (2003).
53. S. K. Mallanna, S. A. Duncan, Differentiation of hepatocytes from pluripotent stem cells. *Curr Protoc Stem Cell Biol* **26**, 1g.4.1-1g.4.13 (2013).
54. Y. Xie, J. Yao, W. Jin, L. Ren, X. Li, Induction and Maturation of Hepatocyte-Like Cells In Vitro: Focus on Technological Advances and Challenges. *Frontiers in Cell and Developmental Biology* **9** (2021).
55. N. Gandhi *et al.*, Comparative transcriptomic and phenotypic analysis of induced pluripotent stem cell hepatocyte-like cells and primary human hepatocytes. *Cell and Tissue Research* 10.1007/s00441-024-03868-9 (2024).
56. A.-K. M. Sjogren *et al.*, Critical differences in toxicity mechanisms in induced pluripotent stem cell-derived hepatocytes, hepatic cell lines and primary hepatocytes. *Archives of Toxicology* **88**, 1427-1437 (2014).
57. J. L. Corbett, S. A. Duncan, iPSC-Derived Hepatocytes as a Platform for Disease Modeling and Drug Discovery. *Front Med (Lausanne)* **6** (2019).
58. M. Kehtari, B. Zeynali, M. Soleimani, M. Kabiri, E. Seyedjafari, Fabrication of a co-culture micro-bioreactor device for efficient hepatic differentiation of human induced pluripotent stem cells (hiPSCs). *Artif Cells Nanomed Biotechnol* **46**, 161-170 (2018).
59. J. H. Kim *et al.*, Enhanced Metabolizing Activity of Human ES Cell-Derived Hepatocytes Using a 3D Culture System with Repeated Exposures to Xenobiotics. *Toxicol Sci* **147**, 190-206 (2015).
60. J. E. Kaserman, A. A. Wilson, Protocol for Directed Differentiation of Human Induced Pluripotent Stem Cells (iPSCs) to a Hepatic Lineage. *Methods Mol Biol* **1639**, 151-160 (2017).
61. O. Kurauchi *et al.*, The concentration of hepatocyte growth factor (HGF) in human amniotic fluid at second trimester: relation to fetal birth weight. *Horm Metab Res* **27**, 335-338 (1995).

62. J. Huang, X. Guo, W. Li, H. Zhang, Activation of Wnt/β-catenin signalling via GSK3 inhibitors direct differentiation of human adipose stem cells into functional hepatocytes. *Sci Rep* **7**, 40716 (2017).
63. R. Siller, S. Greenhough, E. Naumovska, G. J. Sullivan, Small-molecule-driven hepatocyte differentiation of human pluripotent stem cells. *Stem Cell Reports* **4**, 939-952 (2015).
64. K. Czysz, S. Minger, N. Thomas, DMSO efficiently down regulates pluripotency genes in human embryonic stem cells during definitive endoderm derivation and increases the proficiency of hepatic differentiation. *PLoS One* **10**, e0117689 (2015).
65. S. Chetty *et al.*, A simple tool to improve pluripotent stem cell differentiation. *Nat Methods* **10**, 553-556 (2013).
66. J. Li *et al.*, A transient DMSO treatment increases the differentiation potential of human pluripotent stem cells through the Rb family. *PLoS One* **13**, e0208110-e0208110 (2018).
67. J. Krumm *et al.*, High temporal resolution proteome and phosphoproteome profiling of stem cell-derived hepatocyte development. *Cell Rep* **38**, 110604 (2022).
68. Y. Kondo *et al.*, Histone deacetylase inhibitor valproic acid promotes the differentiation of human induced pluripotent stem cells into hepatocyte-like cells. *PLoS One* **9**, e104010 (2014).
69. D. Huangfu *et al.*, Induction of pluripotent stem cells by defined factors is greatly improved by small-molecule compounds. *Nature biotechnology* **26**, 795-797 (2008).
70. M. N. B. Ramli *et al.*, Human Pluripotent Stem Cell-Derived Organoids as Models of Liver Disease. *Gastroenterology* **159**, 1471-1486.e1412 (2020).
71. V. M. Lauschke, D. F. Hendriks, C. C. Bell, T. B. Andersson, M. Ingelman-Sundberg, Novel 3D Culture Systems for Studies of Human Liver Function and Assessments of the Hepatotoxicity of Drugs and Drug Candidates. *Chem Res Toxicol* **29**, 1936-1955 (2016).
72. H. Ardalani *et al.*, 3-D culture and endothelial cells improve maturity of human pluripotent stem cell-derived hepatocytes. *Acta Biomater* **95**, 371-381 (2019).
73. K. Takayama *et al.*, 3D spheroid culture of hESC/hiPSC-derived hepatocyte-like cells for drug toxicity testing. *Biomaterials* **34**, 1781-1789 (2013).
74. R. Ouchi *et al.*, Modeling Steatohepatitis in Humans with Pluripotent Stem Cell-Derived Organoids. *Cell Metabolism* **30**, 374-384.e376 (2019).
75. G. Pettinato *et al.*, Generation of fully functional hepatocyte-like organoids from human induced pluripotent stem cells mixed with Endothelial Cells. *Scientific Reports* **9**, 8920 (2019).
76. T. Takebe *et al.*, Vascularized and functional human liver from an iPSC-derived organ bud transplant. *Nature* **499**, 481-484 (2013).
77. J. Z. Tong, S. Sarrazin, D. Cassio, F. Gauthier, F. Alvarez, Application of spheroid culture to human hepatocytes and maintenance of their differentiation. *Biology of the Cell* **81**, 77-81 (1994).
78. Y. A. Bi, D. Kazolias, D. B. Duignan, Use of cryopreserved human hepatocytes in sandwich culture to measure hepatobiliary transport. *Drug Metab Dispos* **34**, 1658-1665 (2006).
79. X. Gao, Y. Liu, A transcriptomic study suggesting human iPSC-derived hepatocytes potentially offer a better in vitro model of hepatotoxicity than most hepatoma cell lines. *Cell Biology and Toxicology* **33**, 407-421 (2017).
80. A. Baiocchini *et al.*, Extracellular Matrix Molecular Remodeling in Human Liver Fibrosis Evolution. *PLoS One* **11**, e0151736 (2016).
81. M. Lorvellec *et al.*, Mouse decellularised liver scaffold improves human embryonic and induced pluripotent stem cells differentiation into hepatocyte-like cells. *PLoS One* **12**, e0189586 (2017).

82. B. Wang *et al.*, Functional Maturation of Induced Pluripotent Stem Cell Hepatocytes in Extracellular Matrix-A Comparative Analysis of Bioartificial Liver Microenvironments. *Stem Cells Transl Med* **5**, 1257-1267 (2016).
83. M. R. Poorna, S. Sudhindran, M. V. Thampi, U. Mony, Differentiation of induced pluripotent stem cells to hepatocyte-like cells on cellulose nanofibril substrate. *Colloids Surf B Biointerfaces* **198**, 111466 (2021).
84. T. Shinozawa *et al.*, High-Fidelity Drug-Induced Liver Injury Screen Using Human Pluripotent Stem Cell-Derived Organoids. *Gastroenterology* **160**, 831-846.e810 (2021).
85. N. Mobarra *et al.*, Hybrid poly-l-lactic acid/poly(ε-caprolactone) nanofibrous scaffold can improve biochemical and molecular markers of human induced pluripotent stem cell-derived hepatocyte-like cells. *J Cell Physiol* **234**, 11247-11255 (2019).
86. S. S. Ng *et al.*, Human iPS derived progenitors bioengineered into liver organoids using an inverted colloidal crystal poly (ethylene glycol) scaffold. *Biomaterials* **182**, 299-311 (2018).
87. I. D. Orge *et al.*, Phenotype instability of hepatocyte-like cells produced by direct reprogramming of mesenchymal stromal cells. *Stem Cell Research & Therapy* **11**, 154 (2020).
88. M. Ballester *et al.*, Direct conversion of human fibroblast to hepatocytes using a single inducible polycistronic vector. *Stem Cell Research & Therapy* **10**, 317 (2019).
89. D. Nakamori, H. Akamine, K. Takayama, F. Sakurai, H. Mizuguchi, Direct conversion of human fibroblasts into hepatocyte-like cells by ATF5, PROX1, FOXA2, FOXA3, and HNF4A transduction. *Scientific Reports* **7**, 16675 (2017).
90. K. P. Simeonov, H. Uppal, Direct reprogramming of human fibroblasts to hepatocyte-like cells by synthetic modified mRNAs. *PLoS One* **9**, e100134 (2014).
91. M. Rombaut *et al.*, Direct reprogramming of somatic cells into induced hepatocytes: Cracking the Enigma code. *J Hepatol* **75**, 690-705 (2021).
92. Y. Du *et al.*, Human hepatocytes with drug metabolic function induced from fibroblasts by lineage reprogramming. *Cell Stem Cell* **14**, 394-403 (2014).
93. P. Huang *et al.*, Direct reprogramming of human fibroblasts to functional and expandable hepatocytes. *Cell Stem Cell* **14**, 370-384 (2014).
94. A. Afshari, S. Shamdani, G. Uzan, S. Naserian, N. Azarpira, Different approaches for transformation of mesenchymal stem cells into hepatocyte-like cells. *Stem Cell Res Ther* **11**, 54 (2020).
95. I. Laudadio *et al.*, A feedback loop between the liver-enriched transcription factor network and miR-122 controls hepatocyte differentiation. *Gastroenterology* **142**, 119-129 (2012).
96. M. Girard, E. Jacquemin, A. Munnich, S. Lyonnet, A. Henrion-Caude, miR-122, a paradigm for the role of microRNAs in the liver. *J Hepatol* **48**, 648-656 (2008).
97. R. G. Rowe, G. Q. Daley, Induced pluripotent stem cells in disease modelling and drug discovery. *Nat Rev Genet* **20**, 377-388 (2019).
98. V. Sauer, N. Roy-Chowdhury, C. Guha, J. Roy-Chowdhury, Induced pluripotent stem cells as a source of hepatocytes. *Curr Pathobiol Rep* **2**, 11-20 (2014).
99. Z. Xu *et al.*, Analysis of differentially expressed genes among human hair follicle–derived iPSCs, induced hepatocyte-like cells, and primary hepatocytes. *Stem Cell Research & Therapy* **9**, 211 (2018).
100. Z. Song *et al.*, Efficient generation of hepatocyte-like cells from human induced pluripotent stem cells. *Cell Research* **19**, 1233-1242 (2009).
101. J. Wang *et al.*, Differentiation of human foreskin fibroblast-derived induced pluripotent stem cells into hepatocyte-like cells. *Cell Biochem Funct* **34**, 475-482 (2016).
102. K. Zeilinger, N. Freyer, G. Damm, D. Seehofer, F. Knöspel, Cell sources for in vitro human liver cell culture models. *Exp Biol Med (Maywood)* **241**, 1684-1698 (2016).

103. R. Gupta *et al.*, Comparing in vitro human liver models to in vivo human liver using RNA-Seq. *Arch Toxicol* **95**, 573-589 (2021).
104. L. E. Viiri *et al.*, Extensive reprogramming of the nascent transcriptome during iPSC to hepatocyte differentiation. *Scientific Reports* **9**, 3562 (2019).
105. Z. Wang, M. Gerstein, M. Snyder, RNA-Seq: a revolutionary tool for transcriptomics. *Nat Rev Genet* **10**, 57-63 (2009).
106. Y. Kim, P. Rajagopalan, 3D Hepatic Cultures Simultaneously Maintain Primary Hepatocyte and Liver Sinusoidal Endothelial Cell Phenotypes. *PLoS One* **5**, e15456 (2010).
107. X. Zhang, I. Jonassen, RASflow: an RNA-Seq analysis workflow with Snakemake. *BMC Bioinformatics* **21**, 110 (2020).
108. D. Kim, B. Langmead, S. L. Salzberg, HISAT: a fast spliced aligner with low memory requirements. *Nat Methods* **12**, 357-360 (2015).
109. J. Herrero *et al.*, Ensembl comparative genomics resources. *Database (Oxford)* **2016** (2016).
110. Y. Liao, G. K. Smyth, W. Shi, featureCounts: an efficient general purpose program for assigning sequence reads to genomic features. *Bioinformatics* **30**, 923-930 (2014).
111. G. H. Laurens van der Maaten, Visualizing Data Using t-SNE. *Journal of Machine Learning Research* **9**, 2579-2605 (2008).
112. H. Wickham, ggplot2. *Wiley Interdisciplinary Reviews: Computational Statistics* **3.2**, 180-185 (2011).
113. I. T. Jolliffe, "Principal Component Analysis for Special Types of Data" in Principal Component Analysis, I. T. Jolliffe, Ed. (Springer New York, New York, NY, 2002), 10.1007/0-387-22440-8_13, pp. 338-372.
114. M. I. Love, W. Huber, S. Anders, Moderated estimation of fold change and dispersion for RNA-seq data with DESeq2. *Genome Biol* **15**, 550 (2014).
115. G. Yu, L. G. Wang, Y. Han, Q. Y. He, clusterProfiler: an R package for comparing biological themes among gene clusters. *Omics* **16**, 284-287 (2012).
116. M. A. Harris *et al.*, The Gene Ontology (GO) database and informatics resource. *Nucleic Acids Res* **32**, D258-261 (2004).
117. C. D. Klaassen, *Casarett and Doull's toxicology: the basic science of poisons* (McGraw-Hill New York, 2013), vol. 1236.
118. R. Grant, J. Hallett, S. Forbes, D. Hay, A. Callanan, Blended electrospinning with human liver extracellular matrix for engineering new hepatic microenvironments. *Scientific Reports* **9**, 6293 (2019).
119. M. T. Donato, N. Jiménez, J. V. Castell, M. J. Gómez-Lechón, Fluorescence-based assays for screening nine cytochrome P450 (P450) activities in intact cells expressing individual human P450 enzymes. *Drug Metabolism and Disposition* **32**, 699-706 (2004).
120. C. J. Detzel, Y. Kim, P. Rajagopalan, Engineered three-dimensional liver mimics recapitulate critical rat-specific bile acid pathways. *Tissue Eng Part A* **17**, 677-689 (2011).
121. O. Barbier, J. Trottier, J. Kaeding, P. Caron, M. Verreault, Lipid-activated transcription factors control bile acid glucuronidation. *Mol Cell Biochem* **326**, 3-8 (2009).
122. D. Liu *et al.*, UGT1A1 dysfunction increases liver burden and aggravates hepatocyte damage caused by long-term bilirubin metabolism disorder. *Biochem Pharmacol* **190**, 114592 (2021).
123. R. A. Marinelli, G. L. Lehmann, L. R. Soria, M. J. Marchissio, Hepatocyte aquaporins in bile formation and cholestasis. *Front Biosci (Landmark Ed)* **16**, 2642-2652 (2011).
124. S. Jelen *et al.*, Aquaporin-9 and urea transporter-A gene deletions affect urea transmembrane passage in murine hepatocytes. *Am J Physiol Gastrointest Liver Physiol* **303**, G1279-1287 (2012).

125. J. Y. L. Chiang, Bile acid metabolism and signaling. *Compr Physiol* **3**, 1191-1212 (2013).
126. S. Manley, W. Ding, Role of farnesoid X receptor and bile acids in alcoholic liver disease. *Acta Pharm Sin B* **5**, 158-167 (2015).
127. T. Kroll, M. Prescher, S. H. J. Smits, L. Schmitt, Structure and Function of Hepatobiliary ATP Binding Cassette Transporters. *Chemical Reviews* **121**, 5240-5288 (2021).
128. M. Akram, Citric Acid Cycle and Role of its Intermediates in Metabolism. *Cell Biochemistry and Biophysics* **68**, 475-478 (2014).
129. L. Rui, Energy metabolism in the liver. *Compr Physiol* **4**, 177-197 (2014).
130. R. Stark *et al.*, Phosphoenolpyruvate cycling via mitochondrial phosphoenolpyruvate carboxykinase links anaplerosis and mitochondrial GTP with insulin secretion. *J Biol Chem* **284**, 26578-26590 (2009).
131. Z. Wang, C. Dong, Gluconeogenesis in Cancer: Function and Regulation of PEPCK, FBPase, and G6Pase. *Trends in Cancer* **5**, 30-45 (2019).
132. E. D. Montal *et al.*, Inhibition of phosphoenolpyruvate carboxykinase blocks lactate utilization and impairs tumor growth in colorectal cancer. *Cancer & Metabolism* **7**, 8 (2019).
133. J. Xiang, K. Wang, N. Tang, PCK1 dysregulation in cancer: Metabolic reprogramming, oncogenic activation, and therapeutic opportunities. *Genes Dis* **10**, 101-112 (2023).
134. S. Yu, S. Meng, M. Xiang, H. Ma, Phosphoenolpyruvate carboxykinase in cell metabolism: Roles and mechanisms beyond gluconeogenesis. *Mol Metab* **53**, 101257 (2021).
135. S. V. Madhunapantula, P. J. Mosca, G. P. Robertson, The Akt signaling pathway: an emerging therapeutic target in malignant melanoma. *Cancer Biol Ther* **12**, 1032-1049 (2011).
136. G. E. Shambaugh, 3rd, Urea biosynthesis I. The urea cycle and relationships to the citric acid cycle. *Am J Clin Nutr* **30**, 2083-2087 (1977).
137. T. M. Leung, N. Nieto, CYP2E1 and oxidant stress in alcoholic and non-alcoholic fatty liver disease. *J Hepatol* **58**, 395-398 (2013).
138. U. M. Zanger, M. Schwab, Cytochrome P450 enzymes in drug metabolism: Regulation of gene expression, enzyme activities, and impact of genetic variation. *Pharmacology & Therapeutics* **138**, 103-141 (2013).
139. Y. Maruo, M. Iwai, A. Mori, H. Sato, Y. Takeuchi, Polymorphism of UDP-glucuronosyltransferase and drug metabolism. *Curr Drug Metab* **6**, 91-99 (2005).
140. A. Rowland, J. O. Miners, P. I. Mackenzie, The UDP-glucuronosyltransferases: Their role in drug metabolism and detoxification. *The International Journal of Biochemistry & Cell Biology* **45**, 1121-1132 (2013).
141. K. Klein, S. Winter, M. Turpeinen, M. Schwab, U. M. Zanger, Pathway-Targeted Pharmacogenomics of CYP1A2 in Human Liver. *Front Pharmacol* **1**, 129-129 (2010).
142. S. David, J. P. Hamilton, Drug-induced Liver Injury. *US Gastroenterol Hepatol Rev* **6**, 73-80 (2010).
143. L. Kuna *et al.*, Models of Drug Induced Liver Injury (DILI) - Current Issues and Future Perspectives. *Curr Drug Metab* **19**, 830-838 (2018).
144. Y. Lu, A. I. Cederbaum, CYP2E1 and oxidative liver injury by alcohol. *Free Radic Biol Med* **44**, 723-738 (2008).
145. C. Guo, L. Sun, X. Chen, D. Zhang, Oxidative stress, mitochondrial damage and neurodegenerative diseases. *Neural Regen Res* **8**, 2003-2014 (2013).
146. E. P. Neve, M. Ingelman-Sundberg, Molecular basis for the transport of cytochrome P450 2E1 to the plasma membrane. *J Biol Chem* **275**, 17130-17135 (2000).
147. R. F. Novak, K. J. Woodcroft, The alcohol-inducible form of cytochrome P450 (CYP 2E1): role in toxicology and regulation of expression. *Arch Pharm Res* **23**, 267-282 (2000).

148. T. A. Kocarek, R. C. Zangar, R. F. Novak, Post-transcriptional Regulation of Rat CYP2E1 Expression: Role of CYP2E1 mRNA Untranslated Regions in Control of Translational Efficiency and Message Stability. *Archives of Biochemistry and Biophysics* **376**, 180-190 (2000).
149. F. Sivandzade, A. Bhalerao, L. Cucullo, Analysis of the Mitochondrial Membrane Potential Using the Cationic JC-1 Dye as a Sensitive Fluorescent Probe. *Bio Protoc* **9** (2019).
150. E. P. Allain, M. Rouleau, E. Lévesque, C. Guillemette, Emerging roles for UDP-glucuronosyltransferases in drug resistance and cancer progression. *British Journal of Cancer* **122**, 1277-1287 (2020).
151. E. S. Tzanakakis, L. K. Hansen, W. S. Hu, The role of actin filaments and microtubules in hepatocyte spheroid self-assembly. *Cell Motil Cytoskeleton* **48**, 175-189 (2001).
152. N. Roy-Chowdhury, X. Wang, C. Guha, J. Roy-Chowdhury, Hepatocyte-like cells derived from induced pluripotent stem cells. *Hepatol Int* **11**, 54-69 (2017).
153. M. J. Perugorria *et al.*, Wnt–β-catenin signalling in liver development, health and disease. *Nature Reviews Gastroenterology & Hepatology* **16**, 121-136 (2019).
154. P. L. Jansen, Fibroblast growth factor 19, a double-edged sword. *Hepat Oncol* **4**, 1-4 (2017).
155. C. Lindley *et al.*, The effect of cyclophosphamide with and without dexamethasone on cytochrome P450 3A4 and 2B6 in human hepatocytes. *Drug Metab Dispos* **30**, 814-822 (2002).
156. W. Zhang *et al.*, Efficient generation of functional hepatocyte-like cells from human fetal hepatic progenitor cells in vitro. *J Cell Physiol* **227**, 2051-2058 (2012).
157. V. L. Dao Thi *et al.*, Stem cell-derived polarized hepatocytes. *Nature Communications* **11**, 1677 (2020).
158. A. W. Overeem *et al.*, Pluripotent stem cell-derived bile canaliculi-forming hepatocytes to study genetic liver diseases involving hepatocyte polarity. *J Hepatol* **71**, 344-356 (2019).
159. U. Anand, C. V. Anand, Connecting links between the urea cycle and the TCA cycle: a tutorial exercise. *Biochemical Education* **27**, 153-154 (1999).
160. S. de Cima *et al.*, Structure of human carbamoyl phosphate synthetase: deciphering the on/off switch of human ureagenesis. *Scientific Reports* **5**, 16950 (2015).
161. S. F. Zhou, C. C. Xue, X. Q. Yu, C. Li, G. Wang, Clinically important drug interactions potentially involving mechanism-based inhibition of cytochrome P450 3A4 and the role of therapeutic drug monitoring. *Ther Drug Monit* **29**, 687-710 (2007).
162. L.-G. Liu *et al.*, CYP2E1-dependent hepatotoxicity and oxidative damage after ethanol administration in human primary hepatocytes. *World J Gastroenterol* **11**, 4530-4535 (2005).
163. S. C. Preissner *et al.*, Polymorphic cytochrome P450 enzymes (CYPs) and their role in personalized therapy. *PLoS One* **8**, e82562 (2013).
164. Y. Choudhury *et al.*, Patient-specific hepatocyte-like cells derived from induced pluripotent stem cells model pazopanib-mediated hepatotoxicity. *Scientific Reports* **7**, 41238 (2017).
165. Y. Guttman, A. Nudel, Z. Kerem, Polymorphism in Cytochrome P450 3A4 Is Ethnicity Related. *Front Genet* **10**, 224 (2019).
166. A. Brazovskaja, B. Treutlein, J. G. Camp, High-throughput single-cell transcriptomics on organoids. *Curr Opin Biotechnol* **55**, 167-171 (2019).
167. T. Chen, S. Oh, S. Gregory, X. Shen, A. M. Diehl, Single-cell omics analysis reveals functional diversification of hepatocytes during liver regeneration. *JCI Insight* **5** (2020).
168. P. Nell *et al.*, Identification of an FXR-modulated liver-intestine hybrid state in iPSC-derived hepatocyte-like cells. *J Hepatol* **77**, 1386-1398 (2022).

169. B. T. Wesley *et al.*, Single-cell atlas of human liver development reveals pathways directing hepatic cell fates. *Nat Cell Biol* **24**, 1487-1498 (2022).
170. J. G. Camp *et al.*, Multilineage communication regulates human liver bud development from pluripotency. *Nature* **546**, 533-538 (2017).
171. J. C. Dunn, M. L. Yarmush, H. G. Koebe, R. G. Tompkins, Hepatocyte function and extracellular matrix geometry: long-term culture in a sandwich configuration. *The FASEB Journal* **3**, 174-177 (1989).
172. A. N. Tegge *et al.*, Transcriptomic Analysis of Hepatic Cells in Multicellular Organotypic Liver Models. *Scientific Reports* **8**, 11306 (2018).
173. G. Wang *et al.*, Co-culture system of hepatocytes and endothelial cells: two in vitro approaches for enhancing liver-specific functions of hepatocytes. *Cytotechnology* **70**, 1279-1290 (2018).
174. X. Zhu, B. Zhang, Y. He, J. Bao, Liver Organoids: Formation Strategies and Biomedical Applications. *Tissue Eng Regen Med* **18**, 573-585 (2021).
175. W. Song *et al.*, Engraftment of human induced pluripotent stem cell-derived hepatocytes in immunocompetent mice via 3D co-aggregation and encapsulation. *Sci Rep* **5**, 16884 (2015).
176. G. Shiota, J. Okano, H. Kawasaki, T. Kawamoto, T. Nakamura, Serum hepatocyte growth factor levels in liver diseases: clinical implications. *Hepatology* **21**, 106-112 (1995).
177. K. Si-Tayeb, F. P. Lemaigre, S. A. Duncan, Organogenesis and Development of the Liver. *Developmental Cell* **18**, 175-189 (2010).
178. C. Chen, A. Soto-Gutierrez, P. M. Baptista, B. Spee, Biotechnology Challenges to In Vitro Maturation of Hepatic Stem Cells. *Gastroenterology* **154**, 1258-1272 (2018).
179. A. DeLaForest *et al.*, HNF4A is essential for specification of hepatic progenitors from human pluripotent stem cells. *Development* **138**, 4143-4153 (2011).
180. X. Sun, P. D. Kaufman, Ki-67: more than a proliferation marker. *Chromosoma* **127**, 175-186 (2018).
181. T. Nakamura, S. Mizuno, The discovery of hepatocyte growth factor (HGF) and its significance for cell biology, life sciences and clinical medicine. *Proc Jpn Acad Ser B Phys Biol Sci* **86**, 588-610 (2010).
182. S. Dooley, P. ten Dijke, TGF-β in progression of liver disease. *Cell Tissue Res* **347**, 245-256 (2012).
183. R. J. Fontana, Acute liver failure including acetaminophen overdose. *Med Clin North Am* **92**, 761-794, viii (2008).
184. J. B. Hoek, J. G. Pastorino, Ethanol, oxidative stress, and cytokine-induced liver cell injury. *Alcohol* **27**, 63-68 (2002).
185. N. Kaplowitz, L. D. DeLeve, *Drug-induced liver disease* (CRC Press, 2007).
186. N. Kamiguchi, E. Aoyama, T. Okuda, T. Moriwaki, A 96-well plate assay for CYP4503A induction using cryopreserved human hepatocytes. *Drug Metab Dispos* **38**, 1912-1916 (2010).
187. A. Miyajima *et al.*, Role of Oncostatin M in hematopoiesis and liver development. *Cytokine Growth Factor Rev* **11**, 177-183 (2000).
188. W. Goessling *et al.*, Genetic interaction of PGE2 and Wnt signaling regulates developmental specification of stem cells and regeneration. *Cell* **136**, 1136-1147 (2009).
189. C. G. Huh *et al.*, Hepatocyte growth factor/c-met signaling pathway is required for efficient liver regeneration and repair. *Proc Natl Acad Sci U S A* **101**, 4477-4482 (2004).
190. W. H. Choe, S. K. Baik, Prostaglandin E2 -mediated immunosuppression and the role of albumin as its modulator. *Hepatology* **61**, 1080-1082 (2015).

191. N. Li *et al.*, LXR modulation blocks prostaglandin E2 production and matrix degradation in cartilage and alleviates pain in a rat osteoarthritis model. *Proc Natl Acad Sci U S A* **107**, 3734-3739 (2010).
192. A. Honda *et al.*, Cholesterol 25-hydroxylation activity of CYP3A. *Journal of Lipid Research* **52**, 1509-1516 (2011).
193. J. M. Lehmann *et al.*, Activation of the Nuclear Receptor LXR by Oxysterols Defines a New Hormone Response Pathway*. *Journal of Biological Chemistry* **272**, 3137-3140 (1997).
194. Y. Cao *et al.*, Serum oncostatin M is a potential biomarker of disease activity and infliximab response in inflammatory bowel disease measured by chemiluminescence immunoassay. *Clinical Biochemistry* **100**, 35-41 (2022).
195. X.-P. Huang *et al.*, Elevated serum prostaglandin E2 predicts the risk of infection in hepatitis B virus-related acute-on-chronic liver failure patients. *Asian Pacific Journal of Tropical Medicine* **10**, 916-920 (2017).
196. D. Naka *et al.*, Internalization and degradation of hepatocyte growth factor in hepatocytes with down-regulation of the receptor/c-Met. *FEBS Lett* **329**, 147-152 (1993).
197. M. Coetzee, M. Haag, N. Claassen, M. C. Kruger, Stimulation of prostaglandin E2 (PGE2) production by arachidonic acid, oestrogen and parathyroid hormone in MG-63 and MC3T3-E1 osteoblast-like cells. *Prostaglandins Leukot Essent Fatty Acids* **73**, 423-430 (2005).
198. A. E. Moore *et al.*, HGF/Met signalling promotes PGE(2) biogenesis via regulation of COX-2 and 15-PGDH expression in colorectal cancer cells. *Carcinogenesis* **30**, 1796-1804 (2009).
199. J. Henkel *et al.*, Oncostatin M produced in Kupffer cells in response to PGE2: possible contributor to hepatic insulin resistance and steatosis. *Lab Invest* **91**, 1107-1117 (2011).
200. P. Repovic, E. N. Benveniste, Prostaglandin E2 is a novel inducer of oncostatin-M expression in macrophages and microglia. *J Neurosci* **22**, 5334-5343 (2002).
201. P. Loyer *et al.*, Interleukin 4 inhibits the production of some acute-phase proteins by human hepatocytes in primary culture. *FEBS Lett* **336**, 215-220 (1993).
202. D. Nedelcu, J. Liu, Y. Xu, C. Jao, A. Salic, Oxysterol binding to the extracellular domain of Smoothened in Hedgehog signaling. *Nat Chem Biol* **9**, 557-564 (2013).
203. B.-C. Lee *et al.*, PGE2 maintains self-renewal of human adult stem cells via EP2-mediated autocrine signaling and its production is regulated by cell-to-cell contact. *Scientific Reports* **6**, 26298 (2016).
204. A. Singh, R. Raju, M. Mrad, P. Reddell, G. Münch, The reciprocal EC(50) value as a convenient measure of the potency of a compound in bioactivity-guided purification of natural products. *Fitoterapia* **143**, 104598 (2020).
205. J. L. McGill, R. E. Sacco, The Immunology of Bovine Respiratory Disease: Recent Advancements. *Vet Clin North Am Food Anim Pract* **36**, 333-348 (2020).
206. T. L. Ollivett, How Does Housing Influence Bovine Respiratory Disease in Dairy and Veal Calves? *Vet Clin North Am Food Anim Pract* **36**, 385-398 (2020).
207. D. Griffin, M. M. Chengappa, J. Kuszak, D. S. McVey, Bacterial Pathogens of the Bovine Respiratory Disease Complex. *Veterinary Clinics of North America: Food Animal Practice* **26**, 381-394 (2010).
208. G. M. Murray *et al.*, Evolving views on bovine respiratory disease: An appraisal of selected key pathogens – Part 1. *The Veterinary Journal* **217**, 95-102 (2016).
209. T. A. Edwards, Control Methods for Bovine Respiratory Disease for Feedlot Cattle. *Veterinary Clinics of North America: Food Animal Practice* **26**, 273-284 (2010).
210. G. D. Snowder, L. D. Van Vleck, L. V. Cundiff, G. L. Bennett, Bovine respiratory disease in feedlot cattle: environmental, genetic, and economic factors. *J Anim Sci* **84**, 1999-2008 (2006).

211. S. Crosby, B. Credille, S. Giguère, R. Berghaus, Comparative efficacy of enrofloxacin to that of tulathromycin for the control of bovine respiratory disease and prevalence of antimicrobial resistance in Mannheimia haemolytica in calves at high risk of developing bovine respiratory disease1. *Journal of Animal Science* **96**, 1259-1267 (2018).
212. K. Singh, J. W. Ritchey, A. W. Confer, Mannheimia haemolytica: bacterial-host interactions in bovine pneumonia. *Vet Pathol* **48**, 338-348 (2011).
213. S. Amat, D. Baines, E. Timsit, J. Hallewell, T. W. Alexander, Essential oils inhibit the bovine respiratory pathogens Mannheimia haemolytica, Pasteurella multocida and Histophilus somni and have limited effects on commensal bacteria and turbinate cells in vitro. *J Appl Microbiol* **126**, 1668-1682 (2019).
214. D. Cozens *et al.*, Pathogenic Mannheimia haemolytica Invades Differentiated Bovine Airway Epithelial Cells. *Infect Immun* **87**, e00078-00019 (2019).
215. A. Khodakaram-Tafti, G. H. Farjanikish, Persistent bovine viral diarrhea virus (BVDV) infection in cattle herds. *Iran J Vet Res* **18**, 154-163 (2017).
216. J. D. Taylor, R. W. Fulton, T. W. Lehenbauer, D. L. Step, A. W. Confer, The epidemiology of bovine respiratory disease: what is the evidence for preventive measures? *Can Vet J* **51**, 1351-1359 (2010).
217. A. Pratelli *et al.*, Bovine respiratory disease in beef calves supported long transport stress: An epidemiological study and strategies for control and prevention. *Research in Veterinary Science* **135**, 450-455 (2021).
218. C. L. Klima *et al.*, Pathogens of bovine respiratory disease in North American feedlots conferring multidrug resistance via integrative conjugative elements. *J Clin Microbiol* **52**, 438-448 (2014).
219. A. Cameron, T. A. McAllister, Antimicrobial usage and resistance in beef production. *J Anim Sci Biotechnol* **7**, 68-68 (2016).
220. S. Andrés-Lasheras *et al.*, Prevalence and Risk Factors Associated With Antimicrobial Resistance in Bacteria Related to Bovine Respiratory Disease-A Broad Cross-Sectional Study of Beef Cattle at Entry Into Canadian Feedlots. *Front Vet Sci* **8**, 692646-692646 (2021).
221. K. Rajamanickam, J. Yang, M. K. Sakharkar, Phytochemicals as alternatives to antibiotics against major pathogens involved in bovine respiratory disease(BRD)and bovine mastitis(BM). *Bioinformation* **15**, 32-35 (2019).
222. J. M. Andrews, Determination of minimum inhibitory concentrations. *J Antimicrob Chemother* **48 Suppl 1**, 5-16 (2001).
223. L. J. Gershwin, L. J. Berghaus, K. Arnold, M. L. Anderson, L. B. Corbeil, Immune mechanisms of pathogenetic synergy in concurrent bovine pulmonary infection with Haemophilus somnus and bovine respiratory syncytial virus. *Veterinary Immunology and Immunopathology* **107**, 119-130 (2005).
224. C. Lin *et al.*, Histophilus somni Stimulates Expression of Antiviral Proteins and Inhibits BRSV Replication in Bovine Respiratory Epithelial Cells. *PLoS One* **11**, e0148551-e0148551 (2016).
225. D. Cozens *et al.*, Development and optimization of a differentiated airway epithelial cell model of the bovine respiratory tract. *Sci Rep* **8**, 853 (2018).
226. J. A. Zepp, E. E. Morrisey, Cellular crosstalk in the development and regeneration of the respiratory system. *Nat Rev Mol Cell Biol* **20**, 551-566 (2019).
227. P. W. Hellings, B. Steelant, Epithelial barriers in allergy and asthma. *J Allergy Clin Immunol* **145**, 1499-1509 (2020).
228. A. Ciechanowicz, Stem Cells in Lungs. *Adv Exp Med Biol* **1201**, 261-274 (2019).
229. A. F. Miguel, Penetration of inhaled aerosols in the bronchial tree. *Med Eng Phys* **44**, 25-31 (2017).

230. M. Zeineldin, J. Lowe, B. Aldridge, Contribution of the Mucosal Microbiota to Bovine Respiratory Health. *Trends in Microbiology* **27**, 753-770 (2019).
231. Y. Gon, S. Hashimoto, Role of airway epithelial barrier dysfunction in pathogenesis of asthma. *Allergology International* **67**, 12-17 (2018).
232. A. Buckley, J. R. Turner, Cell Biology of Tight Junction Barrier Regulation and Mucosal Disease. *Cold Spring Harb Perspect Biol* **10** (2018).
233. T. Otani, M. Furuse, Tight Junction Structure and Function Revisited. *Trends Cell Biol* **30**, 805-817 (2020).
234. C. Zihni, C. Mills, K. Matter, M. S. Balda, Tight junctions: from simple barriers to multifunctional molecular gates. *Nature Reviews Molecular Cell Biology* **17**, 564-580 (2016).
235. K. Okuda *et al.*, Localization of Secretory Mucins MUC5AC and MUC5B in Normal/Healthy Human Airways. *Am J Respir Crit Care Med* **199**, 715-727 (2019).
236. A.-C. Lagrée *et al.*, Bovine Organospecific Microvascular Endothelial Cell Lines as New and Relevant In Vitro Models to Study Viral Infections. *Int J Mol Sci* **21**, 5249 (2020).
237. H. P. V. a. R. L. Farrell, "The Anatomy and Physiology of the Bovine Respiratory System Relating to Pulmonary Disease" in The Cornell Veterinarian. (Arnold Printing Corporation, Ithaca, N.Y., 1978), vol. 68, pp. 555-581.
238. F. D. Bastida-Corcuera, K. H. Nielsen, L. B. Corbeil, Binding of bovine IgG2a and IgG2b allotypes to protein A, protein G, and Haemophilus somnus IgBPs. *Veterinary Immunology and Immunopathology* **71**, 143-149 (1999).
239. E. V. Sidorin, T. F. Solov'eva, IgG-binding proteins of bacteria. *Biochemistry (Mosc)* **76**, 295-308 (2011).
240. M. B. Gorbet, M. V. Sefton, "Review: Biomaterial-associated thrombosis: roles of coagulation factors, complement, platelets and leukocytes" in The Biomaterials: Silver Jubilee Compendium, D. F. Williams, Ed. (Elsevier Science, Oxford, 2004), https://doi.org/10.1016/B978-008045154-1.50025-3, pp. 219-241.
241. T. Kawasaki, T. Kawai, Toll-Like Receptor Signaling Pathways. *Frontiers in Immunology* **5** (2014).
242. C. R. H. Raetz, C. Whitfield, Lipopolysaccharide endotoxins. *Annu Rev Biochem* **71**, 635-700 (2002).
243. S. Amat, E. Timsit, D. Baines, J. Yanke, T. W. Alexander, Development of Bacterial Therapeutics against the Bovine Respiratory Pathogen Mannheimia haemolytica. *Appl Environ Microbiol* **85** (2019).
244. F. Leite, C. Kuckleburg, D. Atapattu, R. Schultz, C. J. Czuprynski, BHV-1 infection and inflammatory cytokines amplify the interaction of Mannheimia haemolytica leukotoxin with bovine peripheral blood mononuclear cells in vitro. *Veterinary Immunology and Immunopathology* **99**, 193-202 (2004).
245. D. B. Corry, F. Kheradmand, Induction and regulation of the IgE response. *Nature* **402**, 18-23 (1999).
246. N. Sachs *et al.*, Long-term expanding human airway organoids for disease modeling. *Embo j* **38** (2019).
247. A. J. Miller *et al.*, Generation of lung organoids from human pluripotent stem cells in vitro. *Nat Protoc* **14**, 518-540 (2019).
248. L. L. Bassel, J. L. Caswell, Bovine neutrophils in health and disease. *Cell Tissue Res* **371**, 617-637 (2018).
249. U. Koehler, O. Hildebrandt, N. Koehler, K. Sohrabi, [Are Small Airways the Key to Understanding Pathophysiology and Treatment Efficacy in Chronic Obstructive Pulmonary Diseases?]. *Pneumologie* **72**, 790-796 (2018).
250. N. Porchet *et al.*, Human mucin genes: genomic organization and expression of MUC4, MUC5AC and MUC5B. *Biochem Soc Trans* **23**, 800-805 (1995).

251. E. P. Lillehoj, K. Kato, W. Lu, K. C. Kim, Cellular and molecular biology of airway mucins. *Int Rev Cell Mol Biol* **303**, 139-202 (2013).
252. J. A. Whitsett, Airway Epithelial Differentiation and Mucociliary Clearance. *Ann Am Thorac Soc* **15**, S143-S148 (2018).
253. M. G. Roy *et al.*, Muc5b is required for airway defence. *Nature* **505**, 412-416 (2014).
254. A. Livraghi-Butrico *et al.*, Contribution of mucus concentration and secreted mucins Muc5ac and Muc5b to the pathogenesis of muco-obstructive lung disease. *Mucosal Immunol* **10**, 395-407 (2017).
255. I. Boukahil, C. J. Czuprynski, Mannheimia haemolytica biofilm formation on bovine respiratory epithelial cells. *Veterinary Microbiology* **197**, 129-136 (2016).
256. X. M. Bustamante-Marin, L. E. Ostrowski, Cilia and Mucociliary Clearance. *Cold Spring Harbor perspectives in biology* **9**, a028241 (2017).
257. D. Cozens *et al.*, Temporal differentiation of bovine airway epithelial cells grown at an air-liquid interface. *Scientific Reports* **8**, 14893 (2018).
258. T. M. Krunkosky, J. L. Jordan, E. Chambers, D. C. Krause, Mycoplasma pneumoniae host-pathogen studies in an air-liquid culture of differentiated human airway epithelial cells. *Microb Pathog* **42**, 98-103 (2007).
259. J. Kirchhoff, S. Uhlenbruck, K. Goris, G. M. Keil, G. Herrler, Three viruses of the bovine respiratory disease complex apply different strategies to initiate infection. *Vet Res* **45**, 20-20 (2014).
260. T. Kojima *et al.*, Regulation of tight junctions in upper airway epithelium. *BioMed research international* **2013**, 947072-947072 (2013).
261. O. H. Wittekindt, Tight junctions in pulmonary epithelia during lung inflammation. *Pflugers Arch* **469**, 135-147 (2017).
262. J. Lei *et al.*, The antimicrobial peptides and their potential clinical applications. *Am J Transl Res* **11**, 3919-3931 (2019).
263. G. Diamond *et al.*, Tracheal antimicrobial peptide, a cysteine-rich peptide from mammalian tracheal mucosa: peptide isolation and cloning of a cDNA. *Proceedings of the National Academy of Sciences of the United States of America* **88**, 3952-3956 (1991).
264. S. Yarus, J. M. Rosen, A. M. Cole, G. Diamond, Production of active bovine tracheal antimicrobial peptide in milk of transgenic mice. *Proceedings of the National Academy of Sciences of the United States of America* **93**, 14118-14121 (1996).
265. K. Taha-Abdelaziz *et al.*, Bactericidal activity of tracheal antimicrobial peptide against respiratory pathogens of cattle. *Veterinary Immunology and Immunopathology* **152**, 289-294 (2013).
266. K. Taha-Abdelaziz *et al.*, Regulation of tracheal antimicrobial peptide gene expression in airway epithelial cells of cattle. *Vet Res* **47**, 44 (2016).
267. G. B. Mitchell, M. H. Al-Haddawi, M. E. Clark, J. D. Beveridge, J. L. Caswell, Effect of corticosteroids and neuropeptides on the expression of defensins in bovine tracheal epithelial cells. *Infect Immun* **75**, 1325-1334 (2007).
268. L. Berghuis *et al.*, Comparison of innate immune agonists for induction of tracheal antimicrobial peptide gene expression in tracheal epithelial cells of cattle. *Vet Res* **45**, 105 (2014).
269. M. Al-Haddawi, G. B. Mitchell, M. E. Clark, R. D. Wood, J. L. Caswell, Impairment of innate immune responses of airway epithelium by infection with bovine viral diarrhea virus. *Vet Immunol Immunopathol* **116**, 153-162 (2007).
270. K. Vulikh *et al.*, Effect of tracheal antimicrobial peptide on the development of Mannheimia haemolytica pneumonia in cattle. *PLoS One* **14**, e0225533 (2019).
271. E. M. Kościuczuk *et al.*, Cathelicidins: family of antimicrobial peptides. A review. *Mol Biol Rep* **39**, 10957-10970 (2012).

272. A. Baumann, M. S. Kiener, B. Haigh, V. Perreten, A. Summerfield, Differential Ability of Bovine Antimicrobial Cathelicidins to Mediate Nucleic Acid Sensing by Epithelial Cells. *Frontiers in Immunology* **8** (2017).
273. I. Boukahil, C. J. Czuprynski, Mutual antagonism between Mannheimia haemolytica and Pasteurella multocida when forming a biofilm on bovine bronchial epithelial cells in vitro. *Veterinary Microbiology* **216**, 218-222 (2018).
274. I. Boukahil, C. J. Czuprynski, Characterization of Mannheimia haemolytica biofilm formation in vitro. *Veterinary Microbiology* **175**, 114-122 (2015).
275. P. D. Hodgson *et al.*, Effect of stress on viral–bacterial synergy in bovine respiratory disease: novel mechanisms to regulate inflammation. *Comparative and Functional Genomics* **6**, 244-250 (2005).
276. D. I. Kisiela, C. J. Czuprynski, Identification of Mannheimia haemolytica Adhesins Involved in Binding to Bovine Bronchial Epithelial Cells. *Infect Immun* **77**, 446-455 (2009).
277. D. McClenahan *et al.*, Effects of lipopolysaccharide and Mannheimia haemolytica leukotoxin on bovine lung microvascular endothelial cells and alveolar epithelial cells. *Clin Vaccine Immunol* **15**, 338-347 (2008).
278. A. U. N'jai, J. Rivera, D. N. Atapattu, K. Owusu-Ofori, C. J. Czuprynski, Gene expression profiling of bovine bronchial epithelial cells exposed in vitro to bovine herpesvirus 1 and Mannheimia haemolytica. *Veterinary Immunology and Immunopathology* **155**, 182-189 (2013).
279. M. E. Olson, H. Ceri, D. W. Morck, A. G. Buret, R. R. Read, Biofilm bacteria: formation and comparative susceptibility to antibiotics. *Can J Vet Res* **66**, 86-92 (2002).
280. J. J. Rivera-Rivas, D. Kisiela, C. J. Czuprynski, Bovine herpesvirus type 1 infection of bovine bronchial epithelial cells increases neutrophil adhesion and activation. *Veterinary Immunology and Immunopathology* **131**, 167-176 (2009).
281. D. C. Hodgins, P. E. Shewen, *Pneumonic pasteurellosis of cattle* (Oxofrd University Press, Cape Town (South Africa) ed. 2nd, 2004).
282. B. Petruzzi, A. Dickerman, K. Lahmers, W. K. Scarratt, T. J. Inzana, Polymicrobial Biofilm Interaction Between Histophilus somni and Pasteurella multocida. *Front Microbiol* **11**, 1561-1561 (2020).
283. I. Sandal, W. Hong, W. E. Swords, T. J. Inzana, Characterization and Comparison of Biofilm Development by Pathogenic and Commensal Isolates of Histophilus somni. *Journal of Bacteriology* **189**, 8179-8185 (2007).
284. M. J. Sylte, L. B. Corbeil, T. J. Inzana, C. J. Czuprynski, Haemophilus somnus induces apoptosis in bovine endothelial cells in vitro. *Infect Immun* **69**, 1650-1660 (2001).
285. R. D. Welsh, L. B. Dye, M. E. Payton, A. W. Confer, Isolation and antimicrobial susceptibilities of bacterial pathogens from bovine pneumonia: 1994--2002. *J Vet Diagn Invest* **16**, 426-431 (2004).
286. K. W. Ruby, R. W. Griffith, L. J. Gershwin, M. L. Kaeberle, Haemophilus somnus-induced IgE in calves vaccinated with commercial monovalent H. somnus bacterins. *Vet Microbiol* **76**, 373-383 (2000).
287. M. E. Prado, T. M. Prado, M. Payton, A. W. Confer, Maternally and naturally acquired antibodies to Mannheimia haemolytica and Pasteurella multocida in beef calves. *Veterinary Immunology and Immunopathology* **111**, 301-307 (2006).
288. B. Ujvári, L. Makrai, T. Magyar, Characterisation of a multiresistant Pasteurella multocida strain isolated from cattle. *Acta Vet Hung* **66**, 12-19 (2018).
289. S. M. Dabo, A. W. Confer, R. A. Quijano-Blas, Molecular and immunological characterization of Pasteurella multocida serotype A:3 OmpA: evidence of its role in P. multocida interaction with extracellular matrix molecules. *Microbial Pathogenesis* **35**, 147-157 (2003).

290. M. Apley, Bovine Respiratory Disease: Pathogenesis, Clinical Signs, and Treatment in Lightweight Calves. *Veterinary Clinics of North America: Food Animal Practice* **22**, 399-411 (2006).
291. F. P. Maunsell, G. A. Donovan, Mycoplasma bovis Infections in Young Calves. *Veterinary Clinics of North America: Food Animal Practice* **25**, 139-177 (2009).
292. S. Bürki *et al.*, Invasion and persistence of Mycoplasma bovis in embryonic calf turbinate cells. *Vet Res* **46**, 53-53 (2015).
293. J. L. Caswell, M. Archambault, Mycoplasma bovis pneumonia in cattle. *Animal Health Research Reviews* **8**, 161-186 (2007).
294. C. Josi *et al.*, Bovine Epithelial in vitro Infection Models for Mycoplasma bovis. *Front Cell Infect Microbiol* **8**, 329 (2018).
295. M. Suwanruengsri *et al.*, Production of granulomas in Mycoplasma bovis infection associated with meningitis-meningoencephalitis, endocarditis, and pneumonia in cattle. *J Vet Diagn Invest* **34**, 68-76 (2022).
296. B. W. Brodersen, Bovine Respiratory Syncytial Virus. *Veterinary Clinics of North America: Food Animal Practice* **26**, 323-333 (2010).
297. G. Taylor, Animal models of respiratory syncytial virus infection. *Vaccine* **35**, 469-480 (2017).
298. B. Viuff *et al.*, Replication and clearance of respiratory syncytial virus: apoptosis is an important pathway of virus clearance after experimental infection with bovine respiratory syncytial virus. *Am J Pathol* **161**, 2195-2207 (2002).
299. A. R. Hofstetter, R. E. Sacco, Oxidative stress pathway gene transcription after bovine respiratory syncytial virus infection in vitro and ex vivo. *Vet Immunol Immunopathol* **219**, 109956 (2020).
300. M. K. S. Rajput *et al.*, Both cytopathic and non-cytopathic bovine viral diarrhea virus (BVDV) induced autophagy at a similar rate. *Vet Immunol Immunopathol* **193-194**, 1-9 (2017).
301. H. C. Samson, C. L. Topliff, R. O. Donis, C. L. Kelling, Comparison of viral replication and IFN response in alpaca and bovine cells following bovine viral diarrhea virus infection. *Virology* **413**, 111-117 (2011).
302. C. F. Oguejiofor, C. Thomas, Z. Cheng, D. C. Wathes, Mechanisms linking bovine viral diarrhea virus (BVDV) infection with infertility in cattle. *Animal Health Research Reviews* **20**, 72-85 (2019).
303. M. F. Darweesh *et al.*, Characterization of the cytopathic BVDV strains isolated from 13 mucosal disease cases arising in a cattle herd. *Virus Research* **195**, 141-147 (2015).
304. E. Peterhans, T. W. Jungi, M. Schweizer, BVDV and innate immunity. *Biologicals* **31**, 107-112 (2003).
305. G. Pastenkos, B. Lee, S. M. Pritchard, A. V. Nicola, Bovine Herpesvirus 1 Entry by a Low-pH Endosomal Pathway. *J Virol* **92** (2018).
306. X. Fu, D. Chen, Y. Ma, W. Yuan, L. Zhu, Bovine Herpesvirus 1 Productive Infection Led to Inactivation of Nrf2 Signaling through Diverse Approaches. *Oxid Med Cell Longev* **2019**, 4957878 (2019).
307. V. L. D. Queiroz-Castro *et al.*, Detection of bovine herpesvirus 1 in cumulus-oocyte complexes of cows. *Research in Veterinary Science* **120**, 54-56 (2018).
308. C. Jones, S. Chowdhury, A review of the biology of bovine herpesvirus type 1 (BHV-1), its role as a cofactor in the bovine respiratory disease complex and development of improved vaccines. *Anim Health Res Rev* **8**, 187-205 (2007).
309. J. Ellis *et al.*, Infection of calves with in-vivo passaged bovine parainfluenza-3 virus, alone or in combination with bovine respiratory syncytial virus and bovine coronavirus. *Can J Vet Res* **84**, 163-171 (2020).

310. R. C. Reisinger, K. L. Heddleston, C. A. Manthei, A myxovirus (SF-4) associated with shipping fever of cattle. *J Am Vet Med Assoc* **135**, 147-152 (1959).
311. A. B. Hoerlein, M. E. Mansfield, F. R. Abinanti, R. J. Huebner, Studies of shipping fever of cattle. I. Para-influenza 3 virus antibodies in feeder calves. *J Am Vet Med Assoc* **135**, 153-160 (1959).
312. É. Leal *et al.*, Isolation of a Divergent Strain of Bovine Parainfluenza Virus Type 3 (BPIV3) Infecting Cattle in China. *Viruses* **11**, 489 (2019).
313. J. A. Ellis, Bovine Parainfluenza-3 Virus. *Veterinary Clinics of North America: Food Animal Practice* **26**, 575-593 (2010).
314. I. Sandal *et al.*, Histophilus somni biofilm formation in cardiopulmonary tissue of the bovine host following respiratory challenge. *Microbes Infect* **11**, 254-263 (2009).
315. H. C. L., K. Cassandra, Q. Uzma, C.-H. J. A., H. A. N., Mucin inhibits Pseudomonas aeruginosa biofilm formation by significantly enhancing twitching motility. *Canadian Journal of Microbiology* **60**, 155-166 (2014).
316. S. F. Elswaifi, W. K. Scarratt, T. J. Inzana, The role of lipooligosaccharide phosphorylcholine in colonization and pathogenesis of Histophilus somni in cattle. *Vet Res* **43**, 49 (2012).
317. N. Shah, A. B. Bandara, I. Sandal, T. J. Inzana, Natural competence in Histophilus somni strain 2336. *Veterinary Microbiology* **173**, 371-378 (2014).
318. A. A. Alkheraif *et al.*, Type 2 BVDV Npro suppresses IFN-1 pathway signaling in bovine cells and augments BRSV replication. *Virology* **507**, 123-134 (2017).
319. B. Zekarias *et al.*, Histophilus somni IbpA DR2/Fic in virulence and immunoprotection at the natural host alveolar epithelial barrier. *Infect Immun* **78**, 1850-1858 (2010).
320. J. R. Sheldon, H. A. Laakso, D. E. Heinrichs, I. T. Kudva, N. A. Cornick, Iron Acquisition Strategies of Bacterial Pathogens. *Microbiology Spectrum* **4**, 4.2.05 (2016).
321. L. Dortet, E. Veiga-Chacon, P. Cossart, "Listeria Monocytogenes" in Encyclopedia of Microbiology (Third Edition)*,* M. Schaechter, Ed. (Academic Press, Oxford, 2009), https://doi.org/10.1016/B978-012373944-5.00217-0, pp. 182-198.
322. R. Osman, P. Gonzalez-Cano, R. Brownlie, P. J. Griebel, Induction of interferon and interferon-induced antiviral effector genes following a primary bovine herpesvirus-1 (BHV-1) respiratory infection. *J Gen Virol* **98**, 1831-1842 (2017).
323. S. Chen, J. Schoen, Air-liquid interface cell culture: From airway epithelium to the female reproductive tract. *Reprod Domest Anim* **54 Suppl 3**, 38-45 (2019).
324. D. Jiang, N. Schaefer, H. W. Chu, "Air–Liquid Interface Culture of Human and Mouse Airway Epithelial Cells" in Lung Innate Immunity and Inflammation: Methods and Protocols*,* S. Alper, W. J. Janssen, Eds. (Springer New York, New York, NY, 2018), 10.1007/978-1-4939-8570-8_8, pp. 91-109.
325. A. G. Proudfoot, D. F. McAuley, M. J. D. Griffiths, M. Hind, Human models of acute lung injury. *Dis Model Mech* **4**, 145-153 (2011).
326. Y. Hu *et al.*, Comparative anti-inflammatory effect of curcumin at air-liquid interface and submerged conditions using lipopolysaccharide stimulated human lung epithelial A549 cells. *Pulm Pharmacol Ther* **63**, 101939 (2020).
327. D. Jiang, N. Schaefer, H. W. Chu, Air-Liquid Interface Culture of Human and Mouse Airway Epithelial Cells. *Methods Mol Biol* **1809**, 91-109 (2018).
328. S. Upadhyay, L. Palmberg, Air-Liquid Interface: Relevant In Vitro Models for Investigating Air Pollutant-Induced Pulmonary Toxicity. *Toxicological Sciences* **164**, 21-30 (2018).
329. Y. Ma *et al.*, A species-specific activation of Toll-like receptor signaling in bovine and sheep bronchial epithelial cells triggered by Mycobacterial infections. *Mol Immunol* **71**, 23-33 (2016).

330. T. E. Gray, K. Guzman, C. W. Davis, L. H. Abdullah, P. Nettesheim, Mucociliary differentiation of serially passaged normal human tracheobronchial epithelial cells. *Am J Respir Cell Mol Biol* **14**, 104-112 (1996).
331. R. S. Herbst, Review of epidermal growth factor receptor biology. *International Journal of Radiation Oncology*Biology*Physics* **59**, S21-S26 (2004).
332. J. S. Koo *et al.*, Restoration of the mucous phenotype by retinoic acid in retinoid-deficient human bronchial cell cultures: changes in mucin gene expression. *Am J Respir Cell Mol Biol* **20**, 43-52 (1999).
333. R. Wu, Y. H. Zhao, M. M. Chang, Growth and differentiation of conducting airway epithelial cells in culture. *Eur Respir J* **10**, 2398-2403 (1997).
334. Z. Darula, F. Sarnyai, K. F. Medzihradszky, O-glycosylation sites identified from mucin core-1 type glycopeptides from human serum. *Glycoconj J* **33**, 435-445 (2016).
335. A. Su *et al.*, Infection of bovine well-differentiated airway epithelial cells by Pasteurella multocida: actions and counteractions in the bacteria–host interactions. *Vet Res* **51**, 140 (2020).
336. K. Goris *et al.*, Differential sensitivity of differentiated epithelial cells to respiratory viruses reveals different viral strategies of host infection. *Journal of virology* **83**, 1962-1968 (2009).
337. J. J. Rivera Rivas, C. J. Czuprynski, Procoagulant activity of bovine neutrophils incubated with conditioned media or extracellular vesicles from Histophilus somni stimulated bovine brain endothelial cells. *Vet Immunol Immunopathol* **211**, 49-57 (2019).
338. J. H. Widdicombe, L. A. Sachs, W. E. Finkbeiner, Effects of growth surface on differentiation of cultures of human tracheal epithelium. *In Vitro Cell Dev Biol Anim* **39**, 51-55 (2003).
339. S. G. Klein, T. Serchi, L. Hoffmann, B. Blömeke, A. C. Gutleb, An improved 3D tetraculture system mimicking the cellular organisation at the alveolar barrier to study the potential toxic effects of particles on the lung. *Part Fibre Toxicol* **10**, 31-31 (2013).
340. M. Ravi, V. Paramesh, S. R. Kaviya, E. Anuradha, F. D. Solomon, 3D cell culture systems: advantages and applications. *J Cell Physiol* **230**, 16-26 (2015).
341. C. Jensen, Y. Teng, Is It Time to Start Transitioning From 2D to 3D Cell Culture? *Frontiers in Molecular Biosciences* **7** (2020).
342. J. B. Grinspan, S. N. Mueller, E. M. Levine, Bovine endothelial cells transformed in vitro by benzo(a)pyrene. *J Cell Physiol* **114**, 328-338 (1983).
343. M. Lupicka, A. Zadroga, A. Szczepańska, A. J. Korzekwa, Effect of ovarian steroids on vascular endothelial growth factor a expression in bovine uterine endothelial cells during adenomyosis. *BMC Vet Res* **15**, 473 (2019).
344. A. Bellis *et al.*, Autocrine Bradykinin Release Promotes Ischemic Preconditioning-Induced Cytoprotection in Bovine Aortic Endothelial Cells. *Int J Mol Sci* **21** (2020).
345. M. A. Breider, Z. Yang, Tissue factor expression in bovine endothelial cells induced by Pasteurella haemolytica lipopolysaccharide and interleukin-1. *Vet Pathol* **31**, 55-60 (1994).
346. D. B. Paulsen, D. A. Mosier, K. D. Clinkenbeard, A. W. Confer, Direct effects of Pasteurella haemolytica lipopolysaccharide on bovine pulmonary endothelial cells in vitro. *Am J Vet Res* **50**, 1633-1637 (1989).
347. M. A. Breider, S. Kumar, R. E. Corstvet, Interaction of bovine neutrophils in Pasteurella haemolytica mediated damage to pulmonary endothelial cells. *Vet Immunol Immunopathol* **27**, 337-350 (1991).
348. D. Lee, M. Chambers, A co-culture model of the bovine alveolus. *F1000Res* **8**, 357-357 (2019).
349. J. van der Vaart, H. Clevers, Airway organoids as models of human disease. *J Intern Med* **289**, 604-613 (2021).

350. C. E. Barkauskas *et al.*, Lung organoids: current uses and future promise. *Development* **144**, 986-997 (2017).
351. B. Cunniff, J. E. Druso, J. L. van der Velden, Lung organoids: advances in generation and 3D-visualization. *Histochemistry and Cell Biology* **155**, 301-308 (2021).
352. R. Pei *et al.*, Host metabolism dysregulation and cell tropism identification in human airway and alveolar organoids upon SARS-CoV-2 infection. *Protein Cell* **12**, 717-733 (2021).
353. N. Iakobachvili *et al.*, Mycobacteria-host interactions in human bronchiolar airway organoids. *Mol Microbiol* **117**, 682-692 (2022).
354. O. A. Prince, T. M. Krunkosky, D. C. Krause, In vitro spatial and temporal analysis of Mycoplasma pneumoniae colonization of human airway epithelium. *Infect Immun* **82**, 579-586 (2014).
355. Q. Tan, K. M. Choi, D. Sicard, D. J. Tschumperlin, Human airway organoid engineering as a step toward lung regeneration and disease modeling. *Biomaterials* **113**, 118-132 (2017).
356. A. Costa, C. de Souza Carvalho-Wodarz, V. Seabra, B. Sarmento, C. M. Lehr, Triple co-culture of human alveolar epithelium, endothelium and macrophages for studying the interaction of nanocarriers with the air-blood barrier. *Acta Biomater* **91**, 235-247 (2019).
357. E. Puertollano *et al.*, Effects of concentrated supernatants recovered from Lactobacillus plantarum on Escherichia coli growth and on the viability of a human promyelocytic cell line. *J Appl Microbiol* **106**, 1194-1203 (2009).
358. L. R. Wills (2019) Investigating Induced Pluripotent Stem Cells for Tissue Engineering and Hepatotoxicity Applications. in *Biomedical Engineering and Applied Mechanics* (Virginia Polytechnic Institute and State University).
359. S. Citi, The mechanobiology of tight junctions. *Biophys Rev* **11**, 783-793 (2019).
360. A. Preston, R. E. Mandrell, B. W. Gibson, M. A. Apicella, The lipooligosaccharides of pathogenic gram-negative bacteria. *Crit Rev Microbiol* **22**, 139-180 (1996).
361. M. L. Chen, Z. Ge, J. G. Fox, D. B. Schauer, Disruption of tight junctions and induction of proinflammatory cytokine responses in colonic epithelial cells by Campylobacter jejuni. *Infect Immun* **74**, 6581-6589 (2006).
362. T. Tanaka, M. Narazaki, T. Kishimoto, IL-6 in inflammation, immunity, and disease. *Cold Spring Harb Perspect Biol* **6**, a016295 (2014).
363. E. J. Giamarellos-Bourboulis, M. Raftogiannis, The immune response to severe bacterial infections: consequences for therapy. *Expert Rev Anti Infect Ther* **10**, 369-380 (2012).
364. S. A. Dunbar, C. Gardner, S. Das, Diagnosis and Management of Bloodstream Infections With Rapid, Multiplexed Molecular Assays. *Front Cell Infect Microbiol* **12**, 859935 (2022).
365. P. Dowling, M. Clynes, Conditioned media from cell lines: a complementary model to clinical specimens for the discovery of disease-specific biomarkers. *Proteomics* **11**, 794-804 (2011).
366. T. Liu, L. Zhang, D. Joo, S.-C. Sun, NF-κB signaling in inflammation. *Signal Transduction and Targeted Therapy* **2**, 17023 (2017).
367. D. K. Morrison, MAP kinase pathways. *Cold Spring Harb Perspect Biol* **4** (2012).
368. L. Heumos *et al.*, Best practices for single-cell analysis across modalities. *Nature Reviews Genetics* **24**, 550-572 (2023).
369. Y. Hao *et al.*, Integrated analysis of multimodal single-cell data. *Cell* **184**, 3573-3587.e3529 (2021).
370. H. Clevers, COVID-19: organoids go viral. *Nat Rev Mol Cell Biol* **21**, 355-356 (2020).
371. B. Wang *et al.*, Two mutations in the ORF1 of genotype 1 hepatitis E virus enhance virus replication and may associate with fulminant hepatic failure. *Proc Natl Acad Sci U S A* **119**, e2207503119 (2022).